UNIVERSITY OF OKLAHOMA

GRADUATE COLLEGE

AN INTEGRATED GEOMECHANICS AND PETROPHYSICS STUDY OF HYDRAULIC FRACTURING IN NATURALLY FRACTURED RESERVOIRS

A DISSERTATION

SUBMITTED TO THE GRADUATE FACULTY

in partial fulfillment of the requirements for the

Degree of

DOCTOR OF PHILOSOPHY

By

XIAOCHUN JIN
Norman, Oklahoma
2014

Downloaded from SHAREOK. Persistent Handle URL: https://hdl.handle.net/11244/10343

AN INTEGRATED GEOMECHANICS AND PETROPHYSICS STUDY OF
HYDRAULIC FRACTURING IN NATURALLY FRACTURED RESERVOIRS

A DISSERTATION APPROVED FOR THE
MEWBOURNE SCHOOL OF PETROLEUM AND GEOLOGICAL ENGINEERING

BY

_____
Dr. Subhash N. Shah, Chair

_____
Dr. Jean-Claude Roegiers

_____
Dr. Ahmad Ghassemi

_____
Dr. Deepak Devegowda

_____
Dr. Prakash Vedula

© Copyright by XIAOCHUN JIN 2014
All Rights Reserved.

This Dissertation is dedicated to my beloved

Mom and Dad (Shungen Jin & Caie Xiong), Wife (Xiaoshuai Lu), Sons (Xuechong Jin & Xueyuan Jin)

Whose Love and Support contributed to this Achievement

Acknowledgements

I would like to express my deepest appreciation and gratitude to my advisor, Dr. Subhash Shah, for his constant encouragement, patient guidance, and constructive mentorship. I sincerely appreciate him for bringing me into the world of hydraulic fracturing and teaching me to be an independent person of integrity. His rigorous academic attitude has been positively influencing my career. He is always ready to help no matter how busy he is. I also deeply thank Dr. Jean-Claude Roegiers for bringing me into the world of rock fracture mechanics and sharing his insightful vision in petroleum geomechanics, which inspired me to explore new challenges of geomechanics independently. None of the works in this dissertation could have been accomplished without Dr. Shah's remarkable supervision and Dr. Roegiers' excellent guidance. I also would like to thank both Dr. Shah and Dr. Roegiers for introducing me to experts in the petroleum industry, and writing recommendation letters for the applications of internships, full time employment, and scholarships/fellowships. I would never forget the support from both Profs. Shah and Roegiers in the toughest time of my graduate study. I would like to acknowledge Prof. Bor-Jier (Ben) Shiau for talking to me whenever I stop by his office. He said: "During my down time, I try to remind myself. Am I better than yesterday or last year? Do I keep moving forward and no matter how successful or bad last year? I am competing with myself. This help me to focus on what I can, and learn some new things or ideas." I also greatly appreciate my committee members, Dr. Ahmad Ghassemi, Dr. Deepak Devegowda, and Dr. Prakash Vedula for their valuable discussions, advices, and comments that helped to improve the quality of this dissertation.

Special thanks go to Wadood El-Rabaa of Blade Energy Partners, Dr. Xu Li of Shell Oil Company, Dr. Jerry Truax of Linn Energy, Dr. Gang Li of Anadarko Petroleum, Dr. Zhengwen Zeng of BP, Prof. Roger Slatt, Mr. Yawei Li, Mr. Mao Sheng, Mr. Ting Wang, Mr. Yuqi Zhou, Mr. Kai Huang, and Mr. Bo Zhang for contributing to the valuable discussions; to my officemates Mr. Sarvesh Naik and Mr. Idowu Dosunmu for academic discussions, and humor & jokes; to Mr. Luchao Jin, Mrs. Jiman Liu, Mr. Kai Wang, Mr. Guomin Ji, Xin Fan for helping me with paper work when I was away from campus; to my best friends in Sarkeys Energy Center for all the wonderful moments we shared through all these years; to Dr. Bing Hou and Dr. Mian Chen of China University of Petroleum (Beijing) for sharing laboratory data of hydraulic fracturing experiments; to Shell International Exploration and Production Company in Houston and Blade Energy Partners in Frisco, Texas for offering summer internships, which broadened my vision of petroleum industry, and helped me learn about the differences between academic and industry.

Most importantly, I would like to thank my family (Father, Shungen Jin, Mother, Caie Xiong, Wife, Xiaoshuai Lu, Oldest son, Xuechong Jin, and Younger son, Xueyuan Jin), for their understanding, continuous support and love that sustained me throughout the years and finally to make this achievement a reality.

Table of Contents

Acknowledgements iv

List of Tables ……..xi

List of Figures ……xii

Abstract……..……...xvi

Chapter 1. Introduction 1

1.1 Overview of Geomechanics in Unconventional Shale 1

1.2 Overview of Petrophysics in Unconventional Shale 4

1.3 Problem Statement 6

1.4 Dissertation Overview 9

Chapter 2. Mixed-Mode Fracture Propagation in Hydraulic Fracturing: Theoretical Analysis and Experimental Verification 12

2.1 Introduction 12

2.2 Methodology 16

2.2.1 Stress Intensity Factors for a Preexisting Inclined Fracture 16

2.2.2 Determination of Breakdown Pressure for Mixed-Mode Fracture Propagation 18

2.2.3 Stress Field near Fracture Tip for Inclined Fracture in Polar Coordinate System 20

2.2.4 Fracture Propagation Criteria 20

2.3 Theoretical Solutions 21

2.3.1 The Relationship between Fracture Initiation Angle and Stress Intensity Factor Ratio 21

2.3.2 Comparison of Fracture Initiation Angles for Different Fracture Propagation Criteria 24
2.4 Factors Influencing Fracture Initiation Angle 25
2.4.1 Stress Anisotropy Influence on Fracture Initiation Angle 26
2.4.2 Breakdown Pressure/Fracture Toughness Influence on Fracture Initiation Angle 29
2.4.3 Poisson's Ratio Influence on Fracture Initiation Angle (S-criterion) 31
2.5 Experimental Verification 32
2.6 Discussion and Conclusions 42
Chapter 3. Weight Function and Stress Intensity factor for Symmetrical Radial Cracks Emanating from Borehole 45
3.1 Introduction 45
3.2 Determination of weight function parameters for symmetrical radial cracks 48
3.3 Validation 51
3.3.1 Validation for Fig. 3.2-A 51
3.3.2 Validation for Fig. 3.2-B 52
3.4 Application in Petroleum Engineering 53
3.4.1 Case I: Crack of non-constant fracturing pressure aligns with principal stress 55
3.4.2 Case II: Inclined Crack with constant fracturing pressure 57
3.4.3 Case III: Inclined Crack with non-constant fracturing pressure 57
3.5 Discussion and Conclusions 58

Chapter 4. Breakdown Pressure Determination - A Fracture Mechanics Approach 60

4.1 Introduction 60

4.2 Procedures of Breakdown Pressure Calculation by Weight Function Method 67

4.3 Sensitivity Study of Breakdown Pressure 69

4.3.1 Influence of Preexisting Crack Length on Breakdown Pressure 69

4.3.2 Influence of Crack Orientation on Breakdown Pressure 71

4.3.3 Influence of Stress Contrast on Breakdown Pressure 72

4.3.4 Influence of Fracture Toughness on Breakdown Pressure 74

4.3.5 Influence of Internal Fracture Pressure on Breakdown Pressure 75

4.4 Comparison of Breakdown Pressures by Traditional and Weight Function Methods 77

4.5 Experimental Verification 80

4.5.1 Verification with In-house Laboratory Experimental Data 80

4.5.2 Verification with Published Data by Rummel 82

4.6 Discussion and Conclusions 85

Chapter 5. Petrophysical Approach to Brittleness Prediction: Woodford, Barnett, and Eagle Ford Shale 88

5.1 Introduction 88

5.2 Benchmark Brittleness Definition 93

5.3 Prediction of Brittleness with Neutron Porosity for Typical Shale Reservoirs 96

5.3.1 Correlation of Brittleness with Porosity for Woodford Shale 96

5.3.2 Correlation of Brittleness with Porosity for Barnett Shale 98
5.3.3 Correlation of Brittleness with Porosity for Eagle Ford Shale 99
5.4 Prediction of Brittleness with Compressional Sonic Slowness for Typical Shale Reservoirs 100
5.4.1 Correlation of Brittleness with Compressional Sonic Slowness for Woodford Shale 100
5.4.2 Correlation of Brittleness with Compressional Sonic Slowness for Barnett Shale 101
5.4.3 Correlation of Brittleness with Porosity for Eagle ford Shale 102
5.5 Global Correlations of Brittleness with Porosity and Compressional Slowness 103
5.5.1 Global Correlation of Brittleness with Porosity 103
5.5.2 Global Correlation of Brittleness with Sonic Compressional Slowness 104
5.6 Field Application and Verification 106
5.7 Discussion and Conclusions 108
Chapter 6. Fracability Evaluation in Shale Reservoirs - An Integrated Petrophysics and Geomechanics Approach 110
6.1 Introduction 110
6.2 Fracture Toughness and Strain Energy Release Rate 111
6.2.1 Fracture Toughness 111
6.2.2 Strain Energy Release Rate 114
6.3 Fracture Barrier 115

6.4 Fracability Index Model 117
6.5 Field Application 122
6.6 Discussion and Conclusions 127
Chapter 7. Conclusions and Recommendations 129
7.1 Conclusions 129
7.2 Recommendations 130
Nomenclatures 133
References…… 139
Appendix……. 154
Appendix A: Solution of Maximum Tangential Stress Criterion 154
Appendix B: Solution of Maximum Energy Release Rate 154
Appendix C: Solution of Minimum Strain Energy Density Criterion 156
Appendix D: Algorithm of Modified Bisection Method 157
Appendix E: Mathematica code for solving parameters of weight function 158
Appendix F: Weight function parameters for symmetrical radial cracks emanating from borehole 159

List of Tables

Table 2.1 Basic parameters for the prediction of fracture initiation angle 22

Table 2.2 Properties of experimental samples 36

Table 2.3 Configurations of experimental samples 36

Table 2.4 Experimental conditions and breakdown pressures 39

Table 2.5 Theoretical and experimental fracture initiation angles 40

Table 3.1 Inputs for Figs. 3.6 and 3.7 55

Table 4.1 Values of $f\ (a/R_w)$ and $g\ (a/R_w)$ for two symmetrical radial cracks 65

Table 4.2 Basic parameters and their values for prediction of breakdown pressure 69

Table 4.3 Basic parameters for breakdown pressure comparison 77

Table 4.4 Experimental conditions and breakdown pressures in the laboratory 81

Table 4.5 Experimental conditions and breakdown pressures by Rummel 82

Table 5.1 Selected Expressions of Brittleness 92

Table 6.1 Error analysis of correlations for fracture toughness 112

Table F-1 Parameters of weight function for different ratio of crack length to circular radius 159

List of Figures

Figure 2.1 Top views of fracture propagation near horizontal (A) and vertical (B) wells. 13

Figure 2.2 Three basic fracture modes of loading and corresponding crack surface displacements [*Tada et al.*, 2000]..... 13

Figure 2.3 Arbitrary orientated pressurized inclined crack under far-field stresses..... 17

Figure 2.4 Initiation angle vs. Stress intensity factor ratio (K_I/K_{II})..... 23

Figure 2.5 Stress intensity factor ratio vs. Inclination angle. 23

Figure 2.6 Initiation angle vs. inclination angle for three different criteria. 25

Figure 2.7 Initiation angle vs. Inclination angle at different stress contrast..... 28

Figure 2.8 Breakdown pressure vs. Inclination angle at different stress contrasts..... 28

Figure 2.9 Mode II fracture toughness influence on fracture initiation angle..... 30

Figure 2.10 Mode II fracture toughness influence on breakdown pressure. 30

Figure 2.11 Mode I fracture toughness influence on fracture initiation angle. 31

Figure 2.12 Mode I fracture toughness influence on breakdown pressure..... 31

Figure 2.13 Poisson's ratio influence on fracture initiation angle. 32

Figure 2.14 Schematic of triaxial hydraulic fracturing test system..... 34

Figure 2.15 Experimental sample preparation and setup procedures..... 34

Figure 2.16 Non-twisted fracture propagation when preexisting fracture aligns with fracture orientation. 36

Figure 2.17 Measurement of fracture propagation angle. 38

Figure 2.18 Examples of failed experiment. 38

Figure 2.19 Comparison between theoretical and experimental fracture initiation angles (stress contrast = 3 MPa). 41

Figure 2.20 Comparison between theoretical and experimental fracture initiation angles (stress contrast = 5 MPa). 42

Figure 3.1 Stress distributions on radial cracks emanating from borehole. 45

Figure 3.2 Cracks emanating from borehole under different loadings. 47

Figure 3.3 Comparison of the weight function (WF) based *SIFs* and boundary collocation (BC) based *SIFs* for Fig. 3.2-A (R_w = 1 *m*, *P* = 1 *MPa*). 51

Figure 3.4 Comparison of the WF based *SIFs* and BC based *SIFs* for Fig. 3.2-B (R_w = 1 *m*, σ = 1 *MPa*). 53

Figure 3.5 Loadings on inclined symmetrical radial cracks emanating from circular hole. 54

Figure 3.6 Loadings on symmetrical radial cracks aligning with principal stress. 55

Figure 3.7 BC and WF based *SIFs* when crack aligns with principal stress direction under constant and non-constant pressure loadings. 56

Figure 3.8 WF based *SIFs* for inclined cracks with both constant and non-constant pressures. 58

Figure 4.1 Stress distributions on radial cracks emanating from borehole. 64

Figure 4.2 Effect of dimensionless crack length on breakdown pressure. 70

Figure 4.3 Effect of crack deviation angle on breakdown pressure. 72

Figure 4.4 Effect of in-situ stress contrast on breakdown pressure. 73

Figure 4.5 Effect of fracture toughness on breakdown pressure. 75

Figure 4.6 Effect of pressure distribution inside preexisting fracture on breakdown pressure. 77

Figure 4.7 Breakdown pressure by weight function method (R_w = 0.1 m, θ = 0°). 79

Figure 4.8 Breakdown pressure verification with in-house experimental results. 81

Figure 4.9 Breakdown pressure verification during the first injection with 1 m^3 block (R_w = 0.015 m). 83

Figure 4.10 Breakdown pressure verification during the second injection with 1 m^3 block (R_w = 0.015 m). 84

Figure 4.11 Breakdown pressure verification in the field 85

Figure 5.1 Comparison of different brittleness indices for Barnett shale (the major unit in vertical direction is 100 ft). 95

Figure 5.2 Correlation of brittleness with porosity for Woodford shale. 97

Figure 5.3 Correlation of brittleness with porosity for Barnett shale. 98

Figure 5.4 Correlation of brittleness with porosity for Eagle Ford shale. 99

Figure 5.5 Correlation of brittleness with compressional slowness for Woodford shale. 101

Figure 5.6 Correlation of brittleness with compressional slowness for Barnett shale. 102

Figure 5.7 Correlation of brittleness with *DTC* for Eagle Ford shale. 102

Figure 5.8 Correlation of brittleness with porosity for Woodford, Barnett and Eagle ford shales 104

Figure 5.9 Correlation of brittleness with compressional slowness *DTC* for Woodford, Barnett and Eagle ford shales. 105

Figure 5.10 Correlation of brittleness with compressional slowness *DTC* for Barnett and Eagle ford shales..... 106

Figure 5.11 Prediction of brittleness with local correlation (B_{24}) and global correlation (B_{29}) for Well A of Barnett shale. 107

Figure 5.12 Prediction of brittleness with local correlation (B_{27}) and global correlation (B_{30}) for Well B of Barnett shale. 108

Figure 6.1 Demonstration of anisotropy of rock mechanics property. 113

Figure 6.2 Schematic of fracture barrier. 116

Figure 6.3 A cross plot of brittleness and critical strain energy release rate shows increasing fracability index. 120

Figure 6.4 A cross plot of brittleness and fracture toughness shows increasing fracability index. 121

Figure 6.5 A cross plot of brittleness and Young's modulus shows increasing fracability index. 121

Figure 6.6 Screening hydraulic fracturing candidates with fracability index. 126

Abstract

Production enhancement of tight reservoirs requires in-depth analysis of mechanisms governing hydraulic fracturing, especially in naturally fractured reservoirs. This study is dedicated to the optimization of hydraulic fracturing and drilling by integrating both rock fracture mechanics and petrophysics study.

Fracture twist near the borehole adversely impair production rate or induce premature screenout, and is analyzed in terms of mixed-mode fracture propagation. The best fracture propagation criterion is selected by comparing experimental and theoretical fracture initiation angles, suggestions regarding the alleviation of fracture twist are summarized by sensitivity analysis.

Accurate estimation of fracture gradient is critical for both drilling and hydraulic fracturing. Fracture gradient by traditional methods is greatly overestimated due to the ignorance of preexisting fractures, nonlinear near wellbore stress concentration acting on fracture surfaces, and nonlinear fluid pressure distribution inside fractures. A weight function method is firstly introduced to petroleum engineering for the calculation of stress intensity factor where there are preexisting fractures intersecting borehole. Weight function parameters of a pair of symmetrical fractures emanating from borehole are derived and verified against existing models. The weight function parameters are applied to predict breakdown pressure of preexisting fractures. The simulation results are compared against both measured breakdown pressure in both fields and laboratory and results of classical fracture models. The proven weight function method shows a great potential in improving the accuracy of breakdown pressure prediction.

Screening fracture candidates plays a central role in hydraulic fracturing design. Identification of fracture barrier helps prevent freshwater aquifer from contamination

and undesirable water breakthrough due to unintentional cross of fracture barriers. New definition of brittleness is developed and benchmarked for unconventional shale. Correlations of brittleness with neutron porosity and compressional slowness are built for predicting brittleness in the fields lacking specific logging data, and saving cost of logging service. Fracability index model is firstly developed for screening fracturing candidates and fracture barrier identification by integrating brittleness and fracture energy (or fracture toughness, Young's modulus, tensile strength). Its interpretation result is proven by logging interpretation. It is found that it is not always right that formations with high brittleness are good fracturing candidates. The fracability index model refines the formation evaluation and narrows the thickness of target interval.

This research establishes a comprehensive understanding regarding fracture twist, mixed-mode fracture propagation, fracture gradient prediction, fracturing candidate selection by integrating theoretical modeling, experimental efforts, and logging interpretation. The methodologies will not only help engineers improve hydraulic fracturing design, but also provide evidence and theoretical support for explaining previously failed cases.

Chapter 1. Introduction

1.1 Overview of Geomechanics in Unconventional Shale

Geomechanics plays a critical role throughout the life of a reservoir. A comprehensive geomechanics analysis can reduce nonproductive time, enhance risk management (e.g., oil spill, blowout, platform subsidence, etc.), boost production rate, extend the life of reservoir, and ultimately enhance hydrocarbon recovery [*Fjar et al.*, 2008]. At the stage of exploration, geomechanics is applied to predict pore pressure in reservoir scale [*Dutta*, 2002; *Sayers, Johnson and Denyer*, 2002]. At the stage of drilling, geomechanics analysis encompasses in-situ stresses estimation [*Haimson*, 1968; *Abou-Sayed, Brechtel and Clifton*, 1978], pore pressure prediction [*Eaton*, 1975; *Peng and Zhang*, 2007; *Zhang*, 2011], fracture gradient estimation [*Matthews and Kelly*, 1967; *Eaton*, 1969], casing point selection [*Willson, Fossum and Fredrich*, 2003; *Zhang*, 2011], wellbore strengthening simulation [*Wang, Soliman and Towler*, 2009], wellbore stability analysis (e.g., severe problems occurs in reactive shale and salt dome) [*Li, Cui and Roegiers*, 1998; *Ghassemi et al.*, 1999; *Zhang, Bai and Roegiers*, 2003], optimization of drilling trajectory [*Zoback*, 2010], waste solid and fluid re-injection [*Dusseault*, 2010], and so on. At the stage of well completion, geomechanics analysis encompasses optimization of perforation design (e.g., location selection, orientation, phasing, density, perforation clusters spacing, penetration depth, perforation diameter, etc.) for sand control and hydraulic fracturing [*Fjar et al.*, 2008], prediction of critical pressure drawdown and flow rate for sand control [*Perkins and Weingarten*, 1988; *Weingarten and Perkins*, 1995; *Ewy et al.*, 2001; *Yi, Valko and Russell*, 2004], breakdown pressure prediction [*Detournay and Carbonell*, 1997; *Jin et al.*, 2013], and so on. At the stage of reservoir development, geomechanics analysis focuses on fault

reactivation [*Wiprut and Zoback*, 2000], caprock integrity in the development of heavy oil [*Collins*, 2005; *Ghannadi, Irani and Chalaturnyk*, 2013], reservoir compaction and subsidence [*Settari and Walters*, 2001], and so on. Significant improvements in drilling and production have been achieved by successful implementation of geomechanics. Therefore, geomechanics has become a central and essential part throughout the life an oil field.

With the recent boom in the development of unconventional shale gas and tight oil, geomechanics has attracted more attention than ever before because of the complexities and sensitivities of rock properties in these reservoirs [*Abousleiman et al.*, 2007; *Britt and Schoeffler*, 2009; *Ge and Ghassemi*, 2011; *Li and Ghassemi*, 2012]. The richness of reactive clay in shale formation leads to hydration problem, which has been studied by coupled Porochemothermoelastic simulation [*Nguyen and Abousleiman*, 2009]. Shale formation is also rich in natural fractures, which leads to anisotropic properties [*Hornby, Schwartz and Hudson*, 1994]. Both image logging and laboratory testing have been conducted to investigate anisotropic characteristics of shale [*Moran and Gianzero*, 1979; *Esmersoy et al.*, 1994; *Tran*, 2009; *Sierra et al.*, 2010]. The preexisting fracture intersecting borehole may reduce breakdown pressure and fracture gradient, thus narrow the mud density window. Ultimately the borehole wall might be fractured due to the overestimation of breakdown pressure by traditional methods. The induced fracture leads to extra mud invasion to the formation, increased skin factor, and may adversely affect cementing quality [*Jin et al.*, 2013]. Both horizontal drilling and multi-stage hydraulic fracturing are critical for the success of shale play [*King*, 2012]. In order to create transverse vertical fractures, it is suggested to drill a horizontal well in

the direction of minimum horizontal stress [*Valkó and Economides*, 1995]. Horizontal planar fracture is of no economic value due to low vertical permeability, so shale plays in the reverse fault region are not good candidates for hydraulic fracturing. For example, one shale play of Shell Oil Company in Sichuan Province, China (tectonic stresses in Sichuan area are severely perturbed by mountains) cannot be fractured effectively because horizontal planar fractures occurred [*Yuan et al.*, 2013].

Fracture twist near the wellbore is undesirable in hydraulic fracturing, and it becomes severe in formation of high stress anisotropy. Mixed-mode fracture propagation in ductile shale is different from that in brittle formation [*Jin, Shah and Sheng*, 2012]. Perforation design is optimized to alleviate fracture tortuosity near wellbore and prevent premature screenout [*Daneshy*, 2013]. When the neighboring propagating fractures are too close, they may interact with each other due to the influence of disturbed stress field near the fracture tip, which is called "stress shadowing" and has been investigated extensively in recent years [*Olson*, 2008; *Nagel and Sanchez-Nagel*, 2011]. Recommendations regarding the optimization of perforation cluster spacing and density are provided to avoid stress shadowing and maximize *SRV* (stimulated reservoir volume) [*Fisher et al.*, 2002; *Fisher et al.*, 2004]. Interaction between propagating and preexisting natural fractures is studied to understand the formation of fracture network [*Blanton*, 1982; *Potluri, Zhu and Hill*, 2005]. Fracture propagation at the interface of bedding planes is studied to understand the behavior of fracture in layered formation [*Daneshy*, 1978]. Whether the propagating fracture will cross or detour the preexisting fracture, whether fracture will propagate along the interface between the beddings or breakthrough them, all depend on the stress field near

fracture tip, difference of rock mechanical properties, and the selection of propagation criterion.

In conclusion, the study of geomechanics is significant in the development of oil and gas, especially in unconventional shale. The boom of unconventional shale has made rock fracture mechanics more popular than at any time in history.

1.2 Overview of Petrophysics in Unconventional Shale

The study of petrophysics is critical for the success of unconventional shale [*Sondergeld et al.*, 2010], and the measurement of petrophysical properties are quite different from that of conventional reservoirs because of its special nano-scale properties [*Josh et al.*, 2012]. For example, porosity of tight shale is measured by *GRI* crushed powder method [*Luffel and Guidry*, 1992], which does not represent real porosity but is the only available method that can reduce turnaround time in shale testing. Permeability of tight shale cannot be measured by conventional permeameter due to nanodarcy property, but can be measured by pressure-pulse decay method [*Luffel, Hopkins and Schettler*, 1993], which is expensive and time consuming. Recently, digital rock technology has emerged and provided one more option for porosity and permeability estimations, and examining microstructure of tight shales [*Berryman and Blair*, 1986; *Knackstedt et al.*, 2009]. This method may help to reduce the turnaround time of shale permeability and porosity tests, but is not an affordable technique, and is still at developing stage, needs more work to improve its reliability and accuracy. For a two-phase fluid flow with water and gas, relative permeability of gas reduces abruptly after water breakthrough, so the analysis of water saturation and capillary pressure is important for preventing water production and extending the period

of high gas production [*Thomas and Ward*, 1972; *Tiab and Donaldson*, 2011]. Considering the difficulty and complexity of coring in shale formation, methods and devices have been developed to measure rock mechanical properties (e.g., Young's modulus, Poisson's ratio, shear strength, hardness, etc.) on drilling cuttings or broken cores [*Brook*, 1977; *Ulm and Abousleiman*, 2006; *Abousleiman et al.*, 2007; *Kumar*, 2012]. A variety of methods (e.g., logging based, laboratory measurement, etc.) have been developed to determine *TOC* (Total Organic Content) [*Fertl and Chilingar*, 1988; *Passey et al.*, 1990], but field practice indicates that there is no universal method. The preexisting natural fractures are common in shale reservoirs and are critical for enhancing permeability, so the understanding of natural fracture density, dipping angle, location, and aperture width is important [*Curtis*, 2002; *Gale and Holder*, 2010]. High-resolution image logging and *CT* scan technique have been applied widely for the characterization of natural fracture system [*Kemeny and Post*, 2003; *Gale, Reed and Holder*, 2007]. Brittleness has been a favorable parameter for screening fracturing candidates, so mineralogical logging and *XRD* tests are suggested to be conducted in shale plays. To estimate breakdown pressure in both drilling and hydraulic fracturing, fracture toughness measurement is required and the results show strong anisotropy [*Sierra et al.*, 2010]. Better management of breakdown pressure can help reshape mud density window, and estimate the required horse power on surface to fracture the formation. Proppant embedment is another important property in fracturing evaluation. If proppant strength is greater than that of shale formation, proppant may embed into fracture surface, and thus reduce effective fracture width; otherwise, it might be crushed, and thus reduces effective fracture width [*Montgomery and Steanson*, 1985].

Therefore, the selection of proper proppant size and strength is important for ensuring long-term high fracture conductivity.

In conclusion, petrophysical analysis is necessary for the success of unconventional shale. Improper interpretation of petrophysical results may lead to non-affordable decision in production.

1.3 Problem Statement

After an overview of the Geomechanics and Petrophysics applications in unconventional shale, a general understanding about present research interests is established. The objective is to better understand the challenges in shale development and come up efficient solutions by integrating geomechanical and petrophysical mythologies. However, it is hard to encompass all the topics in one dissertation due to the limitations of facility, time, and funding. Therefore, only several topics related to fracture are studied in the dissertation.

Hydraulic fracturing modeling is one important aspect in the optimization of hydraulic fracturing design. Traditional 2-D planar fracture propagation models, such as *PKN*, *KGD* models, etc., cannot meet the demands of current fracturing simulator [*Perkins and Kern*, 1961; *Geertsma and De Klerk*, 1969; *Nordgren*, 1972]. Numerical methods, such as finite element method, boundary element method, extended finite element method, discrete element method, discrete fracture network, and so on, have been applied in fracture propagation simulation [*Gong et al.*, 2011; *Huang, Zhang and Ghassemi*, 2012; *Olson and Wu*, 2012; *Sheng et al.*, 2012; *Wu and Olson*, 2013]. It is found that σ_θ-criterion (maximum tangential stress criterion) is one preferred criterion in most fracture propagation simulations, but no evidence proves the simulated fracture

paths by σ_θ-criterion are close to experimental observations in hydraulic fracturing. Therefore, it is important to figure out which criterion generates fracture path matching the experimental results better. In addition, usually the preexisting fracture (perforation and natural fractures are assumed as preexisting fracture in the dissertation) orientation does not align with the principal stress direction [*Ingraffea*, 1981]. The shear stress acting on the inclined fracture surface leads to the change of fracture propagation orientation [*Jin and Shah*, 2013]. The co-existence of shear and normal stresses in hydraulic fracturing forms mixed-mode fracture propagation, which leads to the undesirable fracture twist near borehole. However, fracture initiation angle of mixed-mode fracture propagation is not available due to the complexity in solving non-linear equations. Therefore, another objective of this dissertation is to explore the fundamental mechanisms governing fracture twist by solving the nonlinear equations of fracture initiation angle numerically.

Fracture gradient prediction is important for both drilling and hydraulic fracturing, but there is no much progress in the prediction methods since 1960s. The methods based on continuum mechanics does not account for the preexisting fractures intersecting borehole, and overestimates fracture gradient in naturally fractured formations [*Hubbert and Willis*, 1957; *Haimson and Fairhurst*, 1967; *Detournay and Carbonell*, 1997]. To manage fracture gradient better, fracture mechanics approach is introduced to fracture gradient calculation [*Barry, Whittaker and Singh*, 1992]. However, the existing fracture approaches do not account for near wellbore stress concentration, uncertainty of preexisting fracture length and orientation, nonlinear pressure distribution inside preexisting fracture. Rummel's fracture mechanics approach

attempts to address these shortcomings, but it does not account for deviation angle between fracture and principal stress, and the solutions are not independent of external loadings[*Rummel*, 1987; *Rummel and Hansen*, 1989]. A *WF* (weight function) method is introduced to fracture gradient prediction because it can overcome all the limitations mentioned earlier [*Glinka and Shen*, 1991]. But the *WF* parameters are not available for calculating *SIF* (stress intensity factor) of fractures emanating from borehole. Therefore, another objective of the dissertation is to derive weight function based *SIF* of fractures emanating from borehole, calculate fracture gradient by the *WF* method, and illustrate its advantages by comparing with traditional methods.

The screening of fracture candidate and identification of fracture barrier are significant for hydraulic fracturing design. Brittleness has been assumed as an indicator of fracability in shale reservoirs [*Rickman et al.*, 2008; *Li et al.*, 2013]. A variety of methods have been developed for defining brittleness, the most popular ones are Rickman's brittleness [*Rickman et al.*, 2008] and mineralogical brittleness [*Jarvie et al.*, 2007; *Wang and Gale*, 2009]. However, there is no universal agreement regarding which definition properly describe rock brittleness [*Hucka and Das*, 1974]. It is also observed that rock brittleness affect drillability (drillability is penetration rate during drilling measured in the unit of feet per minute), and it is observed that drillability decreases with increasing brittleness [*Yarali and Kahraman*, 2011]. Therefore, another objective is to benchmark brittleness definitions. It is observed that not all wells have mineralogical logging and shear slowness, which restricts the application of mineralogical brittleness and brittleness based on dynamic Young's modulus and

Poisson's ratio. Therefore, another objective is to develop high-quality correlations between mineralogical brittleness and other cheap and easy accessible data.

Brittleness alone as a fracability indicator has some shortcomings in formation evaluation. For example, formation with relatively high brittleness might not be good fracture candidate, such as pure limestone (fracture is not easy to be initiated because of its larger fracture toughness), because brittleness does not represent rock strength. Parameters such as closure stress, fracture toughness, bonding strength, etc., have been used as indicators of fracture barrier [*Simonson, Abou-Sayed and Clifton*, 1978; *Ham*, 1982]. For example, formation with high closure stress is considered as fracture barrier because higher fracturing pressure is required to create new fractures in fracture barrier than in adjacent formations. However, these rock mechanics parameters do not suggest how easy to form fracture network. Although pumping pressure is enough to fracture the formation, if its brittleness is relatively low, fracture propagation is slow and fracture network is not easy to form. Therefore, the last objective of the dissertation is to develop a new fracability evaluation model for screening fracture candidates and barriers by integrating both brittleness and rock strengths.

1.4 Dissertation Overview

Hydraulic fracturing has been a popular topic in both industry and academic since the boom of unconventional shale. Petroleum engineers and scientists have learned a lot from shale development experience in the *past 15+* years [*King*, 2012], but there are still challenges due to insufficient understanding about the fundamental mechanisms. In order to improve the efficiency of hydraulic fracturing, this dissertation focuses on integrated geomechanics and petrophysics studies related to hydraulic

fracturing and drilling. The major body of the dissertation is divided into two parts: the first part addresses challenges related to rock fracture mechanics (chapters 2, 3 and 4). The second part addresses the principles of fracturing candidate/barrier selection (chapters 5 and 6).

Chapter 2 studies fracture twist near wellbore by developing a mixed-mode fracture propagation model. The fracture propagation criterion generating fracture initiation angles the closest to experimental observations is selected by comparing theoretical and measured fracture initiation angles. **Chapter 3** introduces *WF* method for the calculation of *SIF* in petroleum engineering. Weight function parameters are derived for fractures emanating from borehole. Weight function based *SIFs* are proven with formulas in the handbook of *SIF*. Its advantages are demonstrated by varying fracture orientation, length, and pressure distribution inside fracture. **Chapter 4** applies the proven *WF* based *SIF* to calculate breakdown pressure where there are preexisting fractures intersecting borehole. Breakdown pressure by *WF* method is compared against results by both *PSA* and Rummel's methods. The *PSA* method is developed by **P**aris and **S**ih [*Paris and Sih*, 1965], and applied to petroleum engineering by **A**bou-Sayed [*Abou-Sayed, Brechtel and Clifton*, 1978]. The comparison not only proves the validity of weight function method in breakdown pressure calculation, but also demonstrates its advantages over both methods. Sensitivity studies are conducted to find major factors (such as preexisting fracture length, orientation, stress contrast, fracture toughness, and internal pressure distribution) influencing breakdown pressure. **Chapter 5** addresses present disagreement regarding the definitions and measurements of brittleness by introducing a new definition of brittleness, and benchmarking it with two other

independent methods. High-quality correlations between mineralogical brittleness and compressional slowness, neutron porosity are developed and proven with field data. The correlations enable the prediction of brittleness in the field without mineralogical logging and shear slowness. **Chapter 6** addresses the limitations of brittleness alone as an indicator of fracturing candidate by integrating brittleness and fracture toughness (or fracture energy, Young's modulus, tensile strength). The integrated approach has great potential in the optimization of horizontal drilling and hydraulic fracturing.

In conclusion, the dissertation makes contributions to hydraulic fracturing by integrating rock fracture mechanics and petrophysics, and adapting mature theory from other disciplines to hydraulic fracturing.

Chapter 2. Mixed-Mode Fracture Propagation in Hydraulic Fracturing: Theoretical Analysis and Experimental Verification

2.1 Introduction

In recent years, horizontal multi-stage hydraulic fracturing completions have become prevalent in the development of tight reservoirs, such as tight gas sand, shale gas, and tight oil. In order to create multiple transverse fractures, it is suggested to drill a well in the minimum horizontal in-situ principal stress direction [*Soliman, Hunt and El Rabaa*, 1990; *El Rabaa*, 1998], but from a practical viewpoint, it is not easy to control drilling orientation in complex geological environment [*Fritz, Horn and Joshi*, 1991]. The inclination angle β between the direction of horizontal well and minimum horizontal in-situ principal stress leads to nonplanar fracture propagation from horizontal well [*Abass, Hedayati and Meadows*, 1996; *Daneshy*, 2013], as is demonstrated in Fig. 2.1-A. As for the hydraulic fracturing of vertical wells, if the perforation orientation does not align with the direction of maximum horizontal in-situ principal stress, it also leads to a fracture twist near borehole [*Yew*, 1997], as is shown in Fig. 2.1-B. Hence, such stimulations imply mixed-mode (opening and sliding modes) fracture initiation. Opening mode contributes to fracture opening, and sliding mode contributes to fracture reorientation from the preexisting fracture. Fracture twist near the wellbore might lead to proppant bridging, premature screenout, decreased fracture width, and increased skin[1] [*Cleary et al.*, 1993; *Khan and Khraisheh*, 2000; *Jin, Shah and Sheng*, 2012].

[1] Hydrocarbon flowing inside the tortuous fracture experiences extra pressure loss.

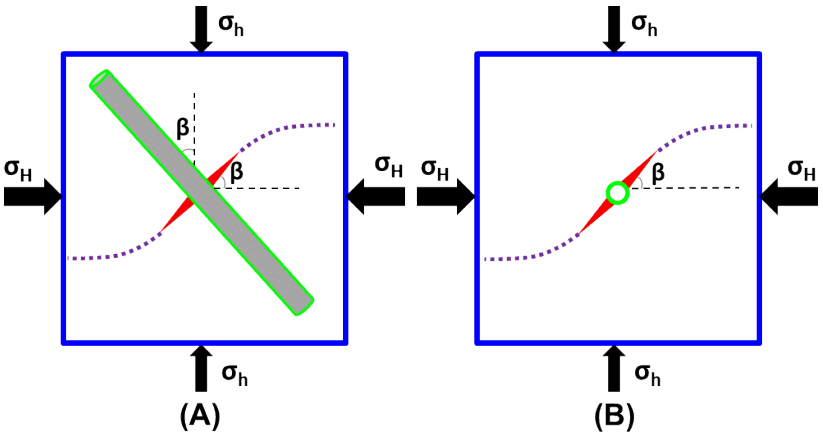

Figure 2.1 Top views of fracture propagation near horizontal (A) and vertical (B) wells.

The triangle emanating from borehole represents the preexisting fracture, which is magnified for visualization.

Fracture propagation usually includes a mix of three basic fracture modes, as shown in Fig. 2.2. Fractures of Mode I and II are the two primary types in hydraulic fracturing. As a result, this paper will focus on mixed modes of I and II.

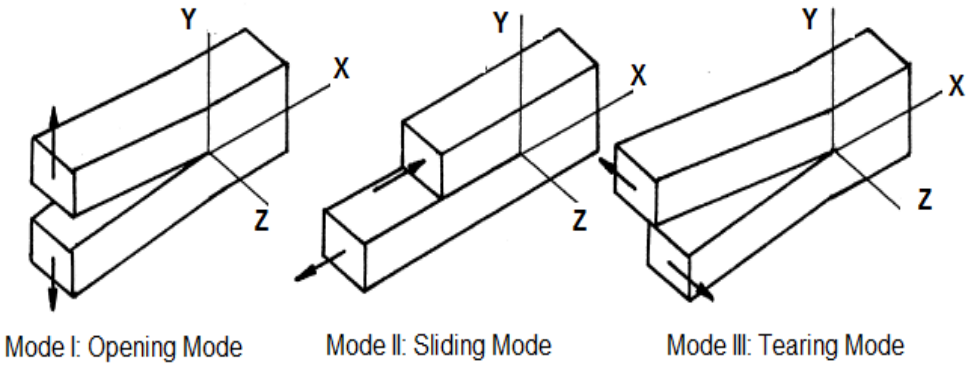

Figure 2.2 Three basic fracture modes of loading and corresponding crack surface displacements [*Tada et al.*, 2000].

Fracture propagation of an inclined crack under uniaxial loading has been studied with three fracture propagation criteria (Maximum Tangential Stress Criterion

(σ_θ-Criterion), Maximum Energy Release Rate (G-Criterion), and Minimum Strain Energy Density (S-Criterion)), and with a limited number of experiments to verify fracture propagation in rocks. It is concluded that there is no difference in results by the three criteria [*Ingraffea,* 1977]. In addition, fracture propagation under biaxial loading is not investigated, and the new fracture is not induced by fracturing fluid, but by the tensile stress. Mixed-mode fracture initiation angle under different loadings is analyzed systematically [*Khan and Khraisheh,* 2000], but the pressurized preexisting fracture and determination of breakdown pressure are not considered. Stress intensity factors of preexisting pressurized cracks are available [*Rice,* 1968a; *Abou-Sayed, Brechtel and Clifton,* 1978], but solutions of mixed-mode fracture initiation angles are unavailable due to the complexity in solving the nonlinear equations. σ_θ-Criterion has been applied extensively in simulating fracture propagation path owing to its simplicity [*Belytschko and Black,* 1999; *Moes, Dolbow and Belytschko,* 1999; *Zhang et al.*, 2011; *Olson and Wu,* 2012], but limited hydraulic fracturing experiments have proven fracture path predicted by σ_θ-Criterion is close to observed results. Hydraulic fracturing experiments are conducted with different types of rock to study fracture initiation pressure, propagation orientation, and its potential in determining in-situ principal stresses [*Haimson,* 1968]; However, the induced fracture is not initiated from a preexisting fracture, but from an intact wellbore. The breakdown pressure is determined based on Griffith's criterion, which assumes fracture is initiated when maximum tangential stress on borehole wall reaches apparent tensile strength [*Griffith,* 1921; *Fjar et al.,* 2008]. If it is an intact vertical borehole wall in homogeneous formation, the orientation of fracture initiation is the maximum horizontal principal stress direction [*Peng and*

Zhang, 2007]. In addition, the tensile failure criterion proven by Haimson is different from σ_θ-Criterion used in fracture mechanics. Tensile failure uses tangential stress near a borehole, while σ_θ-Criterion uses tangential stress near fracture tip. Experimental investigation is also conducted to study hydraulic fracturing through perforations [*Daneshy*, 1973], but the length of perforation is in the stress concentration region near wellbore due to short perforation length. Other hydraulic fracturing experiments have also been conducted to study fracture propagation [*Haimson*, 1981; *Abass, Hedayati and Meadows*, 1996; *El Rabaa*, 1998; *Zhou et al.*, 2008; *Chen et al.*, 2010; *Germanovich et al.*, 2012; *Ispas et al.*, 2012], but limited in-depth analysis is provided to the selection of mixed mode fracture propagation criterion.

In present study, a 2-D plane strain hydraulic fracturing model is developed to investigate fracture propagation with the three criteria mentioned earlier. The breakdown pressure in mixed mode fracture propagation is calculated by assuming the associate curve of K_I and K_{II} is an ellipse. A modified bisection method is developed to solve the nonlinear equations of fracture initiation angle. The relationship between fracture initiation angle θ_m and inclination angle β of preexisting fracture is discussed in terms of *SIF* ratio. The influence of in-situ principal stress anisotropy, breakdown pressure, mode-I and II fracture toughness, and Poisson's ratio on fracture propagation is analyzed. Fracture initiation angles at different inclination angles (15°, 30°, 45°, and 60°) and stress anisotropy are measured in a series of realistic triaxial hydraulic fracturing experiments. The best criterion for predicting fracture propagation in hydraulic fracturing is selected by comparing experimental and theoretical fracture

initiation angles. Recommendations regarding the optimization of drilling and hydraulic fracturing are also provided.

2.2 Methodology

2.2.1 Stress Intensity Factors for a Preexisting Inclined Fracture

Two types of preexisting inclined fracture are considered here: perforation and natural fracture. The cone-shaped perforation geometry with tapered tip has been observed in the laboratory for years [*Ansah, Proett and Soliman*, 2002], so perforation geometry in a 2-D model is assumed to be sharp-tip fracture as depicted in Fig. 2.3. The penetration depth is about ten times the borehole radius, for example, if borehole radius is about 0.05 m, penetration depth is about 0.5 m [*Stenhaug et al.*, 2003]. For an open hole, stress concentration is negligible in the region outside about five times the borehole radius [*Haimson*, 1968]. Stress concentration region becomes smaller after setting casing because the strength of casing is much higher than that of rock. It is assumed here the length of preexisting fracture is at least five times borehole radius for an open hole, and at least three times wellbore radius for a cased hole. Therefore, near wellbore stress concentration is ignored in the calculation of *SIF* for the pressurized preexisting fracture. The hydraulic fracturing model is simplified as demonstrated in Fig. 2.3.

The net normal and shear stresses acting on the faces of preexisting inclined fracture are (tensile stress is assumed positive):

$$\sigma_n = P - \sigma_H \sin^2 \beta - \sigma_h \cos^2 \beta \tag{2.1}$$

$$\tau = \frac{1}{2}(\sigma_H - \sigma_h) \sin 2\beta \tag{2.2}$$

where, σ_n is normal stress, τ is shear stress, P is fluid pressure inside fracture, σ_H and σ_h are maximum and minimum horizontal in-situ stresses, β is inclination angle between fracture orientation and maximum horizontal in-situ stress, a is half-fracture length.

.

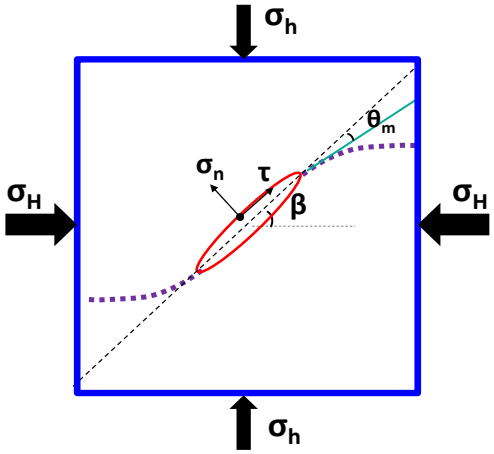

Figure 2.3 Arbitrary orientated pressurized inclined crack under far-field stresses. The width of preexisting fracture is magnified for visualization.

Stress intensity factor is a parameter used to predict the stress state in the vicinity of a crack tip caused by a remote loading or residual stresses [*Anderson*, 2005]. *SIFs* for mode-I and II fractures are defined as:

$$K_I = Y_1 \sigma_n \sqrt{\pi a} \tag{2.3}$$

$$K_{II} = Y_2 \tau \sqrt{\pi a} \tag{2.4}$$

where, K_I and K_{II} are mode-I and II *SIFs*, Y_1 and Y_2 are shape factors for different fracture geometry, σ_n is normal stress, τ is shear stress, and a is half-fracture length.

Generally, Y_1 and Y_2 are equal for through cracks and edge crack in an infinite body [*Tada et al.*, 2000]. The shape factors are included as coefficients in the calculation of fracture initiation angle, but get canceled because the first derivatives of

tangential stress, energy release rate, and strain energy density with respect to fracture initiation angle is equal to zero. For convenience, Y_1 and Y_2 are assumed to be unity.

As a result, the *SIFs* of the arbitrary inclined crack reduce down to [*Rice*, 1968a; *Barry, Whittaker and Singh*, 1992]:

$$K_I = (P - \sigma_H \sin^2 \beta - \sigma_h \cos^2 \beta)\sqrt{\pi a} \tag{2.5}$$

$$K_{II} = \frac{1}{2}(\sigma_H - \sigma_h) \sin 2\beta \sqrt{\pi a} \tag{2.6}$$

2.2.2 Determination of Breakdown Pressure for Mixed-Mode Fracture Propagation

The critical value of *SIF* is fracture toughness, which is expressed as K_{IC} and can be measured in the laboratory [*Zhao and Roegiers*, 1993; *Anderson*, 2005]. Fracture toughness is a rock mechanics property measuring the resistance of a flawed sample to fracture propagation [*Rossmanith*, 1983]. For mode-I fracture, crack initiation occurs once *SIF* reaches fracture toughness [*Bower*, 2011],

$$K_I = K_{IC} \tag{2.7}$$

One must be aware that fracture toughness is not an intrinsic rock property, and there is a discrepancy between the measured values in the laboratory and field [*Shlyapobersky, Wong and Walhaug*, 1988; *Zhao and Roegiers*, 1993]. Sample volume, confining pressure, temperature, fluid lag, and nonlinear elasticity are major factors influencing fracture toughness [*Shlyapobersky, Wong and Walhaug*, 1988; *Jeffrey*, 1989; *Roegiers*, 1989; *Gardner*, 1992; *Zhao and Roegiers*, 1993; *Al-Shayea, Khan and Abduljauwad*, 2000]. In practice, one needs to multiply the measured K_{IC} by a coefficient (usually > 1) so that relatively accurate results can be obtained from the fracturing model.

According to modified Griffith energy approach [*Irwin*, 1957], crack initiation from preexisting fracture occurs when strain energy release rate reaches its critical value G_C, which is considered as a characteristic material constant and does not vary with fracture mode. The formula of G_C is as follows:

$$K_I^2 + K_{II}^2 = E'G_C \tag{2.8}$$

where, *E'* is general expression of Young's modulus. It is different for plane stress and strain problems.

The modified Griffith energy approach draws the conclusion that $K_{IC} = K_{IIC}$, which is contrary to experimental results (in the laboratory, it is found that $K_{IIC} = 1.1 \sim 3.0\ K_{IC}$) [*Ingraffea*, 1981; *Al-Shayea, Khan and Abduljauwad*, 2000; *Rao et al.*, 2003; *Backers*, 2005]. Therefore, the modified Griffith energy approach is not applicable for mixed-mode fracture propagation. The analysis of mixed-mode fracture in experiments indicated that the associate curve of K_I and K_{II} is an ellipse [*Miller*, 2000].

$$\left(\frac{K_I}{K_{IC}}\right)^2 + \left(\frac{K_{II}}{K_{IIC}}\right)^2 = 1 \tag{2.9}$$

Equation 2.7 is a special case of Eq. 2.9 when $\frac{K_{II}}{K_{IIC}} \to 0$; Eq. 2.8 is the other special case of Eq. 2.9 when $K_{IC} = K_{IIC}$.

Substituting Eqs. 2.5 and 2.6 into Eq. 2.9, breakdown pressure, P_b at which mixed-mode fracture initiation occurs is obtained as follows,

$$P_b = \frac{K_{IC}\sqrt{1-\left[\frac{\frac{1}{2}(\sigma_H-\sigma_h)\sin 2\beta\sqrt{\pi a}}{K_{IIC}}\right]^2}}{\sqrt{\pi a}} + \sigma_H \sin^2\beta + \sigma_h \cos^2\beta \tag{2.10}$$

If K_{IC} and K_{IIC} are assumed to be equal, according to Eq. 2.10, breakdown pressure will be underestimated.

2.2.3 Stress Field near Fracture Tip for Inclined Fracture in Polar Coordinate System

The following basic equations for stress field near crack tip are well-established [*Zehnder*, 2012].

$$\begin{bmatrix}\sigma_r\\ \sigma_\theta\\ \sigma_{r\theta}\end{bmatrix} = \frac{K_I}{\sqrt{2\pi r}}\cos\frac{\theta}{2}\begin{bmatrix}1+\sin^2 2\theta\\ \cos^2 2\theta\\ \sin\frac{\theta}{2}cos\frac{\theta}{2}\end{bmatrix} + \frac{K_{II}}{\sqrt{2\pi r}}\begin{bmatrix}\sin\frac{\theta}{2}(1-3\sin^2\frac{\theta}{2})\\ -3\sin\frac{\theta}{2}cos^2\frac{\theta}{2}\\ \cos\frac{\theta}{2}(1-3\sin^2\frac{\theta}{2})\end{bmatrix} \quad (2.11)$$

$\sigma_z = \upsilon(\sigma_r + \sigma_\theta)$ for plane strain; (2.12)

where, σ_r is radial stress near crack tip, σ_θ is tangential stress near crack tip, $\sigma_{r\theta}$ is shear stress near crack tip, σ_z is vertical stress near crack tip, υ is Poisson's ratio, and θ is clockwise direction referred to perforation/crack axis in polar coordinates. Equation 2.11 is in polar coordinate system, clockwise direction is negative.

2.2.4 Fracture Propagation Criteria

The propagation path of a hydraulic fracture cannot be predicted without the knowledge of fracture initiation angle at each step. After calculating mode-I and II *SIFs*, breakdown pressure, and stresses near crack tip, fracture initiation angle can be predicted with proper fracture propagation criteria. The three criteria considered in fracture propagation are:

- Maximum tangential stress criterion, which is called σ_θ-Criterion [*Erdogan and Sih*, 1963].

- Maximum energy release rate criterion, which is called G-Criterion [*Hussain*, 1974].
- Minimum strain energy density criterion, which is called S-Criterion [*Sih*, 1974].

The solution of fracture initiation angle of mixed-mode fracture propagation in hydraulic fracturing by the above criteria is presented in Appendices A through C. The details of the modified bisection method employed in solving nonlinear equations of fracture initiation angle are shown in Appendix D.

2.3 Theoretical Solutions

2.3.1 The Relationship between Fracture Initiation Angle and Stress Intensity Factor Ratio

The relationship between fracture initiation angle and *SIF* ratio is given in Eq. A-3, and is plotted in Fig. 2.4. It is observed that the absolute value of fracture initiation angle (used for the comparison in the following sections) decreases with increasing *SIF* ratio and approaches to zero at infinite *SIF* ratio.

Employing parameters listed in Table 2.1, *SIF* versus fracture inclination angle is plotted in Fig. 2.5. It can be seen in Fig. 2.5 that when inclination angle β is between 0°- 8° or 82°-90°, *SIF* ratio K_I/K_{II} is big, which means the opening mode is dominating, fracture will not twist much and fracture initiation angle is small (Fig. 2.4 indicates fracture initiation angle decreases gradually to zero with increasing *SIF* ratio). As the *SIF* ratio goes to minimum (β = 45° in Fig. 2.5), sliding mode dominates fracture propagation, and fracture initiation angle reaches its maximum value (Fig. 2.4 indicates that fracture initiation angle is big at small *SIF* ratio). Special attention should be paid as β approaches 45° because fracture twist in this case is the most, which may lead to

the a risk of premature screenout and increased pressure drawdown near borehole. As fracture propagates gradually and orientates perpendicular to the minimum principal stress, inclination angle β approaches zero, *SIF* ratio K_I/K_{II} approaches infinity, and then fracture initiation angle will be nearly zero. This means fracture will ultimately propagate along a vertical plane perpendicular to the minimum horizontal in-situ principal stress after experiencing a twist near the wellbore.

Table 2.1 Basic parameters for the prediction of fracture initiation angle

Parameter	**Value**
Maximum Horizontal Stress: σ_H	20.0 *MPa*
Minimum Horizontal Stress: σ_h	15.0 *MPa*
Preexisting Fracture Length: a	0.5 *m*
Mode-I Fracture Toughness: K_{IC}	3.0 $MPa \cdot m^{1/2}$
Mode-II Fracture Toughness: K_{IIC}	7.5 $MPa \cdot m^{1/2}$
Poisson's Ratio: v	0.25

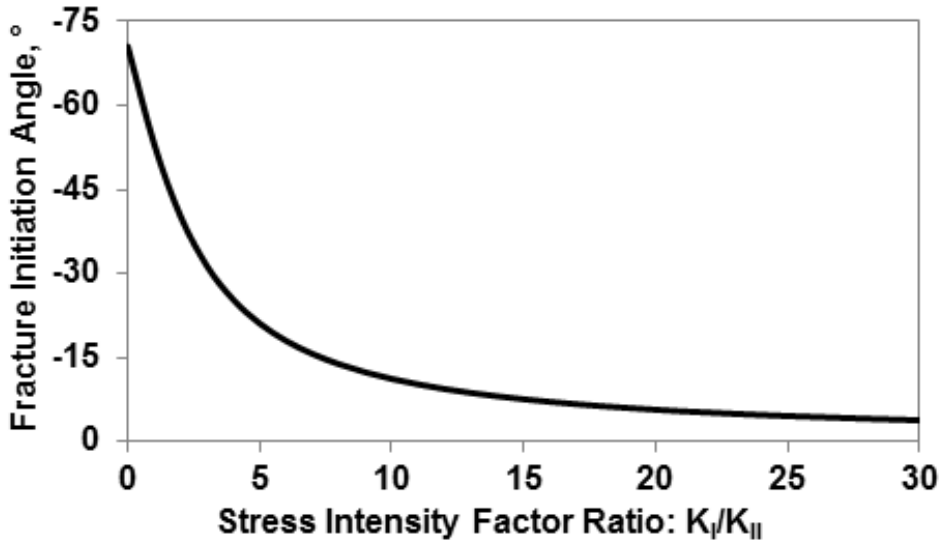

Figure 2.4 Initiation angle vs. Stress intensity factor ratio (K_I/K_{II}).

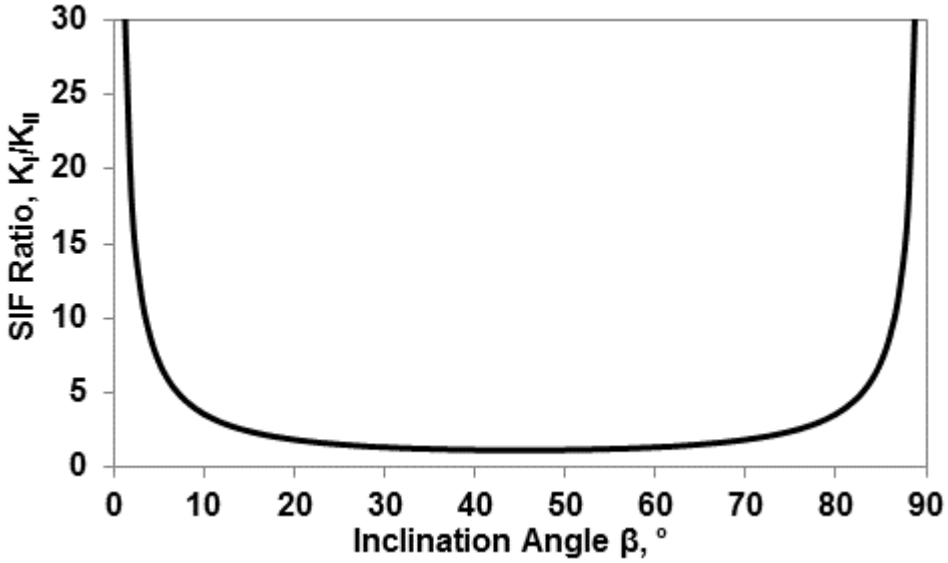

Figure 2.5 Stress intensity factor ratio vs. Inclination angle.

2.3.2 Comparison of Fracture Initiation Angles for Different Fracture Propagation Criteria

One of the objectives of this study is to highlight the differences in fracture initiation angle by using the three classical propagation criteria. Analytical solution is only available for the σ_θ-criterion. A modified bisection method is developed to solve the nonlinear equations of fracture initiation angle for G-Criterion and S-Criterion. The details of the algorithm are described in Appendix D. The basic input is listed in Table 2.1. The relationship between fracture initiation angle and inclination angle for a pressurized preexisting inclined crack is plotted in Fig. 2.6. The following conclusions are drawn:

(1) The three criteria yield fracture initiation angles with the same trend over the region (0°-90°), but vastly different magnitudes in the middle region (10° - 80°). The ranking of the magnitude of fracture initiation angle by the three criteria is: S-Criterion < σ_θ-criterion < G-criterion.

(2) Fracture initiation angles by the three criteria match very well when inclination angles are in the regions of 0° - 10° and 10° - 90°. This means that there is no difference in the predicted fracture path and any of the three criteria can be used as the angle between the orientation of preexisting fracture and the horizontal principal stress is small (e.g., 0° - 10°).

(3) Fracture initiation angle varies rapidly with inclination angle between 0°-10°, and 10°-90° because *SIF* ratio varies significantly in these regions (Fig. 2.5). This means fracture initiation angle is very sensitive to inclination angle when the angle between the orientation of preexisting fracture and minimum horizontal principal

stress is small (0°-10°). Therefore, a small deviation from minimum horizontal in-situ principal stress direction during the horizontal well drilling, or a small deviation from maximum horizontal in-situ principal stress in the perforation of vertical well, might lead to significant fracture twist near the wellbore in hydraulic fractures.

(4) Fracture initiation angle varies gradually between 10° and 80° because *SIF* ratio does not vary significantly in the region (as shown in Fig. 2.5), which means fracture initiation angle is insensitive to inclination angle when inclination angle is between 10° and 80°.

(5) The selection of a proper fracture initiation and propagation criterion for hydraulic fracturing design requires experimental verification, discussed under Experimental Verification.

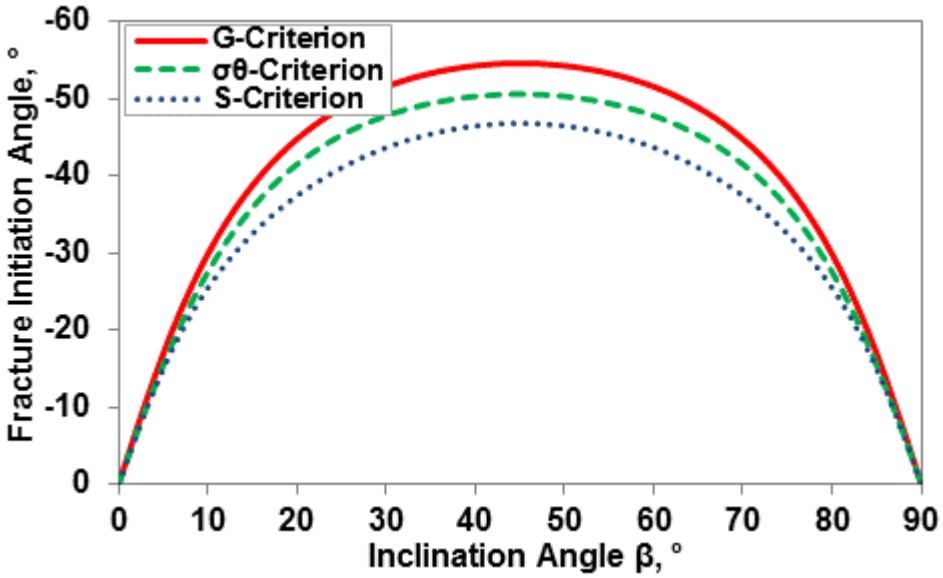

Figure 2.6 Initiation angle vs. inclination angle for three different criteria.

2.4 Factors Influencing Fracture Initiation Angle

After examining the fracture initiation angles derived from the three criteria, it is observed that the initiation angle is affected by the following factors: (1) difference

between horizontal in-situ principal stresses, (2) breakdown pressure, (3) fracture toughness, and (4) Poisson's ratio (only applies to S-Criterion). Because the initiation angle exhibits similar trends for the three criteria (Fig. 2.6), we examine the sensitivity of fracture initiation angle to these factors with only the S-criterion.

2.4.1 Stress Anisotropy Influence on Fracture Initiation Angle

For complex geological structure or lithology where stress anisotropy is significant, mode-II *SIF* increases and near wellbore fracture tortuosity becomes more significant. The stress anisotropy can be expressed by either the ratio of two principal horizontal stresses (e.g., $b = \sigma_H/\sigma_h$), or the contrast between two principal horizontal stresses (e.g., $C = \sigma_H - \sigma_h$). Based on the laboratory experiments, it was observed that fracture propagation orientation is contingent upon principal stress difference. It is more convenient to study stress anisotropy by using stress contrast rather than stress ratio. For example, consider two cases, Case I: σ_H = 21 MPa, σ_h = 20 MPa, C = 1 MPa, b = 1.05; and Case II: σ_H = 22.5 MPa, σ_h = 20 MPa, C = 2.5 MPa, b = 1.125. It is easier to show stress anisotropy for both cases by using stress contrast than using stress ratio. The influence of stress anisotropy on fracture initiation angle under four stress contrasts are studied with the basic parameters in Table 2.1. Keeping σ_h = 15 MPa, values of C = 1, 5, 10, 15 MPa are set, which correspond to σ_H = 16, 20, 25, and 30 MPa, respectively. Fracture toughness is assumed to be constant. The results are presented in Fig. 2.7, and discussed below:

(1) For a given inclination angle, the fracture initiation angle increases with increasing stress anisotropy because mode-II *SIF* increases, which means sliding mode

becomes dominant. In practice, it means that the fracture will twist more in the region of higher stress anisotropy.

(2) Fracture initiation angle is more sensitive to small stress contrast. For example, when *C* increases from 1 MPa to 5 MPa, fracture initiation angle increases by about 300%; however, fracture initiation angle increases by less than 15% when *C* increases from 10 MPa to 15 MPa. This suggests it is important to improve the accuracy of stress contrast determination. Small error in the calculation of stress contrast will magnify the error in the prediction of fracture propagation path in regions of small stress contrast.

(3) For the formation with high stress anisotropy, in order to mitigate fracture twist near wellbore, it is recommended to decrease the inclination angle by controlling the wellbore azimuth and/or perforation phasing. Although higher inclination angle produces lower initiation angle, higher breakdown pressure is required at higher inclination angle, as is shown in Fig. 2.8, and fracture will turn slowly towards the plane perpendicular to minimum horizontal stress.

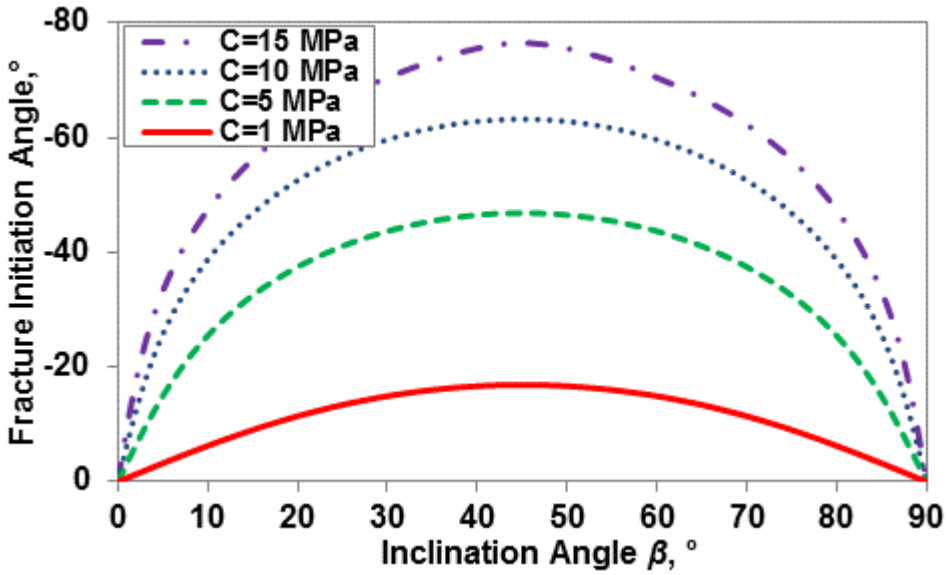

Figure 2.7 Initiation angle vs. Inclination angle at different stress contrast.

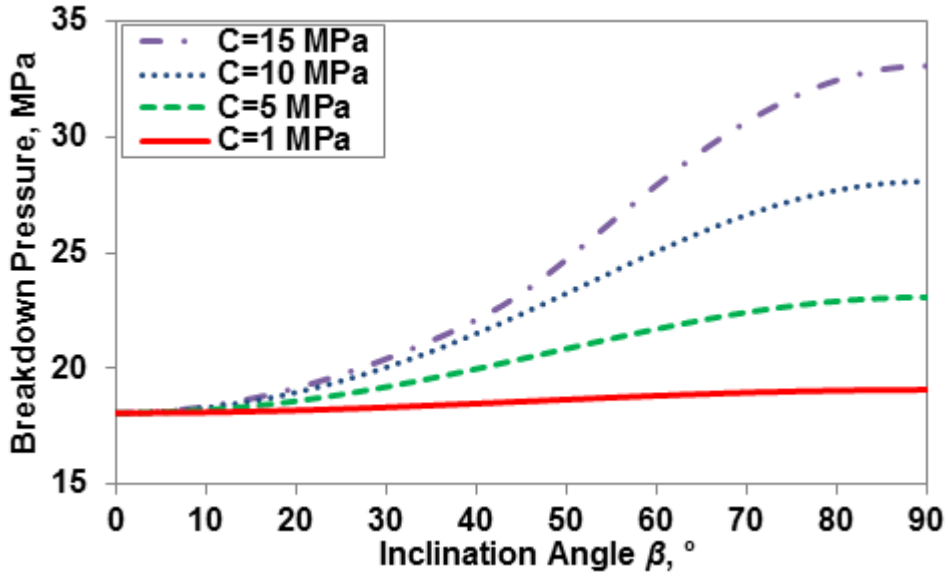

Figure 2.8 Breakdown pressure vs. Inclination angle at different stress contrasts.

2.4.2 Breakdown Pressure/Fracture Toughness Influence on Fracture Initiation Angle

The breakdown pressure of mixed-mode fracture propagation is determined by both K_{IC} and K_{IIC}, as expressed by Eq. 10. Therefore, only the sensitivity of fracture initiation angle to fracture toughness is analyzed.

Varying K_{IIC} in Table 2.1 and keeping other parameters constant, the sensitivity of fracture initiation angle and breakdown pressure to K_{IIC} is examined. Figures 2.9 and 2.10 indicate that both breakdown pressure and fracture initiation angle are not sensitive to K_{IIC}. As a result, only the influence of K_{IC} on fracture initiation angle is studied for K_{IC} = 2.0, 2.5, and 3.0 MPa·m$^{0.5}$. The results of fracture initiation angle versus inclination angle are shown in Fig. 2.11**,** and the analysis is presented in the following.

(1) For a given inclination angle, higher the K_{IC}, lower is the fracture initiation angle. This is because increasing fracture toughness will require higher breakdown pressure to create new fracture surface, as is shown in Fig. 2.12. Increasing breakdown pressure will increase K_I, while K_{II} is constant, then *SIF* ratio will increase (mode-I *SIF* becomes dominant). Finally fracture initiation angle will decrease, as is depicted in Fig. 2.4.

(2) One important application of this result is in explaining different fracture initiation angles and breakdown pressures during multi-stage fracturing of a horizontal well. The fracture toughness at various stages might be different due to formation heterogeneity. For example, at stage 1, K_{IC} = 3.0 MPa·m$^{0.5}$; at stage 2, K_{IC} = 2.0 MPa·m$^{0.5}$, the breakdown pressure at stage 1 is higher than stage 2. Fracture twist is less near borehole at stage 1 than at stage 2. This means the risk of premature

screenout and pressure drawdown near borehole for stage 1 is less than for stage 2. As a result, near wellbore fracture geometry along the same borehole might be different.

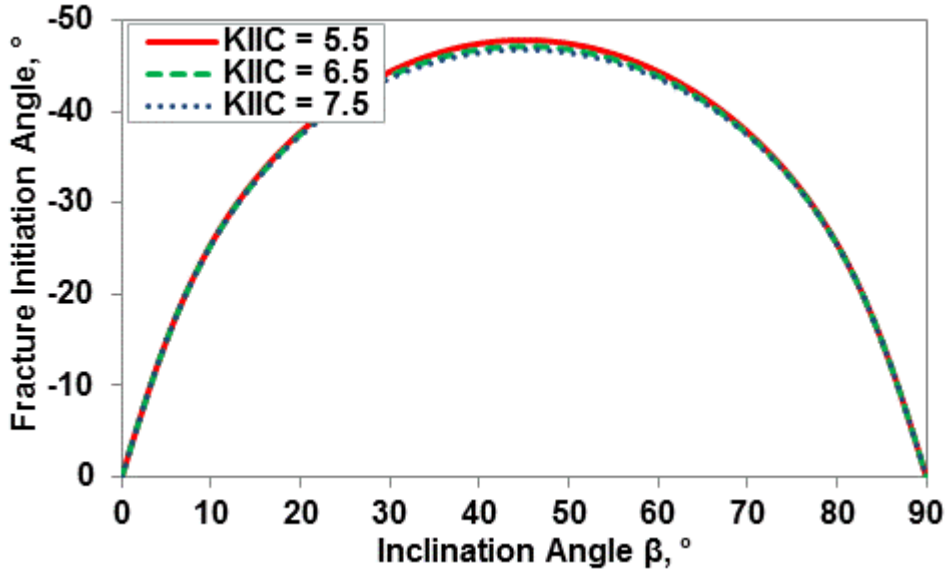

Figure 2.9 Mode II fracture toughness influence on fracture initiation angle.

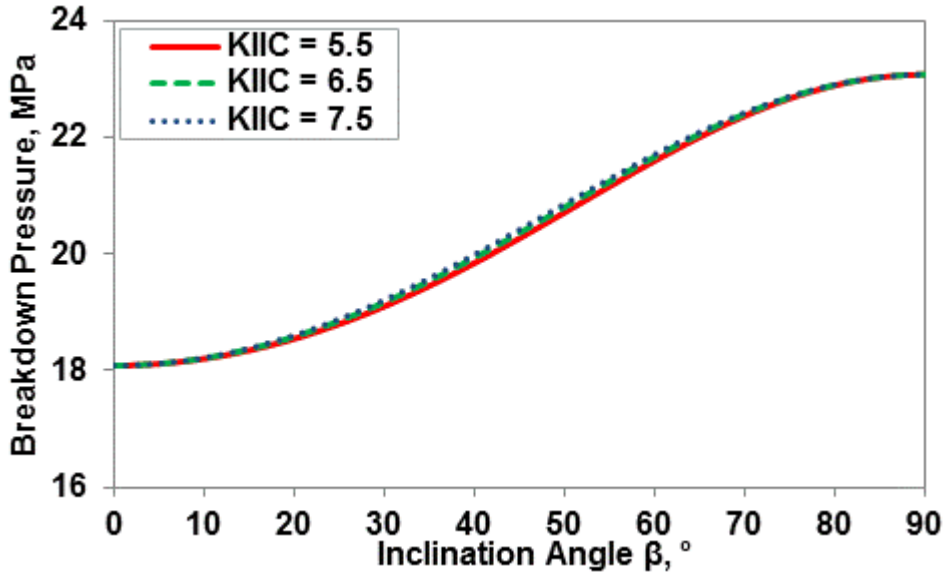

Figure 2.10 Mode II fracture toughness influence on breakdown pressure.

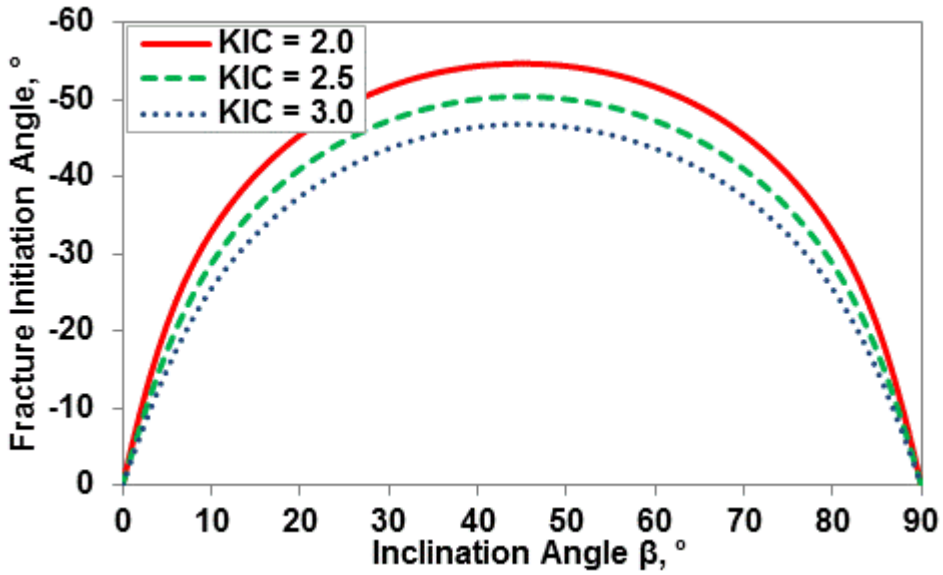

Figure 2.11 Mode I fracture toughness influence on fracture initiation angle.

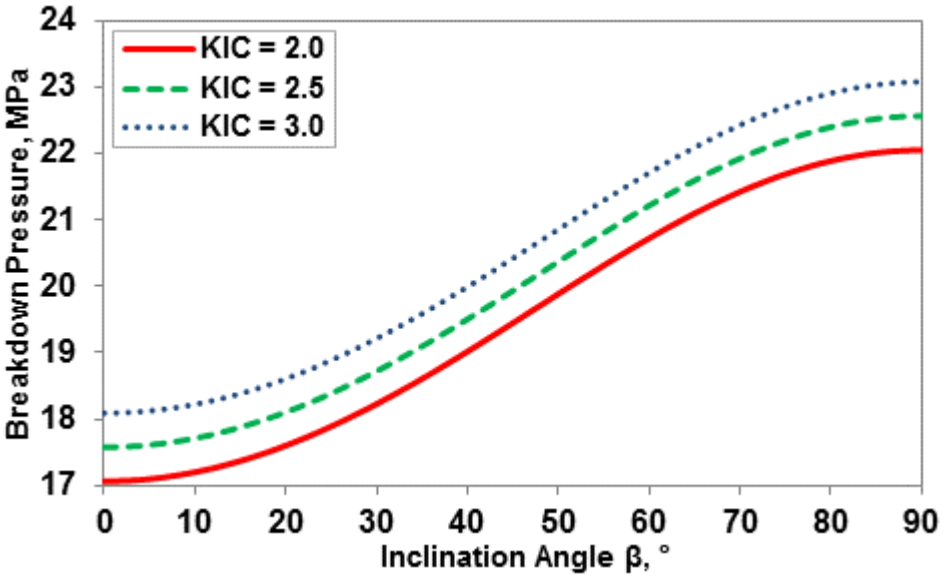

Figure 2.12 Mode I fracture toughness influence on breakdown pressure.

2.4.3 Poisson's Ratio Influence on Fracture Initiation Angle (S-criterion)

Among the three criteria, only S-Criterion depends on Poisson's ratio. To evaluate the influence of Poisson's ratio on fracture initiation angle, all other parameters in Table 2.1 are kept constant. Three values of Poisson's ratio are selected to investigate

its influence on the initiation angle. The Poisson's ratio values of 0.15, 0.25, and 0.35, which corresponds to k = 2.4, 2.0, and 1.6 (recall that k = 3 - 4v, v is Poisson's ratio), are used.

The results shown in Fig. 2.13 are summarized in the following:

(1) Generally, fracture initiation angle for different Poisson's ratio shows similar trend for the complete region (0°-90°) but different magnitudes in the region between 10° - 80°.

(2) Higher the Poisson's ratio, higher is the fracture initiation angle.

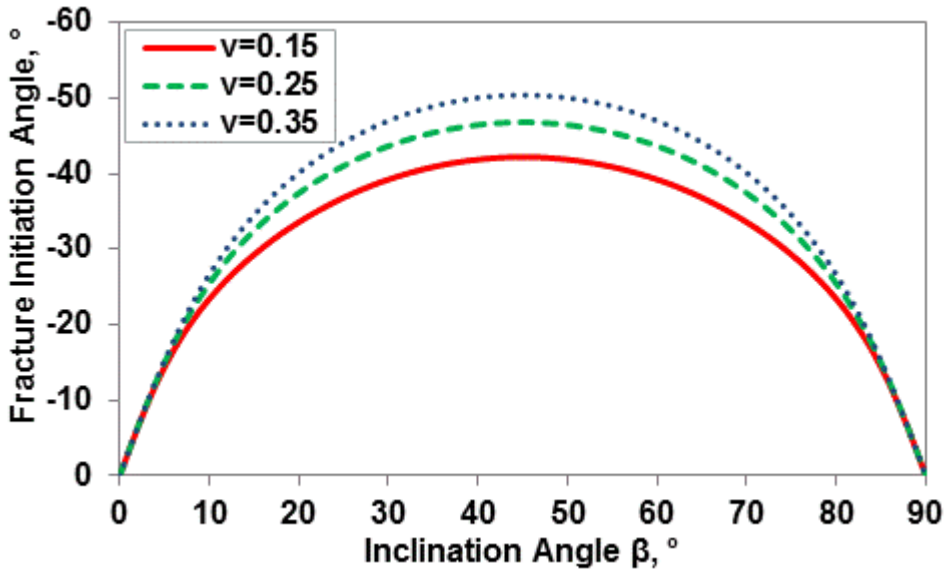

Figure 2.13 Poisson's ratio influence on fracture initiation angle.

2.5 Experimental Verification[2]

Scaling laws have been developed to minimize the effect of boundary on fracture propagation for hydraulic fracturing experiments [*De Pater et al.*, 1994;

[2] Hydraulic fracturing experiments were conducted by Prof. Mian Chen's research group in Rock Mechanics Laboratory at China University of Petroleum (Beijing).

Berchenko et al., 2004]. The experimental samples are made of cement and quartz sand at the volume ratio of 1:1. The brand of cement is PC 32.5[3]. The quartz sand is well screened fine river sand. After mixing quartz sand and cement, measure the mixture's total volume. Pure water is added to the mixture of quartz sand and cement at the volume ratio of 0.4 (one volume water, 0.4 volume mixture). The fracturing fluid is made of guar, and its viscosity is 124 cp at 1022 sec^{-1}. The purpose of using high viscous fracturing fluid is to create relatively smooth planar fracture surface and reduce fluid loss. The flow rate of fracturing fluid is controlled at 2.05×10^{-9} m^3/sec. A triaxial hydraulic fracturing system is used to simulate the hydraulic fracturing process in the laboratory (Fig. 2.14). The system can produce three unequal stresses (one overburden stress and two horizontal stresses). The maximum loading is 28 MPa. The maximum injection pressure is 140 MPa. The perforation is simulated by using small cylinder made of stiff paper, as shown in Fig. 2.15-A. The size limitation of the sample restricts the depth of penetration. The workflow of experimental procedure is summarized by 9 photos in Fig. 2.15. The properties and dimensions of experimental samples are listed in Tables 2.2 and 2.3. As discussed in Section 2.2.1, the stress concentration near borehole can be neglected because the penetration depth is about four times the borehole radius, and the borehole wall is made of steel in laboratory.

[3] "PC" is the symbol for Portland cement, "32.5" is the minimum desired tensile strength value (in the unit of MPa) achieved within 28 days.

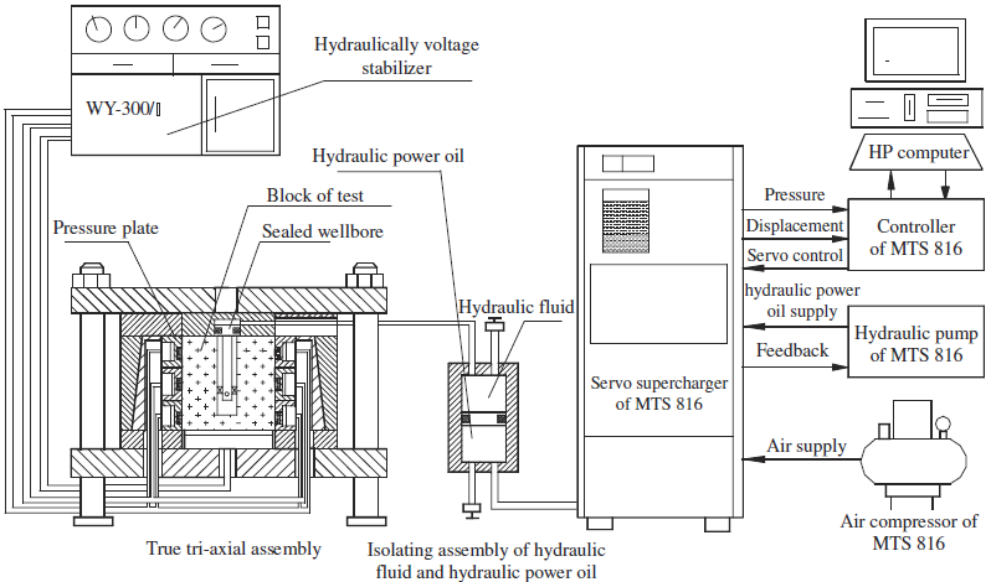

Figure 2.14 Schematic of triaxial hydraulic fracturing test system.

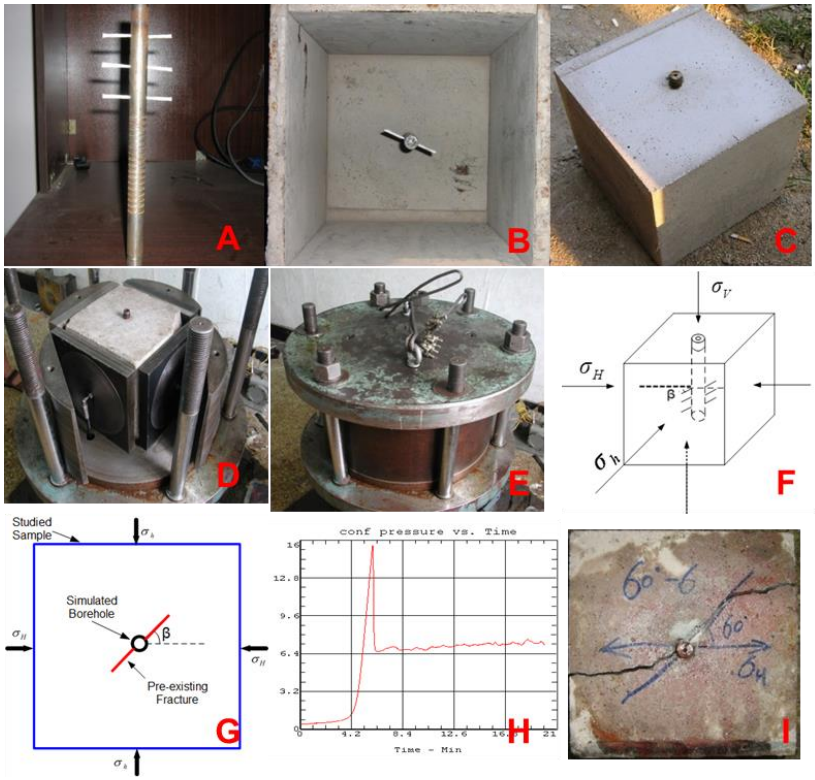

Figure 2.15 Experimental sample preparation and setup procedures.

(A) Simulated borehole with perforations. Borehole is made of steel tube, perforation is made of stiff paper

(B) Mold of experimental sample. Make samples with different inclination angle by rotating borehole

(C) Cubic sample for hydraulic fracturing test

(D) Sample loading into the cell

(E) Completed assembly

(F) 3-D view of loadings

(G) 2-D top view of loadings

(H) Pressure recording from MTS computer system

(I) Fractured sample

A series of experiments have been conducted for the study of fracture propagation under the far field stress $\sigma_h < \sigma_H < \sigma_v$. When the orientation of preexisting fracture is perpendicular to the plane of minimum horizontal stress, the experimental results show that the initiation angle is zero, and fracture propagates perpendicular to the direction of minimum horizontal principal stress, as is shown in Fig. 2.16. It is also observed that vertical fracture plane is relatively smooth because the overburden stress is the maximum and far greater than the horizontal stresses, and fluid viscosity is high.



Figure 2.16 Non-twisted fracture propagation when preexisting fracture aligns with fracture orientation.

Table 2.2 Properties of experimental samples

Parameter	**Value**
Young's modulus	15 *GPa*
Poisson's ratio	0.23
UCS	48.5 *MPa*
Permeability	0.5 md
Porosity	1.85%

Table 2.3 Configurations of experimental samples

Parameter	**Value**
Block Side Length: *L*	30 cm
Borehole Inner Diameter: *ID*	15 mm
Borehole Outer Diameter: *OD*	20 mm
Preexisting Fracture Length: *a*	30 mm
Simulated Perforation Diameter	2 mm
Preexisting Fracture Phasing	180°

The measurement of fracture initiation angle at the tip of preexisting fracture is demonstrated by taking sample "1-6-60" (represents "σ_h-σ_H-β", 1 and 6 are minimum and maximum horizontal principle stresses in the unit of MPa, 60 is inclination angle °) as an example (Fig. 2.17). The left photo in Fig. 2.17 shows that fracture turns in horizontal plane, and the right photo in Fig. 2.17 shows vertical planar fracture surface.

One must be aware that not all experiments can fulfill experimental purpose. For instance, when the inclination angle is small (e.g., less than 10°), fracture initiation angle is small. Then it is difficult to measure small fracture initiation angle on fractured samples. Thus, the minimum inclination angle in the experiment is set as 15°. Even so, some experiments still failed due to the complexities in conducting hydraulic fracturing experiments [*Haimson*, 1981]. For example, experiment shown in Fig. 2.18-A-1 failed because there are two peaks of breakdown pressure in its pressure vs. time curve (Fig. 2.18-A-2). This failure might be caused by nonhomogeneous rock property when preparing samples. Although peak pressure in Fig. 2.18-B-2 is clear, two-wing fracture is not created, fracture initiation angle is not clear either. Thus, sample shown in Fig. 2.18-B-1 cannot be considered as qualified sample. The failure in Fig. 2.18-B-1 might be attributed to low cementing strength between borehole wall (steel tube surface) and sample. Similar failures as Fig. 2.18 are also observed in other unsuccessful experiments.

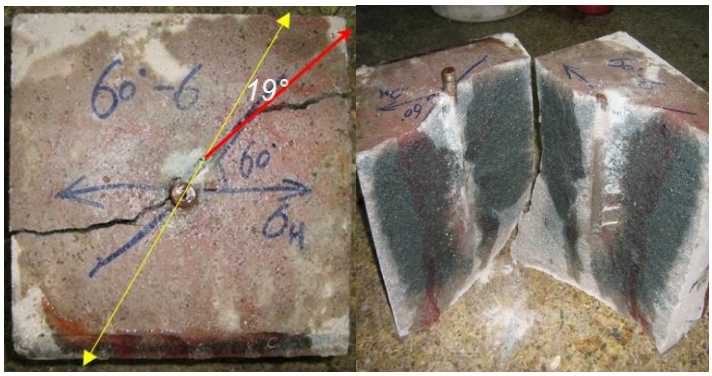

Figure 2.17 Measurement of fracture propagation angle.

The yellow double-arrow line represents the orientation of preexisting fractures, the red single-arrow line represents fracture propagation orientation at the tip of preexisting fracture.

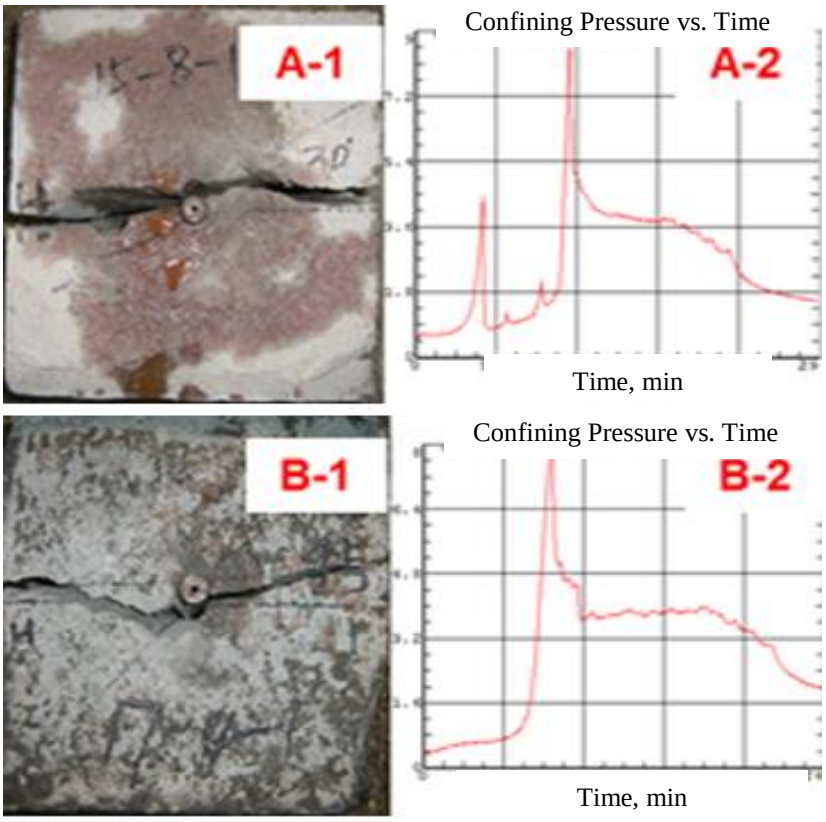

Figure 2.18 Examples of failed experiment.

Therefore, in order to determine which criterion simulates hydraulic fracture propagation better, 8 successful experiments (two different stress contrasts and four different inclination angles, see Table 2.4) are selected from 40 experiments to fulfill the objective. The inclination angle β is known when preparing experimental samples, the horizontal stresses σ_h and σ_H, and breakdown pressure P_b are experimentally determined and stored in computer. The experimental conditions and breakdown pressures are listed in Table 2.4. The fracture toughness data of experimental samples is not required when calculating theoretical initiation angle because breakdown pressure can be read directly, and not required to be calculated with Eq. 2.10. The skip of breakdown pressure calculation helps improve the accuracy of experimental verification because K_{IC} and K_{IIC} at laboratory conditions changes [*Zhao and Roegiers*, 1993], and cannot be measured during hydraulic fracturing experiments.

Table 2.4 Experimental conditions and breakdown pressures

Number**	**Minimum Horizontal Stress** σ_h (*MPa*)	**Maximum Horizontal Stress** σ_H (*MPa*)	**Inclination Angle** β °	**Breakdown Pressure** P_b (*MPa*)
1-4-15	1	4	15	7.4
1-4-30	1	4	30	8.5
1-4-45	1	4	45	9.3
1-4-60	1	4	60	9.8
1-6-15	1	6	15	6.23
1-6-30	1	6	30	10.4
1-6-45	1	6	45	10.5
1-6-60	1	6	60	15.6

The overburden stress is kept constant, $\sigma_v = 15\ MPa$. Higher overburden stress is applied to constrain deformation in vertical direction. The naming rule is σ_h-σ_H-β, which are “min horizontal stress - max horizontal stress - inclination angle”.

Table 2.5 Theoretical and experimental fracture initiation angles

Number	**Theoretical Fracture Initiation Angle**, °			**Experimental** Fracture Initiation Angle, °
	G-Criterion	σθ-Criterion	S-Criterion	
1-4-15	-14.7	-13.4	-13.0	-12.0
1-4-30	-22.3	-20.4	-19.2	-19.5
1-4-45	-24.9	-22.9	-21.3	-20.0
1-4-60	-22.8	-20.9	-19.7	-19.8
1-6-15	-28.0	-25.8	-23.7	-22.0
1-6-30	-28.8	-26.6	-24.4	-25.0
1-6-45	-35.5	-32.9	-29.5	-28.0
1-6-60	-23.0	-21.0	-19.8	-19.0

The steps of experimental verification are as follows:

1. Calculate theoretical fracture initiation angle by the three propagation criteria with the parameters in Table 2.4.
2. Measure fracture initiation angle of the preexisting fractures with the method shown in Fig. 2.17 for the eight qualified samples. The fracture initiation angles are recorded in Table 2.5.
3. Analyze both the theoretical and experimental fracture initiation angles in Figs. 2.19 and 2.20 (the source data is Table 2.5).

From Figs. 2.19 and 2.20, it can be concluded that fracture initiation angles by S-Criterion match experimental results the best, and fracture initiation angles by G-Criterion deviate the most from measured results. However, S-criterion has not been implemented in numerical simulation of fracture propagation as extensively as σ_θ-Criterion because analytical solution of fracture initiation angle by σ_θ-Criterion is easy to be calculated, and σ_θ-Criterion is easy to be embedded in fracturing model. In order to better capture the path of fracture initiation in hydraulic fracturing, it is suggested

that S-Criterion is better than both σ_θ-Criterion and G-Criterion. Data in Table 2.4 suggests that increasing inclination angle will increase breakdown pressure, which supports the trend of theoretical results shown in Figs. 2.8, 2.10 and 2.12. Table 2.5 suggests that increasing stress contrast will increase fracture initiation angle, which supports theoretical results shown in shown in Fig. 2.7.

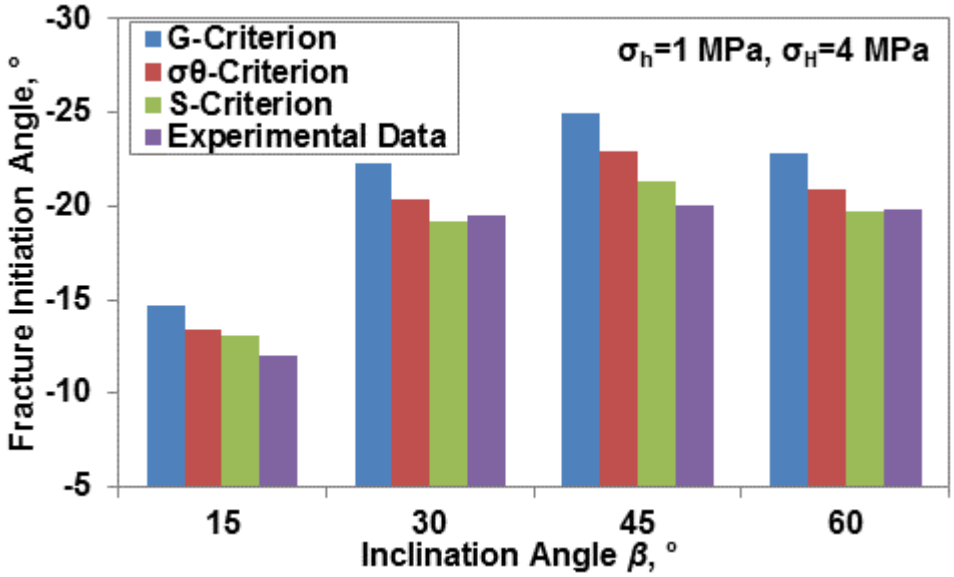

Figure 2.19 Comparison between theoretical and experimental fracture initiation angles (stress contrast = 3 MPa).

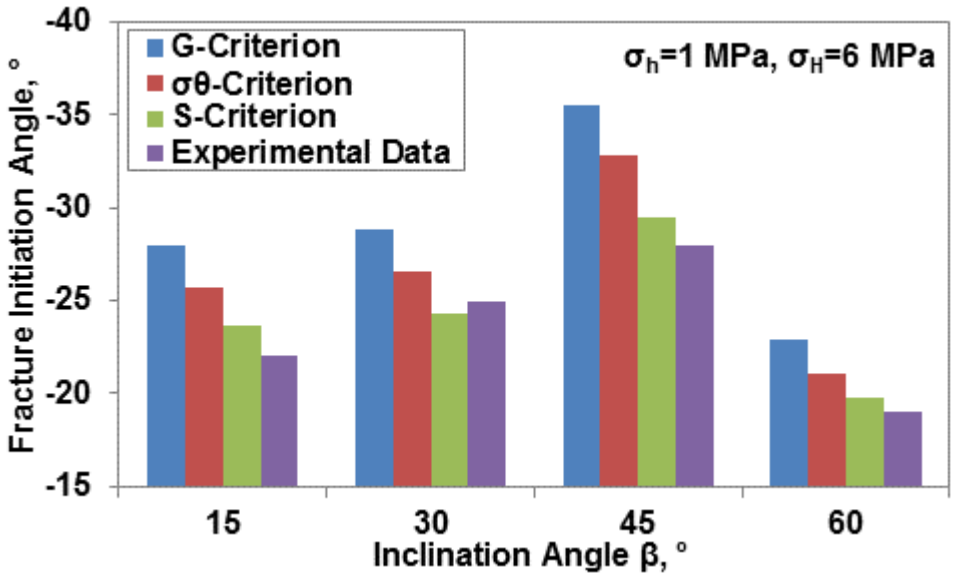

Figure 2.20 Comparison between theoretical and experimental fracture initiation angles (stress contrast = 5 MPa).

2.6 Discussion and Conclusions

A detailed analysis of mixed-mode fracture initiation angle in hydraulic fracturing is presented in this study. Measured data from hydraulic fracturing experiments have been applied to verify which propagation criterion is better. Guidelines for the optimization of hydraulic fracturing of both vertical and horizontal wells are suggested. The conclusions are drawn as follows:

1. Simulation with S-Criterion yields fracture initiation angles the closest to the experimental results, followed by σ_θ-Criterion, and G-Criterion.
2. Under the same simulation conditions, the three criteria produce fracture initiation angle with similar trend but different magnitudes: S-Criterion < σ_θ-Criterion < G-Criterion.

3. The relationship between fracture initiation angle and inclination angle is a bell-shaped curve. Fracture initiation angle varies significantly when inclination angle is in the region between 0° to 10°, and 10° to 90°.
4. Stress contrast between σ_H and σ_h, mode-I fracture toughness, and Poisson's ratio are considered as major uncontrollable factors influencing fracture initiation in hydraulic fracturing. Higher stress contrast and Poisson's ratio will increase fracture initiation angle, while higher mode-I fracture toughness will decrease fracture initiation angle. Experimental results have also proven that fracture initiation angle increases with increasing stress contrast.
5. Both theoretical and experimental results have shown that breakdown pressure increases with increasing inclination angle.
6. Hydraulic fracturing in the area with high stress anisotropy, high Poisson's ratio, or low fracture toughness will face relatively high risk of fracture twisting, premature screenout, and high pressure drop near the wellbore. The possible solutions are: reduction in inclination angle by maintaining horizontal well orientation close to the minimum in-situ principal stress direction, or perforating close to maximum horizontal in-situ principal stress direction for vertical well, or fracturing in the interval with relatively high fracture toughness. It is thus imperative to acquire an accurate in-situ principal stress orientation for hydraulic fracturing.
7. Theoretical and experimental attempts have been made for evaluating fracture initiation criteria and factors influencing fracture twist. However, further research and experimental data are needed to validate the results.

The present study does not cover fracture initiation angle in nonhomogeneous and anisotropic formations, where stress distribution near the crack tip should be recalculated. It is more difficult to calculate fracture initiation angle for mixed mode fracture propagation in nonhomogeneous formation. Stress concentration near the borehole is ignored, and pressure distribution inside fracture is assumed constant in present calculation of *SIF*. In chapter 3, a weight function method will be developed for calculating *SIF*. The weight function method can accounts for stress concentration near wellbore, nonlinear stress on fracture surface, and inclination angle.

Chapter 3. Weight Function and Stress Intensity factor for Symmetrical Radial Cracks Emanating from Borehole

3.1 Introduction

Symmetrical radial cracks emanating from borehole are common in oriented perforation and hydraulic fracturing (Fig.3.1).

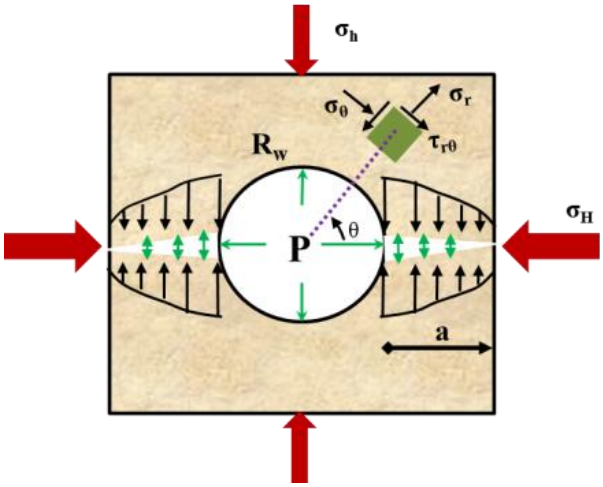

Figure 3.1 Stress distributions on radial cracks emanating from borehole.

Pressure inside borehole is fracturing pressure P, while inside fracture it is less or equal to P. σ_h and σ_H are two far field stresses. The black arrows represent non-uniform normal stress on crack faces. θ is the angle with reference to horizontal principal stress, counterclockwise direction is positive.

The determination of maximum in-situ stress, prediction of breakdown pressure, and simulation of fracture propagation path near the wellbore are contingent on the accurate calculation of *SIF* [*Barry, Whittaker and Singh*, 1992]. Inaccurate estimation of in-situ stress contrast may lead to unexpected wellbore instability, premature screenout, and sand production [*Fjar et al.*, 2008]. Overestimation of breakdown pressure may lead to drilling induced fracture [*Bourgoyne Jr et al.*, 1986]. Therefore, having a

reliable method for the calculation of *SIF* of radial cracks emanating from borehole is significant in petroleum geomechanics. Although *J*-integral method is good and has been applied extensively in fracture mechanics [*Rice*, 1968b; a], it is not convenient for field application because of complex numerical integral. *SIF* derived from tabulated data is applied to calculate maximum in-situ stress from the data of mini-frac test [*Abou-Sayed, Brechtel and Clifton*, 1978], but with limitations. They are: (1) only applicable for specific geometry in the reference [*Paris and Sih*, 1965]; and (2) not appropriate for the case of nonlinear stress on fracture face. Boundary collocation method is also applied to calculate *SIFs* for the fractures shown in Fig. 3.2 [*Newman Jr*, 1971; *Tada et al.*, 2000], but the solutions are: (1) only applicable for cracks aligning with maximum in-situ stress orientation; and (2) not suitable for the case with nonlinear stresses acting on fracture faces. However, *SIFs* for fractures in Fig. 3.2 can be taken as reference *SIFs* to solve weight function parameters.

To overcome the limitations discussed above, weight function method is developed to calculate *SIFs* in fracture mechanics [*Glinka and Shen*, 1991; *Shen and Glinka*, 1991; *Zheng and Glinka*, 1995; *Zheng, Kiciak and Glinka*, 1997; *Kiciak, Glinka and Burns*, 2003]. The weight function is only dependent on fracture geometry, and is a characteristic property for a particular geometry [*Bueckner*, 1970; *Rice*, 1972]. It is widely applied because it simplifies the calculation of *SIFs* under complex loading conditions to an integration expression as follows:

$$K_i = \int_0^a \sigma_i(x,\theta) m(x,a) dx \tag{3.1}$$

$$m(x,a) = \frac{2}{\sqrt{2\pi(a-x)}}\left[1 + M_1\left(1-\frac{x}{a}\right)^{1/2} + M_2\left(1-\frac{x}{a}\right) + M_3\left(1-\frac{x}{a}\right)^{3/2}\right] \tag{3.2}$$

where, i =1, 2, 3; $\sigma_i(x,\theta)$ is stress field resulting from the loadings applied on the uncracked body, normal to the faces of prospective crack. x is dummy variable; θ is the angle with reference to horizontal principal stress, clockwise direction is negative; M_1, M_2, and M_3 are weight function parameters. Here, compression is taken as negative, and tension as positive.

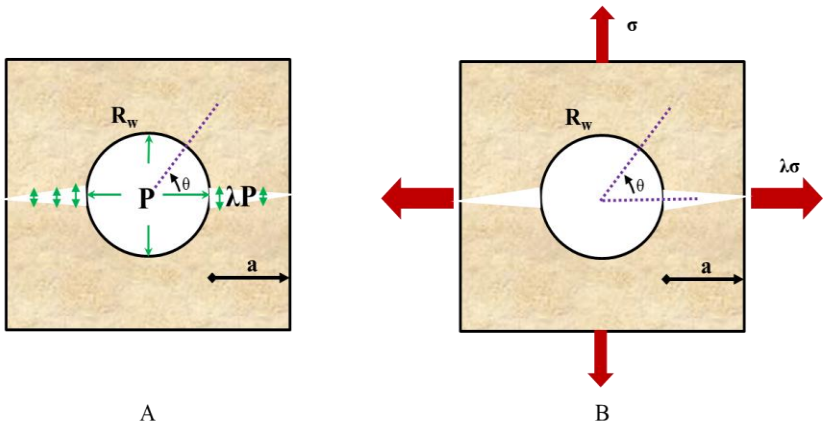

Figure 3.2 Cracks emanating from borehole under different loadings.

λ is a positive constant, $0 \leq \lambda \leq 1$; R_w is borehole radius, σ is applied stress.

Fig. 3.2-A has only pressure inside borehole and fracture. Fig. 3.2-B has only external tension loadings. The symmetrical fractures align with direction of principal stress.

Although weight functions have been developed for numerous geometries [*Glinka*, 1996], the one for symmetrical radial cracks emanating from borehole in an infinite plane is not available. Considering its importance in petroleum/geothermal engineering as described earlier, the weight function parameters for this case is derived with the available data [*Newman Jr*, 1971; *Tada et al.*, 2000]. The accuracy of the weight function based *SIFs* is validated against boundary collocation based *SIFs* under two different loading conditions shown in Fig. 3.2.

3.2 Determination of weight function parameters for symmetrical radial cracks

The method of two reference stress intensity factors is selected in the determination of weight function parameters because of its high accuracy [*Shen and Glinka*, 1991]. Three independent equations can be written as follows:

$$K_1 = \int_0^a \sigma_1(x) \frac{2}{\sqrt{2\pi(a-x)}} \left[1 + M_1 \left(1 - \frac{x}{a}\right)^{1/2} + M_2 \left(1 - \frac{x}{a}\right) + M_3 \left(1 - \frac{x}{a}\right)^{3/2} \right] dx \tag{3.3}$$

$$K_2 = \int_0^a \sigma_2(x) \frac{2}{\sqrt{2\pi(a-x)}} \left[1 + M_1 \left(1 - \frac{x}{a}\right)^{1/2} + M_2 \left(1 - \frac{x}{a}\right) + M_3 \left(1 - \frac{x}{a}\right)^{3/2} \right] dx \tag{3.4}$$

$$\frac{\partial}{\partial x} \left\{ \frac{2}{\sqrt{2\pi(a-x)}} \left[1 + M_1 \left(1 - \frac{x}{a}\right)^{1/2} + M_2 \left(1 - \frac{x}{a}\right) + M_3 \left(1 - \frac{x}{a}\right)^{3/2} \right] \right\} \Bigg|_{x=0} = 0 \tag{3.5}$$

where, K_1 and K_2 are reference *SIFs* corresponding to reference stresses $\sigma_1(x)$ and $\sigma_2(x)$, respectively. The reference stresses and *SIFs* are available [*Tada et al.*, 2000], or can be solved with numerical methods. Equation 3.5 is based on the characteristic of crack surface curvature at the crack mouth [*Shen and Glinka*, 1991].

SIFs for situations shown in Fig. 3.2 are derived with boundary collocation methods [*Newman Jr*, 1971]. Stress fields for uncracked body under the same loading shown in Fig. 3.2 are classical Kirsch solutions [*Fjar et al.*, 2008]. Kirsch solution of Fig. 3.2-B is more complex than that of Fig. 3.2-A. In order to simplify the derivation of weight function parameters, boundary collocation based *SIFs* of Fig. 3.2-A and its Kirsch solutions are adopted. The general expression of mode-I *SIF* for Fig. 3.2-A is [*Newman Jr*, 1971; *Tada et al.*, 2000],

$$K_I = P\sqrt{\pi a}\left\{\begin{array}{l}(1-\lambda)\left(1-\dfrac{a}{R_w+a}\right)\left[0.637+0.485\left(1-\dfrac{a}{R_w+a}\right)^2+0.4\left(\dfrac{a}{R_w+a}\right)^2\left(1-\dfrac{a}{R_w+a}\right)\right] \\ +\lambda\left\{1+\left(1-\dfrac{a}{R_w+a}\right)\left[0.5+0.743\left(1-\dfrac{a}{R_w+a}\right)^2\right]\right\}\end{array}\right\},$$

$$(0 \le \lambda \le 1.0) \tag{3.6}$$

Two reference *SIFs* for two applied stresses are required to solve the weight function parameters.

- $\lambda = 0$, only pressure inside hole,

$$\sigma_1(x) = P\left(\frac{R_w}{R_w+x}\right)^2,\ (0 \le x \le a) \tag{3.7}$$

$$K_1 = P\sqrt{\pi a}\left(1-\frac{a}{R_w+a}\right)\left[0.637+0.485\left(1-\frac{a}{R_w+a}\right)^2+0.4\left(\frac{a}{R_w+a}\right)^2\left(1-\frac{a}{R_w+a}\right)\right] \tag{3.8}$$

- $\lambda = 1$, the same pressure inside both the hole and fracture,

$$\sigma_2(x) = P\left(\frac{R_w}{R_w+x}\right)^2 + P,\ (0 \le x \le a) \tag{3.9}$$

$$K_2 = P\sqrt{\pi a}\left\{1+\left(1-\frac{a}{R_w+a}\right)\left[0.5+0.743\left(1-\frac{a}{R_w+a}\right)^2\right]\right\} \tag{3.10}$$

Substituting Eqs. 3.7 and 3.8 into Eq. 3.3 and after manipulation, Eq. 3.11 is obtained as follows:

$$\begin{array}{l}\sqrt{\pi a}\left(1-\dfrac{a}{R_w+a}\right)\left[0.637+0.485\left(1-\dfrac{a}{R_w+a}\right)^2+0.4\left(\dfrac{a}{R_w+a}\right)^2\left(1-\dfrac{a}{R_w+a}\right)\right]= \\ \displaystyle\int_0^a\left(\frac{R_w}{R_w+x}\right)^2\frac{2}{\sqrt{2\pi(a-x)}}\left[1+M_1\left(1-\frac{x}{a}\right)^{1/2}+M_2\left(1-\frac{x}{a}\right)+M_3\left(1-\frac{x}{a}\right)^{3/2}\right]dx\end{array} \tag{3.11}$$

Substituting Eqs. 3.9 and 3.10 into Eq. 3.4 and after manipulations, Eq. 3.12 is obtained as follows:

$$\sqrt{\pi a}\left\{1+\left(1-\frac{a}{R_w+a}\right)\left[0.5+0.743\left(1-\frac{a}{R_w+a}\right)^2\right]\right\}= \int_0^a\left[\left(\frac{R_w}{R_w+x}\right)^2+1\right]\frac{2}{\sqrt{2\pi(a-x)}}\left[1+M_1\left(1-\frac{x}{a}\right)^{1/2}+M_2\left(1-\frac{x}{a}\right)+M_3\left(1-\frac{x}{a}\right)^{3/2}\right]dx \quad (3.12)$$

The relationship between M_2 and M_3 is obtained by solving Eq. 3.5,

$$1-M_2-2M_3=0 \quad (3.13)$$

Three independent equations (Eqs. 3.11 through 3.13) with three unknown variables (M_1, M_2, and M_3) are available now. M_1, M_2, and M_3 are functions of crack length a and borehole radius R_w, which are $M_1(R_w,a), M_2(R_w,a)$ and $M_3(R_w,a)$. It is not feasible to solve M_1, M_2, and M_3 manually because the stress field is nonlinear. M_1, M_2, and M_3 are solved numerically with the Mathematica code presented in Appendix E. The full expressions of $M_1(R_w,a)$, $M_2(R_w,a)$ and $M_3(R_w,a)$ are not listed here due to their complexity. Interested readers can solve them with the code in Appendix E. For convenience, values of M_1, M_2, and M_3 at different a/R_w are listed in Table F-1 of Appendix F. In addition, three correlations of weight function parameters derived with the values in Appendix F are listed below:

$$M_1=0.0356x^5-0.0977x^4-0.1678x^3+0.4661x^2+0.0883x-0.2673 \quad R^2=0.9923 \quad (3.14)$$

$$M_2=-0.0472x^5+0.0735x^4+0.2198x^3-0.3205x^2-0.2037x+0.1535 \quad R^2=0.9959 \quad (3.15)$$

$$M_3=-0.0236x^5+0.0368x^4+0.1099x^3-0.1603x^2-0.1018x+0.5768 \quad R^2=0.9959 \quad (3.16)$$

where, $x = Log_{10}(a/R_w)$, $0.001 \leq a/R_w \leq 100$. The range of a/R_w covers the length of both natural and induced fractures.

3.3 Validation

3.3.1 Validation for Fig. 3.2-A

Weight function based *SIFs* for symmetrical radial cracks emanating from circular hole are verified with the available boundary collocation based *SIFs* for Fig. 3.2-A [*Newman Jr*, 1971; *Tada et al.*, 2000]. The *SIF* curves for different λ values are shown in Fig. 3.3. It is observed that weight function based *SIFs* match boundary collocation based *SIFs* very well. The average error is as low as 1.66×10^{-7}%, which proves the validity of the derived weight function parameters above.

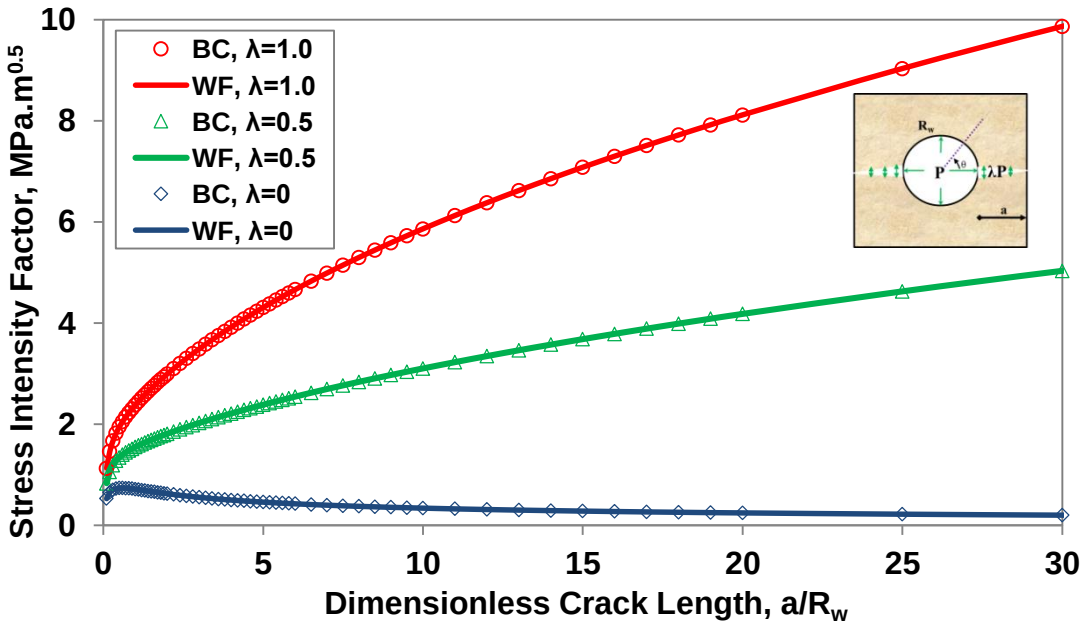

Figure 3.3 Comparison of the weight function (WF) based *SIFs* and boundary collocation (BC) based *SIFs* for Fig. 3.2-A (R_w = 1 *m*, *P* = 1 *MPa*).

3.3.2 Validation for Fig. 3.2-B

The weight function parameters are derived with loadings and boundary collocation based *SIFs* of Fig. 3.2-A. It is verified here that they can also be applied to calculate *SIF* for Fig. 3.2-B, and with similar accuracy. The general expression of boundary collocation based mode-I *SIF* for Fig. 3.2-B is [*Newman Jr*, 1971; *Tada et al.*, 2000],

$$K_I = \sigma\sqrt{\pi a}\begin{Bmatrix}(1-\lambda)\left\{0.5\left(3-\dfrac{a}{R_w+a}\right)^2\left[1+1.243\left(1-\dfrac{a}{R_w+a}\right)^3\right]\right\} \\ +\lambda\left\{1+\left(1-\dfrac{a}{R_w+a}\right)\left[0.5+0.743\left(1-\dfrac{a}{R_w+a}\right)^2\right]\right\}\end{Bmatrix},\ (\lambda = \text{constant, and } \lambda \geq 0) \tag{3.17}$$

From Fig. 3.4, it is observed that the boundary collocation based *SIFs* [*Newman Jr*, 1971; *Tada et al.*, 2000] agree well with the weight function based *SIFs* for Fig. 3.2-B. The average deviation is 0.21%, which proves the validity of the derived weight function parameters, and the weight function parameters are independent of applied loadings. Therefore, the weight function based *SIF* derived with data from Fig. 3.2-A can also be applied to calculate *SIF*s of the same fracture with different loadings.

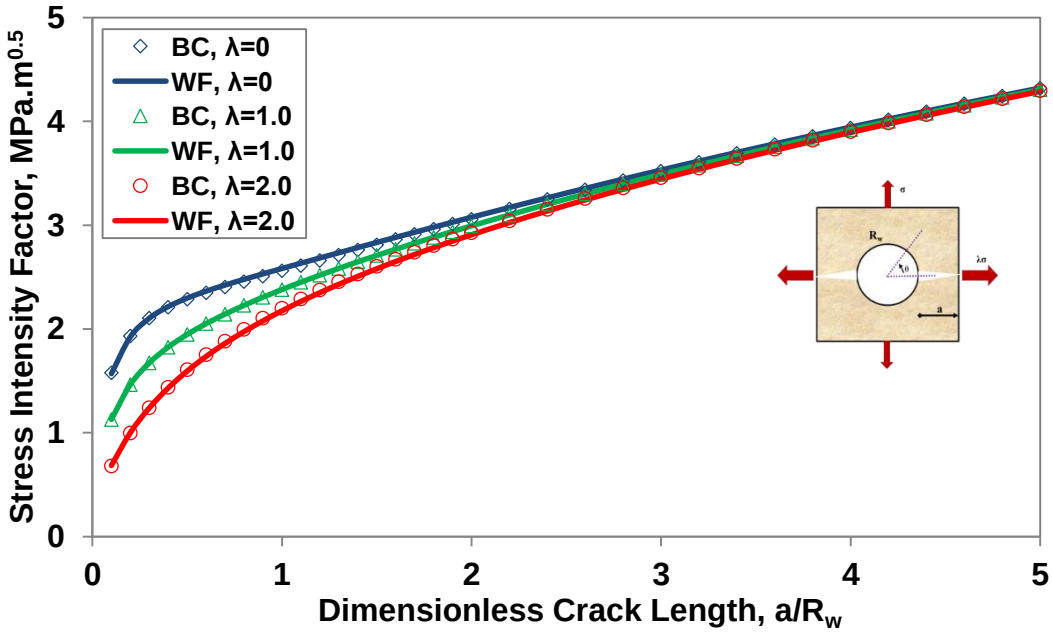

Figure 3.4 Comparison of the WF based *SIFs* and BC based *SIFs* for Fig. 3.2-B (R_w = 1 *m*, σ = 1 *MPa*).

3.4 Application in Petroleum Engineering

As mentioned earlier, the boundary collocation based *SIF* for symmetrical radial cracks emanating from borehole are only applicable to the case where: (1) crack aligns with principal stress direction, and (2) pressure inside crack is constant. However, generally, preexisting fractures do not align with principal stresses (see Fig. 3.5), and pressure inside fracture is not constant. The weight function parameters derived above can be applied to calculate *SIF* of Fig. 3.5 because they only depend on the ratio of borehole radius to crack length.

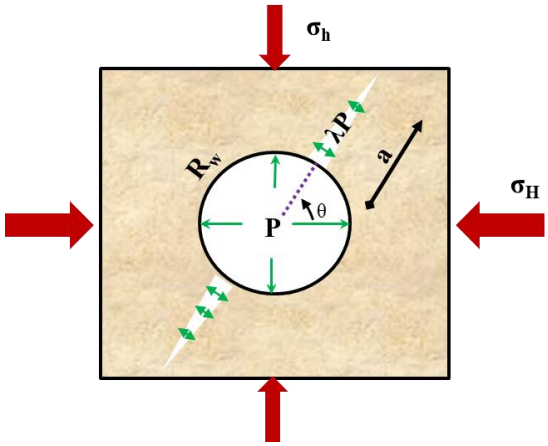

Figure 3.5 Loadings on inclined symmetrical radial cracks emanating from circular hole.

Pressure inside borehole represents fracturing pressure *P*. Pressure inside fracture (or perforation) is less than borehole pressure and non-uniform, thus $0 \le \lambda \le 1$. The two principal stresses are horizontal in-situ stresses, and $\sigma_h \le \sigma_H$. Wellbore radius is R_w, and fracture length is *a*.

If there is no fracture, the tangential stress at angle θ is:

$$\sigma_{\theta\theta}(R_w, x, \sigma_H, \sigma_h, \theta) = \lambda P - \left\{ \frac{\sigma_H + \sigma_h}{2}\left[1+\left(\frac{R_w}{R_w+x}\right)^2\right] - \frac{\sigma_H - \sigma_h}{2}\left[1+3\left(\frac{R_w}{R_w+x}\right)^4\right]\cos 2\theta - P\left(\frac{R_w}{R_w+x}\right)^2 \right\} \quad (0 \le x \le a)$$

(3.18)

Therefore, the weight function based *SIF* for the inclined symmetrical cracks is Eq. 3.19, and can be solved with the derived weight function parameters.

$$K_I = \int_0^a \sigma_{\theta\theta}(R_w, x, \sigma_H, \sigma_h, \theta) \frac{2}{\sqrt{2\pi(a-x)}}\left[1+M_1\left(1-\frac{x}{a}\right)^{1/2} + M_2\left(1-\frac{x}{a}\right) + M_3\left(1-\frac{x}{a}\right)^{3/2}\right] dx \quad (3.19)$$

3.4.1 Case I: Crack of non-constant fracturing pressure aligns with principal stress

If crack aligns with principal stress direction, and the pressure inside crack is constant, boundary collocation based *SIF* can be calculated with the superposition method (see Fig. 3.6). The boundary collocation based *SIF* of Fig. 3.6-A is equal to the sum of boundary collocation based *SIFs* of Figs. 3.6-B and 3.6-C. Weight function based *SIFs* for Figs. 3.6-B and 3.6-C can be calculated with the weight function parameters derived in section 3.2. The results of Fig. 3.6 are plotted in Fig. 3.7 with inputs from Table 3.1. From Fig. 3.7, it can be observed that the weight function based *SIFs* agree with boundary collocation based *SIFs* when pressure inside fracture is constant.

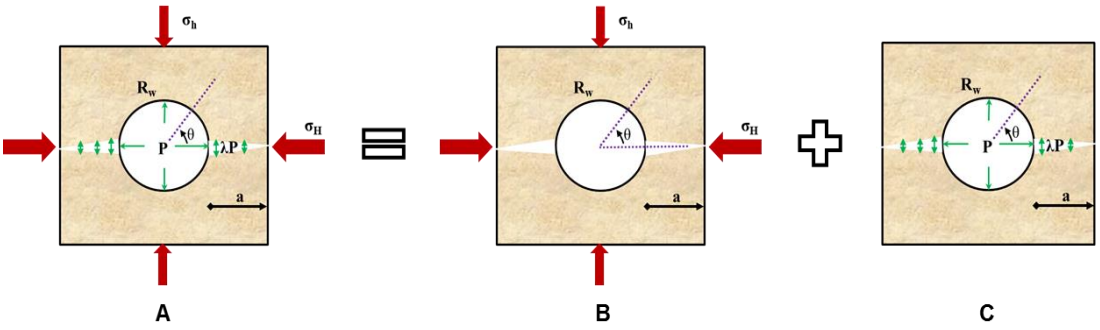

Figure 3.6 Loadings on symmetrical radial cracks aligning with principal stress.

Table 3.1 Inputs for Figs. 3.6 and 3.7

Parameter	Case I
Maximum Horizontal Stress: σ_H	20.0 *MPa*
Minimum Horizontal Stress: σ_h	15.0 *MPa*
Hole Radius: R_w	0.1 *m*
Preexisting Fracture Length: *a*	0~10 R_w
Fracturing Pressure inside hole: *P*	18 *MPa*

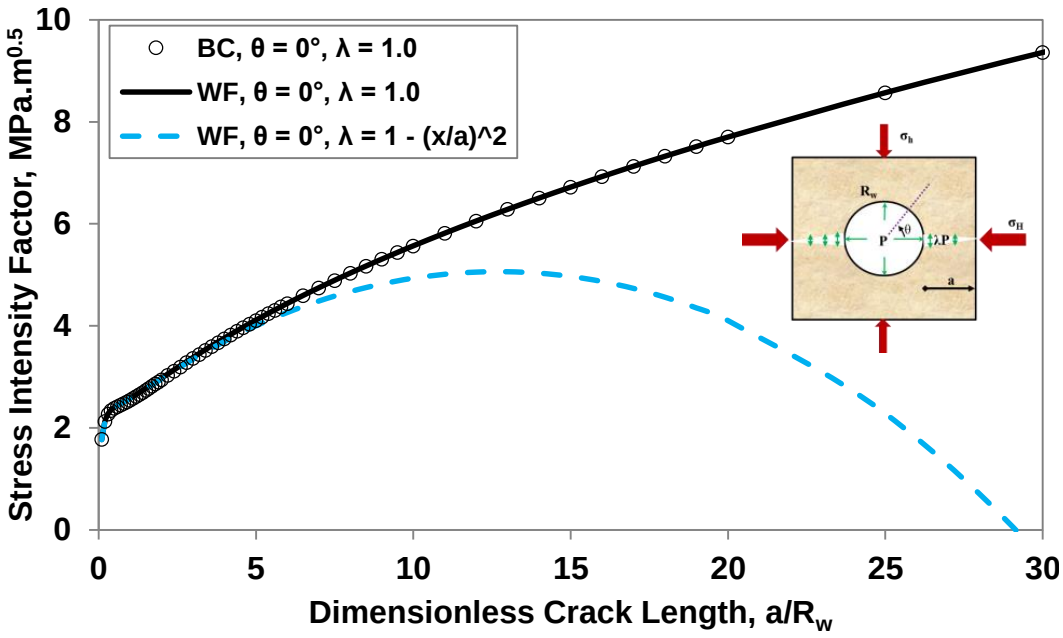

Figure 3.7 BC and WF based *SIFs* when crack aligns with principal stress direction under constant and non-constant pressure loadings.

When pressure inside fracture is non-constant, the boundary collocation based *SIF* [*Newman Jr*, 1971; *Tada et al.*, 2000] cannot be applied to calculate *SIF*, but weight function based *SIF* will still works. It is assumed that pressure inside fracture declines parabolically, which is

$$\lambda = 1 - \frac{x^2}{a^2}, (0 \le x \le a) \tag{3.20}$$

Weight function based *SIF* under non-constant pressure loading inside preexisting fracture can be calculated with Eqs. 3.18 and 3.19, weight function parameters of Table F-1 or correlations of weight function parameters, and input from Table 3.1. The results are plotted in Fig. 3.7 (dashed blue curve). It is observed that *SIF* of fracture with non-constant pressure is different from the case with constant pressure. Figure 3.7 shows the advantage of weight function in calculating *SIF* of fracture under

non-uniform loading. However, pressure declining function inside radial crack is a complex problem and may not be presented by a parabola. The determination of pressure declining function inside fracture is out of the scope of present study. The objective here is to prove that weight function method is advantageous in solving *SIF* of preexisting fracture under nonlinear loading.

3.4.2 Case II: Inclined Crack with constant fracturing pressure

For the inclined crack with constant fracturing pressure (assume $\lambda = 1.0$), Eqs. 3.6 and 3.17 cannot be used to calculate its *SIF* because they are only applicable to cracks aligning with principal stresses. *SIF* of inclined crack can be solved numerically with boundary collocation method, but a new numerical code is required for each inclined fracture. However, weight function based *SIF* can be calculated directly with Eqs. 3.18 and 3.19, weight function parameters in Table F-1 or correlations of weight function parameters, and input of Table 3.1. The results for case II is plotted in Fig. 3.8 (solid black curve).

3.4.3 Case III: Inclined Crack with non-constant fracturing pressure

For the inclined crack with non-constant fracturing pressure (assume λ is parabolic, which is Eq. 3.20), both Eqs. 3.6 and 3.17 are not suitable for the calculation of its *SIF*. Derivation of boundary collocation based *SIF* for this case is more complex. However, weight function based *SIF* can be calculated with Eqs. 3.18 and 3.19, weight function parameters of Table F-1 or correlations of weight function parameters, and input of Table 3.1. The results for case III is plotted in Fig. 3.8 (red dotted curve). It is observed that *SIF* of inclined crack is different from that of horizontal crack if other parameters are remained the same.

After calculating *SIFs* for the above three cases, the advantages of weight function method can be summarized as: (1) simple and convenient, (2) accurate, (3) good for nonlinear loadings on crack, (4) intrinsic character of specific fracture geometry.

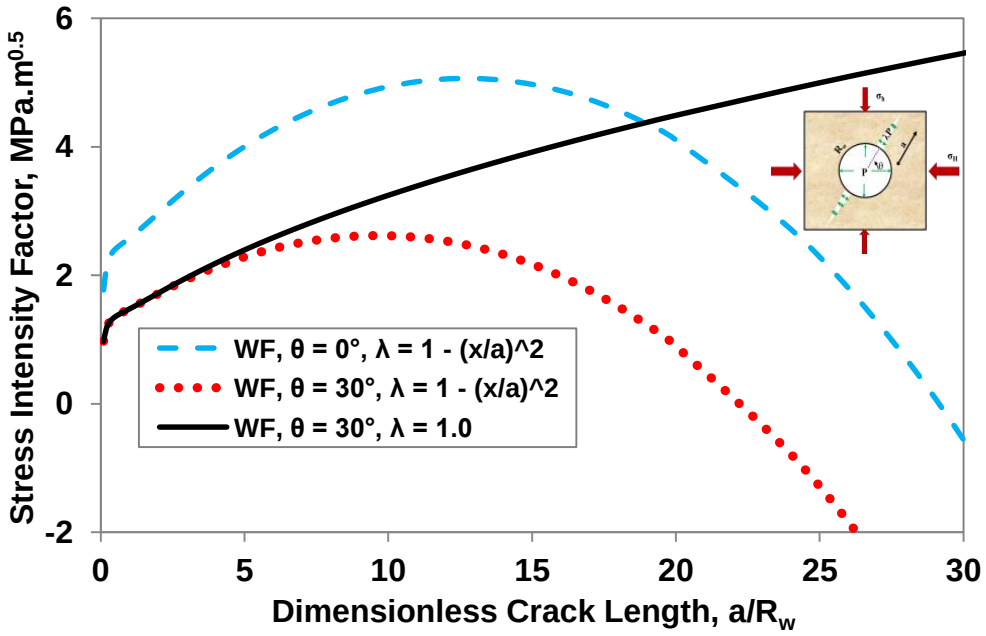

Figure 3.8 WF based *SIFs* for inclined cracks with both constant and non-constant pressures.

3.5 Discussion and Conclusions

Weight function parameters and *SIF* for symmetrical radial cracks emanating from borehole in an infinite plane have been derived by employing weight function approach. Weight function parameters are determined by the method of two reference stress intensity factors. The weight function based *SIF* is validated against available boundary collocation based *SIF* [*Newman Jr*, 1971; *Tada et al.*, 2000], and they are in good agreement with each other. A table of weight function parameters for different dimensionless crack length is provided in Appendix F. Three correlations of weight

function parameters with dimensionless crack length are also derived. The derived weight function parameters are applied to calculate *SIF* of: (1) horizontal fracture with non-constant pressure inside it; (2) inclined fracture with constant pressure; and (3) inclined fracture with non-constant pressure. The comparison of weight function based *SIFs* for the three cases exhibits its advantages over other methodologies in solving *SIFs* of fractures emanating from borehole.

The derived weight function parameters simplify the calculation of mode-I *SIF*. The weight function method has a great potential in predicting breakdown pressure and maximum horizontal in-situ stress. In Chapter 4, breakdown pressure is calculated with the weight function method, and compared against results by traditional fracture mechanics approaches.

Chapter 4. Breakdown Pressure Determination - A Fracture Mechanics Approach

4.1 Introduction

Fracture mechanics analysis of breakdown pressure is important in drilling (e.g., leak-off test data interpretation, fracture gradient determination), well construction (e.g., casing design), and hydraulic fracturing (e.g., required horse power, mini-frac analysis) [*Detournay and Carbonell*, 1997]. Leak-off test or extended leak-off test is conducted to measure breakdown pressure and closure stress during drilling, but the number of tests is limited due to the cost of testing and incurred increase of non-productive time. Mini-frac and micro-frac tests are conducted to acquire critical parameters for hydraulic fracturing design (e.g., pumping rate, fluid viscosity, breakdown pressure, etc.) before the main hydraulic fracturing treatment [*Economides and Nolte*, 2000]. Misinterpretation of pressure data from mini-frac tests of perforated borehole with continuum mechanics theory is not uncommon. There is significant error in fracture gradient prediction if preexisting natural fractures intersecting wellbore is ignored. In fact, intrinsic crack lengths (less than 10 mm) in intact granite is considered to be acceptable if assuming the coarse-grained matrix and the microscopic observation that grain boundaries act as potential micro cracks under tensile loading [*Rummel*, 1987]. Recent studies also suggest that the length of preexisting fractures (or defects) is shorter than borehole radius, which greatly affects the magnitude of the breakdown pressure [*Garagash and Detournay*, 1997]. Therefore, a reliable model is required to improve the accuracy of fracture gradient prediction, and may help reduce the costs of field tests.

In fracture mechanics, breakdown pressure is defined as a critical pressure at which fracture occurs at the tip of a preexisting fracture (natural fracture intersecting

borehole, defects on the borehole, and perforation emanating from the borehole are assumed as preexisting fracture) [*Ingraffea*, 1977]. In continuum mechanics, it is defined as the critical pressure at which crack occurs during the pressurization of a borehole [*Detournay and Carbonell*, 1997]. The peak pressure in the pressure vs. time curve during leak-off test, Mini-frac, or hydraulic fracturing operation is, therefore, considered to represent the breakdown pressure. Comparing pressure vs. time curves in both permeable and less permeable formations, it is found that the peak pressure of less permeable formation is obvious, while the other is not. Another important concept is fracture initiation pressure, which is defined as the critical pressure at which a fracture initiates from the position where a perforation intersects the borehole [*Wang and Dusseault*, 1991], or a small initial defect at the wellbore starts to develop [*Detournay and Carbonell*, 1997]. Fracture initiation pressure is equal to or slightly lower than breakdown pressure [*Ishijima and Roegiers*, 1983]. Two classical expressions of breakdown pressure have been widely used in the industry.

For impermeable rocks, Hubert-Willis formula [*Hubbert and Willis*, 1957] is selected:

$$P_b = 3\sigma_h - \sigma_H + T - p_o \tag{4.1}$$

For permeable rocks, Haimson-Fairhurst formula [*Haimson and Fairhurst*, 1967] is selected:

$$P_b = \frac{3\sigma_h - \sigma_H + T - 2\eta p_o}{2(1-\eta)} \tag{4.2}$$

where, P_b is the breakdown pressure, σ_h and σ_H are the minimum and maximum horizontal in-situ stresses, respectively, T is the tensile strength of the rock formation, p_o is the pore pressure, η is the poroelastic parameter in the range of 0 to 0.5, $\eta = 0$ for

impermeable rock, η = 0.5 for permeable rock [*Detournay and Cheng*, 1992]. Here, compression is positive, and tension is negative.

The validity and feasibility of Eqs. 4.1 and 4.2 are based on the assumptions that the near wellbore region is intact, homogeneous, and elastic. However, both the formation image log and core analysis have demonstrated the existence of natural fractures or mechanically induced fractures near wellbore in some wells, especially in naturally fractured formations [*Barton and Zoback*, 2002]. The existence of perforations also impairs the intact borehole wall assumption of continuum mechanics model. It has been observed that the influence of initial fracture length on breakdown pressure could not be neglected if it is about 4% of the borehole radius [*Bunger, Lakirouhani and Detournay*, 2010]. Therefore, it is important to introduce an advanced fracture mechanics model to improve the accuracy of breakdown pressure prediction.

To account for the preexisting fracture emanating from borehole, breakdown pressure has been addressed with fracture mechanics approaches by numerous researchers [*Abou-Sayed, Brechtel and Clifton*, 1978; *Ishijima and Roegiers*, 1983; *Atkinson*, 1987; *Rummel*, 1987; *Rummel and Hansen*, 1989; *Wang and Dusseault*, 1991; *Barry, Whittaker and Singh*, 1992; *Weijers, de Pater and Hagoort*, 1996; *Detournay and Carbonell*, 1997], but few calculates breakdown pressure with the weight function method. Breakdown pressure was once calculated with the weight function method [*Garagash and Detournay*, 1997], but it approximates weight function of fracture emanating from a borehole to that of edge fracture due to the unavailability of weight function for such fractures at that time. Furthermore, *Rummel* in 1987 developed one approach for breakdown pressure calculation by the superposition of *SIFs* caused by in-

situ stresses, bottomhole pressure, and pressure inside a fracture; but it is limited to preexisting fractures aligning with principal stress, and not independent of loadings. However, his results are going to be applied to prove the validity of the weight function method when solving breakdown pressure; as summarized in the following:

$$P_b = \frac{1}{h_o(b) + h_a(b)} \left(\frac{K_{IC}}{\sqrt{R_w}} + \sigma_H f(b) + \sigma_h g(b) \right) \tag{4.3}$$

where, K_{IC} is the fracture toughness of the rock formation, R_w is the borehole radius, b, $h_o(b)$, $h_a(b)$, $f(b)$, and $g(b)$ are geometrical coefficients defined in the following (the pressure inside fracture is assumed to be constant):

$$b = 1 + a/R_w \tag{4.4}$$

$$h_o(b) = 1.3\frac{b-1}{1+b^{1.5}} + 7.8\frac{\sin[(b-1)/2]}{2b^{2.5} - 1.7} \tag{4.5}$$

$$h_a(b) = \lambda(\pi b)^{0.5}\left(1 - \frac{2}{\pi}\sin^{-1}\frac{1}{b}\right) \tag{4.6}$$

$$f(b) = -2\left[(b^2 - 1)/\pi b^7\right]^{0.5} \tag{4.7}$$

$$g(b) = (\pi b)^{0.5}\left(1 - \frac{2}{\pi}\sin^{-1}\frac{1}{b}\right) + 2(b^2 + 1)\left[\frac{(b^2 - 1)}{\pi b^7}\right]^{0.5} \tag{4.8}$$

where, b is normalized fracture length, a is preexisting fracture length, λ is constant between 0 to 1.0 ($\lambda = 0$ means internal fracture pressure is equal to zero, and $\lambda = 1.0$ means internal fracture pressure is equal to bottomhole pressure). The physical model is demonstrated in Fig. 4.1.

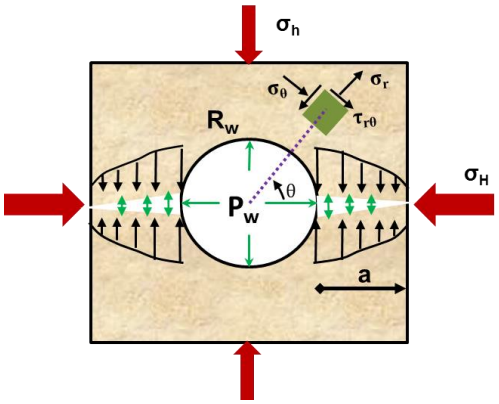

Figure 4.1 Stress distributions on radial cracks emanating from borehole.

where, P_w is the borehole pressure, while the internal fracture pressure is less or equal to P_w. The black arrows represent a non-uniform normal stress field acting on the crack faces because of near wellbore stress concentrations. The green arrows represent pressure distribution. σ_h and σ_H are the two far-field stresses. θ is the angle with respect to maximum horizontal principal stress, counterclockwise direction is positive. R_w is the borehole radius, and a is the half crack length.

Stress intensity factor is of central importance in fracture mechanics, it is defined as a parameter predicting the stress state in the vicinity of crack tip caused by a remote loading or residual stress [*Anderson*, 2005]. It is assumed that fracture initiation occurs once the following critical condition is satisfied,

$$K_I = K_{IC} \tag{4.9}$$

where, K_I is the *SIF* of Mode-I fracture (opening mode), K_{IC} is Mode-I fracture toughness. Sliding mode fracture is not considered for this study because shear strength of rock is several times than tensile strength.

Another fracture mechanics model has been developed to calculate breakdown pressure for a pair of symmetrical fractures (see Fig. 4.1) emanating from the borehole

[*Paris and Sih*, 1965; *Abou-Sayed, Brechtel and Clifton*, 1978; *Barry, Whittaker and Singh*, 1992], and it is as follows,

$$P_b = \frac{K_{IC} - g(a/R_w)\sqrt{\pi a}(\sigma_H - \sigma_h)Cos2\beta}{\sqrt{\pi a}\, f(a/R_w)} + \sigma_H Cos^2\beta + \sigma_h Sin^2\beta \qquad (4.10)$$

where, a is the preexisting fracture length, R_w is the borehole radius, $f(a/R_w)$ and $g(a/R_w)$ are geometric coefficients listed in Table 4.1, β is deviation angle between maximum principal stress and fracture axis. Because the original fracture model was developed by **P**aris and **S**ih, and extended to hydraulic fracturing by **A**bou-Sayed, Eq. 4.10 is referred to here as the ***PSA* method**. The *PSA* method is more advanced than *Rummel* method because it accounts for deviation angle and is independent of applied loadings, but limited to only a few discrete dimensionless fracture lengths as listed in Table 4.1.

Table 4.1 Values of $f\ (a/R_w)$ and $g\ (a/R_w)$ for two symmetrical radial cracks

[*Paris and Sih*, 1965; *Barry, Whittaker and Singh*, 1992]

a/R_w	**$f(a/R_w)$**	**$g(a/R_w)$**	**a/R_w**	**$f(a/R_w)$**	**$g(a/R_w)$**
0	2.26	3.39	1	1.38	1.45
0.1	2.06	2.93	1.5	1.26	1.29
0.2	1.83	2.41	2	1.2	1.21
0.3	1.7	2.15	3	1.13	1.14
0.4	1.61	1.96	5	1.06	1.07
0.5	1.57	1.83	10	1.03	1.03
0.6	1.52	1.71	∞	1.00	1.00
0.8	1.43	1.58			

The near wellbore stress field is nonlinear because wellbore drilling disturbed the distribution of in-situ stresses [*Fjar et al.*, 2008; *Jaeger, Cook and Zimmerman*, 2009]. In addition, the internal fracture pressure may not be uniform either due to fluid leak-off. The limitations of current fracture models are,

(1) Most of the formulas of *SIF* in the handbook are only applicable to uniform and linear loading [*Tada et al.*, 2000];

(2) Boundary collocation method is employed to calculate the stress intensity factor for a pair of symmetrical radial fractures emanating from a circle, but it is only applicable to fracture aligning with principal stress, and not applicable to nonconstant pressure inside the preexisting fracture [*Newman Jr*, 1971; *Tada et al.*, 2000];

(3) Some fracture models cannot account for nonuniform pressure distribution inside the preexisting fracture, and are only applicable to a specific dimensionless fracture length [*Paris and Sih*, 1965; *Barry, Whittaker and Singh*, 1992].

(4) Some fracture mechanics models are not independent of loadings [*Rummel*, 1987; *Rummel and Hansen*, 1989].

(5) *J*-integral method is reliable and has been used extensively in numerical analysis, but is not convenient due to complex numerical integral [*Rice*, 1968b; a].

(6) Technically, *SIF* can be solved with the weight function method proven by Bueckner [*Bueckner*, 1970] and Rice [*Rice*, 1972], and developed by Glinka and his group [*Glinka and Shen*, 1991; *Shen and Glinka*, 1991; *Zheng and Glinka*, 1995; *Glinka*, 1996; *Zheng, Kiciak and Glinka*, 1997; *Kiciak, Glinka and Burns*, 2003]. The weight function for a pair of symmetrical radial cracks emanating from a circle, however, to the best of our knowledge, is not derived [*Detournay and Carbonell*, 1997].

The objective of present study is to integrate the stress concentration near the borehole, the nonlinear internal pressure in the preexisting fracture, the dimensionless crack length (ratio of crack length to borehole radius), and the deviation angle into one weight function model for the prediction of breakdown pressure. In Chapter 3, the weight function parameters of symmetrical fractures emanating from borehole were derived. They are applied to improve the accuracy of breakdown pressure prediction. Effects of preexisting fracture orientation and length, in-situ stress contrast, and fracture toughness on breakdown pressure are investigated. The influence of fluid viscosity and flow rate on fluid pressure loss inside preexisting fracture is not considered directly because of the complexity in deriving the analytical solution. Instead, a nonlinear equation of pressure inside preexisting fracture is assumed. In the sensitivity analyses, breakdown pressure is compared against results obtained by *PSA* and *Rummel* methods. Furthermore, the weight function based breakdown pressure is also compared with that by traditional method (see Eqs. 4.1 and 4.2), and is verified against the measured breakdown pressure during hydraulic fracturing experiments in our research partner's laboratory and published experimental data.

4.2 Procedures of Breakdown Pressure Calculation by Weight Function Method

The physical model is a pair of symmetrical radial fractures emanating from the borehole, as demonstrated in Fig. 4.1. The detailed derivation is presented earlier in Chapter 3.

According to the failure criterion stated in Eq. 4.9, the following nonlinear equation is obtained for breakdown pressure calculation,

$$K_{IC}=\int_0^a \sigma\left(\sigma_H,\sigma_h,P_w,P(x,Pw),x,\theta\right)\frac{2}{\sqrt{2\pi(a-x)}}\left[1+M_1\left(1-\frac{x}{a}\right)^{1/2}+M_2\left(1-\frac{x}{a}\right)+M_3\left(1-\frac{x}{a}\right)^{3/2}\right]dx \quad (4.11)$$

where, K_{IC} is mode-I fracture toughness, the right hand side is stress intensity factor, x is the distance from wellbore wall, and $P(x, P_w)$ is the internal pressure distribution in the preexisting fracture, P_w is borehole pressure, R_w is the borehole radius, σ_H and σ_h are maximum and minimum horizontal principal stress, θ is the fracture deviation angle from maximum principal stress (clockwise direction is negative), M_1, M_2 and M_3 are weight function parameters derived in Chapter 3, and can be calculated with Mathematica program presented in Appendix E, or with their correlations (Eqs. 3.14 and 3.16), $\sigma\left(\sigma_H,\sigma_h,P_w,P(x,P_w),x,\theta\right)$ is the net stress[4] acting at the position of fracture, which is as following:

$$\sigma\left(\sigma_H,\sigma_h,P_w,P(x,P_w),x,\theta\right)=P(x,P_w)-\left\{\begin{array}{l}-P_w\left(\frac{R_w}{R_w+x}\right)^2+\frac{\sigma_H+\sigma_h}{2}\left[1+\left(1+\frac{R_w}{R_w+x}\right)^2\right]\\ -\frac{\sigma_H+\sigma_h}{2}\left[1+3\left(1+\frac{R_w}{R_w+x}\right)^4\right]Cos2\theta\end{array}\right\} \quad (4.12)$$

After examining Eqs. 4.11 and 4.12, it is observed the only unknown parameter is P_w, which is part of the nonlinear Eq. 4.11, and can be solved numerically.

The major steps for solving weight function parameters are listed in the following:

Step I: Calculate net stress acting at the position of fracture surface with Eq. 4.12.

[4] It is called net stress, but not net effective stress, because the object being studied is fracture surface. Pore pressure is not explicitly shown in Eq. 4.6 because the far field stress is total stress. For example, after stop pumping, vertical planar fracture closes gradually, if tensile strength of rock is ignored, when pressure inside fracture is equal to total minimum horizontal in-situ stress, the net stress is equal to zero.

Step II: Calculate weight function parameters with Mathematica code in Appendix E.

Step III: Solve nonlinear equation of breakdown pressure numerically.

Step IV: Collect and sort data, conduct sensitivity analysis.

4.3 Sensitivity Study of Breakdown Pressure

In this section, the influence of preexisting crack length and orientation, fracture toughness, in-situ stress contrast, and internal pressure distribution on breakdown pressure are investigated. The internal pressure distribution of preexisting fracture was assumed to be constant, although the flow rate and fluid viscosity affect friction pressure losses in perforations [*Lord and Shah*, 1994], they are not considered here. The basic input is listed in Table 4.2.

In this analysis, the breakdown pressure obtained by the weight function method is compared against both *PSA* and *Rummel* method. The comparison allows for validating this approach and identifying its advantages and disadvantages.

Table 4.2 Basic parameters and their values for prediction of breakdown pressure

Parameter	Value
Maximum horizontal stress: σ_H	20.0 *MPa*
Minimum horizontal stress: σ_h	15.0 *MPa*
Mode I fracture toughness: K_{IC}	3.0 $MPa \cdot m^{1/2}$
Borehole radius: R_w	0.1 m
Preexisting crack length: a	Vary
Preexisting crack orientation: θ	Vary

4.3.1 Influence of Preexisting Crack Length on Breakdown Pressure

The stress concentration near the borehole varies with distance from the borehole wall. It is difficult to determine the exact penetration depth or natural fracture

length, although the laboratory testing or logging tools can assist this estimation. The change of breakdown pressure versus preexisting crack length is shown in Fig. 4.2.

It can be observed that (1) breakdown pressure decreases with increasing dimensionless crack length for the case being considered (if the stress contrast is different, the relationship will vary, as is shown later in Section 4.3.3); (2) when dimensionless crack length is less than 0.1, breakdown pressure is very sensitive to dimensionless crack length, and grows exponentially with decreasing dimensionless crack length; (3) Results of the three methods agree well with each other; (4) *PSA* method, however, can only predict breakdown pressure for several specific fracture geometries, which limits its application in the field; (5) *Rummel's* method can be used to calculate the breakdown pressure for fractures aligning with principal stresses, and give very similar results as the Weight function method. Based on the analysis, it is suggested that the prediction of breakdown pressure of a preexisting fracture can be improved if a relatively accurate length is known, especially for short fractures. It also proves the validity of weight function method in solving breakdown pressure.

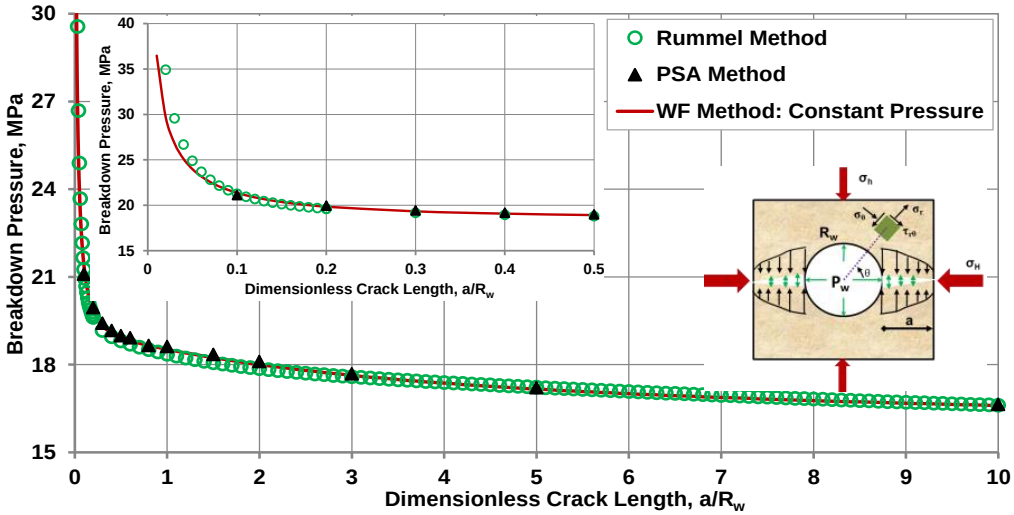

Figure 4.2 Effect of dimensionless crack length on breakdown pressure.

4.3.2 Influence of Crack Orientation on Breakdown Pressure

Perforation guns are recommended to be oriented in the maximum principal stress direction to prevent or alleviate fracture tortuosity near the borehole [*Dusterhoft*, 1994; *Yew*, 1997; *Economides and Nolte*, 2000]. In the field, however, it is difficult to orient the gun to an exact prescribed direction, and sometimes the orientation of in-situ stress is not determined precisely. In addition, most of the preexisting natural fractures can deviate a few degrees from the maximum horizontal in-situ stress direction [*Higgins*, 2006]. It is known that the near wellbore stress varies with the hoop direction [*Fjar et al. 2008*]; consequently, *SIFs* of preexisting fractures at different deviation angle will vary. However, *Rummel's* method does not account for deviation angle, so it is not included in studying the effects of crack orientation on breakdown pressure.

Keeping other parameters in Table 4.2 constant and varying crack deviation angle from -90° to 90°, the results of two dimensionless crack lengths are obtained and shown in Fig. 4.3.

It can be observed that (1) breakdown pressure varies with crack deviation angle in a sinusoidal fashion, and increases with increasing deviation angle; (2) Breakdown pressures by both methods agree well with each other for different dimensionless crack lengths. In engineering application, breakdown pressure is suggested to be calculated statistically by integrating weight function based breakdown pressure with statistical information of preexisting fracture orientation.

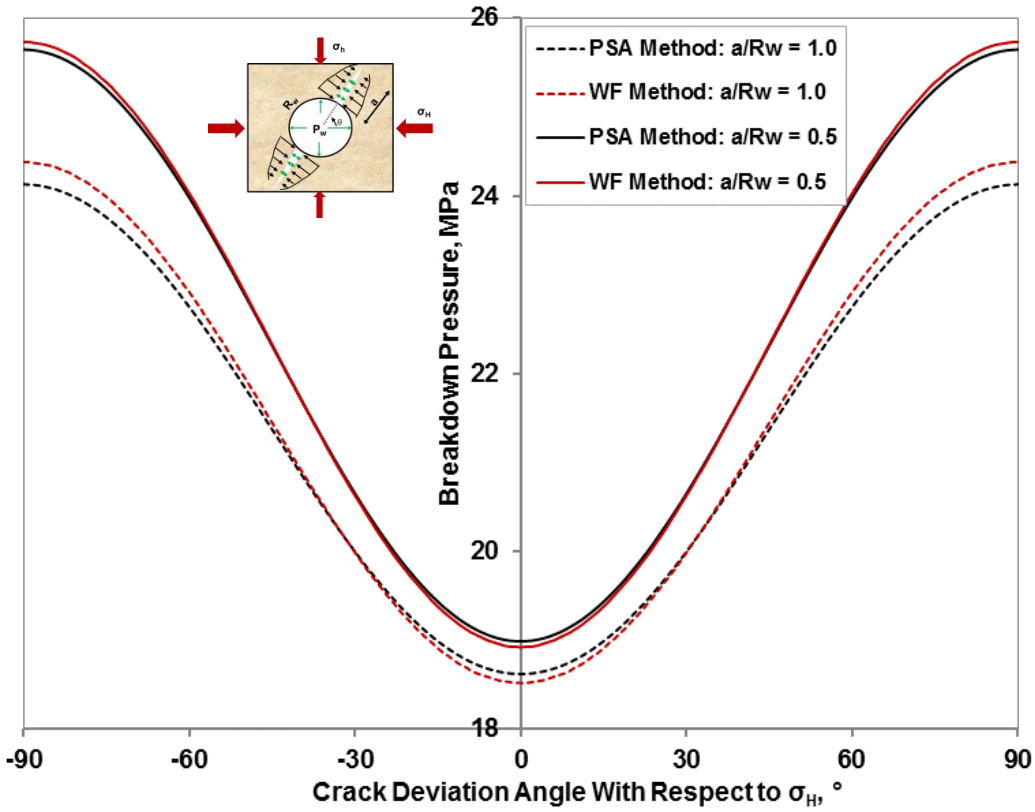

Figure 4.3 Effect of crack deviation angle on breakdown pressure.

4.3.3 Influence of Stress Contrast on Breakdown Pressure

In-situ stress anisotropy is common [*Jaeger, Cook and Zimmerman*, 2009], therefore, studying the influence of stress contrast on breakdown pressure can help engineers foster perception of breakdown pressure. Keeping other parameters in Table 4.2 constant, given fracture aligns with principal stress, and bottomhole pressure and internal fracturing pressure are equal; the sensitivity of *SIF* of preexisting fractures to the change of stress contrast is investigated. The maximum horizontal in-situ stress, σ_H = 20, 25, 30, and 45 MPa (corresponds to three stress contrasts of 5, 10, 15, 30 MPa), are considered. The results are shown in Fig. 4.4.

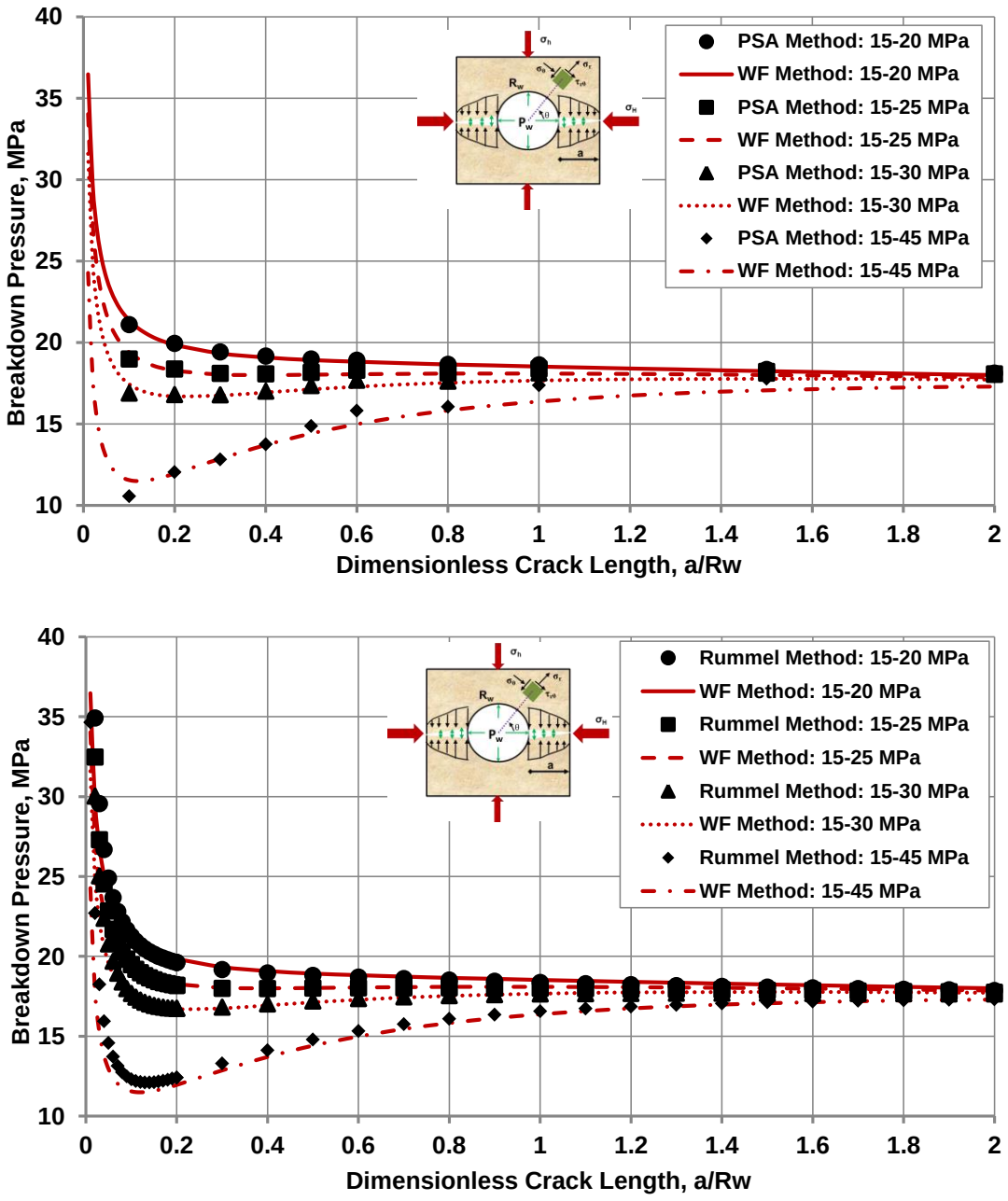

Figure 4.4 Effect of in-situ stress contrast on breakdown pressure.

It can be observed that (1) at higher stress contrast, the breakdown pressure does not decrease monotonically with increasing dimensionless crack length; (2) a minimum value of breakdown pressure near the wellbore can be observed at high stress contrasts by the weight function and *Rummel's* methods; (3) breakdown pressure will decrease to

zero if stress contrast is high enough, because tangential stress near the borehole will become tension at relatively high stress contrasts; (4) results by both *Rummel's* and weight function methods agree well with each other, but results by *PSA* and weight function methods do not agree well at high stress contrasts. This analysis has proven that it might be incorrect to assume that the breakdown pressure for long fracture is lower than for short fracture if their stress contrasts are different.

4.3.4 Influence of Fracture Toughness on Breakdown Pressure

Fracture toughness changes with rock types [*Barry, Whittaker and Singh*, 1992]. For the same type of rock, increasing temperature or confining pressure will increase the fracture toughness [*Zhao and Roegiers*, 1993; *Al-Shayea, Khan and Abduljauwad*, 2000]. Therefore, the field measured fracture toughness is usually larger than the laboratory measured fracture toughness [*Shlyapobersky, Wong and Walhaug*, 1988]. Keeping other parameters in Table 4.2 constant, given the same internal fracturing pressure as bottomhole pressure, the effect of *SIF* of preexisting fractures on fracture toughness is investigated (K_{IC} = 3.0, 4.0, and 5.0 $MPa\text{-}m^{0.5}$). The results are shown in Fig. 4.5.

It is observed that (1) the breakdown pressure increases with increasing fracture toughness; (2) breakdown pressures by both methods are in good agreement for different fracture toughness; and that (3) the difference in breakdown pressure becomes less with increasing dimensionless crack length. Results of weight function and Rummel methods agree well with each, but are not re-plotted.

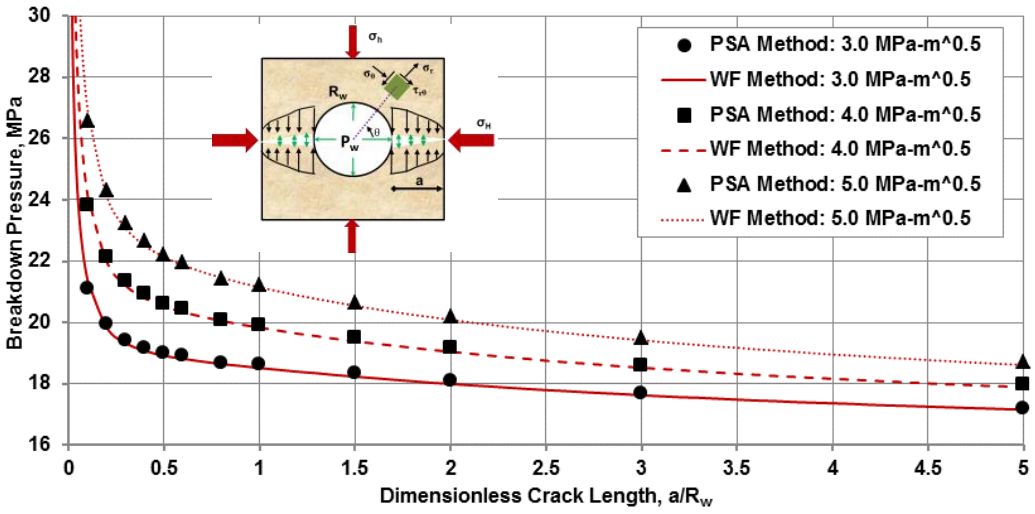

Figure 4.5 Effect of fracture toughness on breakdown pressure.

4.3.5 Influence of Internal Fracture Pressure on Breakdown Pressure

The objective is not to derive an accurate pressure decline function inside preexisting fracture, but highlight the advantages of the weight function method in solving nonlinear fracture mechanics problems. The *PSA* method is only applicable to the case with constant internal fracture pressure. Rummel's model can be applied to calculate the breakdown pressure with nonlinear internal fracture pressure, but one must re-derive another $h_a(b)$ function (Eq. 4.6) for one specific internal fracture pressure distribution every time if the internal fracture pressure function changes [*Rummel*, 1987], which is inconvenient for engineering applications. The weight function method, however, can be applied to study fractures under any nonlinear stress distribution because it is a characteristic property of fracture and independent of loadings. Therefore, only the weight function method is studied in this section.

The internal pressure distribution of impermeable rock is assumed to be constant, while it is assumed to be a declining function for permeable rock. Assuming

that the pressure at the heel of preexisting fracture is equal to the borehole pressure, and pressure at the tip of the preexisting fracture is zero because of the existing fluid lag [*Jeffrey*, 1989]. It is assumed that fracturing fluid pressure at the tip of fracture is zero. Therefore, the nonlinear fracture pressure distribution is assumed as follows:

$$P(x, R_w) = P_w\left(1 - \frac{x^2}{a^2}\right) \tag{4.13}$$

Keeping all parameters in Table 4.2 constant, two cases are investigated: Case I: pressure declines as Eq. 4.13; Case II: internal pressure is constant, and equal to the bottomhole pressure. The results are depicted in Fig. 4.6. It is observed that breakdown pressure by declining pressure function is about twice that of constant internal fracture pressure. This emphasizes that the determination of internal pressure distribution function is critical in the prediction of an accurate breakdown pressure.

The pressure drop inside a preexisting fracture is different in both unconventional and conventional reservoirs. For unconventional reservoirs, the fluid viscosity is relatively low, so pressure drop inside the fracture is relatively low, and pressure distribution inside the preexisting fracture can be assumed to be constant. However, for conventional reservoirs, fluid viscosity is relatively high, pressure drop inside the preexisting fracture cannot be ignored, and pressure distributions are considered as nonlinear.

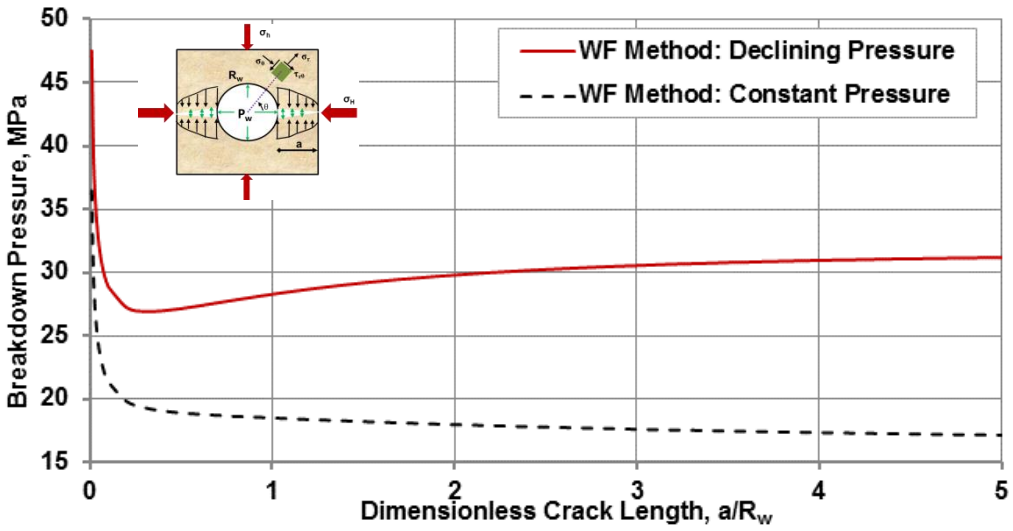

Figure 4.6 Effect of pressure distribution inside preexisting fracture on breakdown pressure**.**

4.4 Comparison of Breakdown Pressures by Traditional and Weight Function Methods

The objective of this section is to verify whether the traditional methods over/under estimate breakdown pressure. The parameters employed in this comparison are listed in Table 4.3.

Table 4.3 Basic parameters for breakdown pressure comparison

σ_H	σ_h	*Pore Pressure*	Fracture Toughness	Tensile Strength	Fracture Orientation	Poroelastic Constant, η *
20 MPa	15 MPa	1.7 MPa	2.41 MPa-$m^{0.5}$	20 MPa	0°	0 - 0.5

*η *is in the range of 0 to 0.5,* η = 0 is impermeable rock, η = 0.5 is permeable rock.

For impermeable rocks (e.g., porosity is very low), the poroelastic effect is negligible, so η = 0. According Eq. 4.2, breakdown pressure is

$$P_{b_1} = \frac{3\sigma_h - \sigma_H + T - 2\eta p_o}{2(1-\eta)} = \frac{3\times 15 - 20 + 20 - 0}{2} = 22.5\,\text{MPa}$$

For the same impermeable rock, at the same conditions, if Eq. 4.1 is employed, its value is

$$P_{b_2} = 3\sigma_h - \sigma_H + T - p_o = 3\times 15 - 20 + 20 - 1.7 = 43.3\,\text{MPa}$$

It is observed that P_{b_1} and P_{b_2} are different, so the results of traditional methods themselves (Eqs. 4.1 and 4.2) are not consistent.

For permeable rocks, if the poroelastic effect is non-negligible, assume $\eta = 0.5$, according to Eq. 4.2,

$$P_{b_3} = \frac{3\sigma_h - \sigma_H + T - 2\eta p_o}{2(1-\eta)} = \frac{3\times 15 - 20 + 20 - 1.7}{1} = 43.3\,\text{MPa}$$

It is observed that P_{b_3} is the same as P_{b_2}, and P_{b_1} is lower than P_{b_3}. Generally, if other conditions are the same, breakdown pressure in impermeable formation is lower than that in permeable formation. Therefore, P_{b_2} calculated by Eq. 4.1 overestimates breakdown pressure because it does not account for the change of pore pressure by poroelasticity. The analysis of the differences between the breakdown pressures by different continuum mechanics is out of the scope of the dissertation, so no deep analysis is provided here.

If there is preexisting fractures intersecting borehole, fracture mechanics model is employed to calculate breakdown pressure. Using the parameters in Table 4.3, breakdown pressure is calculated by weight function method, and the results are plotted in Fig. 4.7.

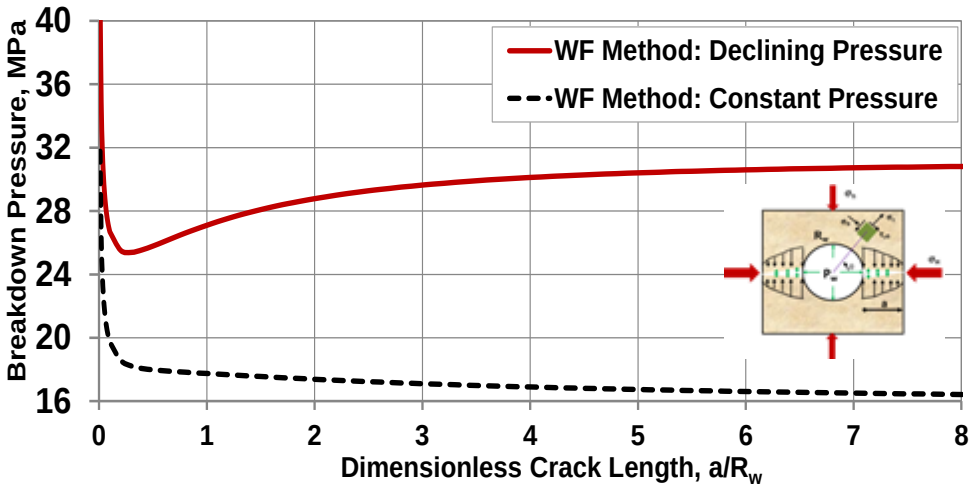

Figure 4.7 Breakdown pressure by weight function method (R_w = 0.1 m, θ = 0°).

For impermeable rock, fracturing fluid pressure inside fracture is assumed constant and the same as bottomhole pressure because fluid does not leak into formation. Its breakdown pressure is the dashed curve in Fig. 4.7. If Eq. 4.1 is applied to calculate breakdown pressure for this case, breakdown pressure is overestimated too much because P_{b_2} is much higher than the maximum value of the dashed curve. If Eq. 4.2 is used, breakdown pressure is underestimated if dimensionless fracture length is less than about 0.1; breakdown pressure is overestimated if dimensionless fracture length is greater than about 0.25 (usually natural fracture length is greater than this value).

For permeable rock, pressure inside fracture is non-constant and less than borehole pressure because of fluid leak-off into formation. Its breakdown pressure is the red curve in Fig. 4.7. Equation 4.2 yields results much higher than that by weight function method (e.g., P_{b_3} is higher than the maximum value of red curve in Fig. 4.7).

Therefore, based on the above comparison, it is concluded that both traditional methods overestimate breakdown pressure because of the negligence of preexisting

fracture, and fracture mechanics model is required to improve the accuracy of fracture gradient prediction.

4.5 Experimental Verification

4.5.1 Verification with In-house Laboratory Experimental Data

Breakdown pressure was acquired from hydraulic fracturing experiments described in Section 2.5. It should be pointed out that many laboratory experiments could not fulfill the research objectives because of the following reasons: uncertainties of sample properties caused by environment temperature during sample drying (some of the experiments were done in summer, while others were conducted in winter), the difficulty to predict accurate fracture toughness under confining pressure [*Zhao and Roegiers*, 1993], uncemented interface between simulated borehole and sample, complexities in sample preparation and conducting hydraulic fracturing experiments in laboratory [*Haimson*, 1981]. In addition, the prolonged test and expenses does not allow the repetition of all the experiments reported here. Therefore, in order to verify the theoretical breakdown pressures against the measured values, only 6 successful experiments are selected from more than 40 sets of experiments. The experimental conditions and breakdown pressures for these tests are listed in Table 4.4. Fracture toughness at the experimental conditions cannot be measured in the laboratory, so it is fine-tuned to calibrate the theoretical breakdown pressures against the measured values.

The steps of experimental verification are as follows:

Step I: Collect measured breakdown pressures (see Table 4.4).

Step II: Calculate theoretical breakdown pressures with parameters in Table 4.4 by fine-tuning fracture toughness at experimental conditions.

Step III: Compare theoretical breakdown pressure with experimental results (see Fig. 4.8).

Table 4.4 Experimental conditions and breakdown pressures in the laboratory

Number	Min In-situ Stress σ_h (MPa)	Max In-situ Stress σ_H (MPa)	Inclination Angle β °	Measured Breakdown Pressure P_b (MPa)
1-4-15	1	4	15	7.4
1-4-30	1	4	30	8.5
1-4-45	1	4	45	9.3
1-4-60	1	4	60	9.8
1-6-30	1	6	30	10.4
1-6-45	1	6	45	10.5
1-6-60	1	6	60	15.6

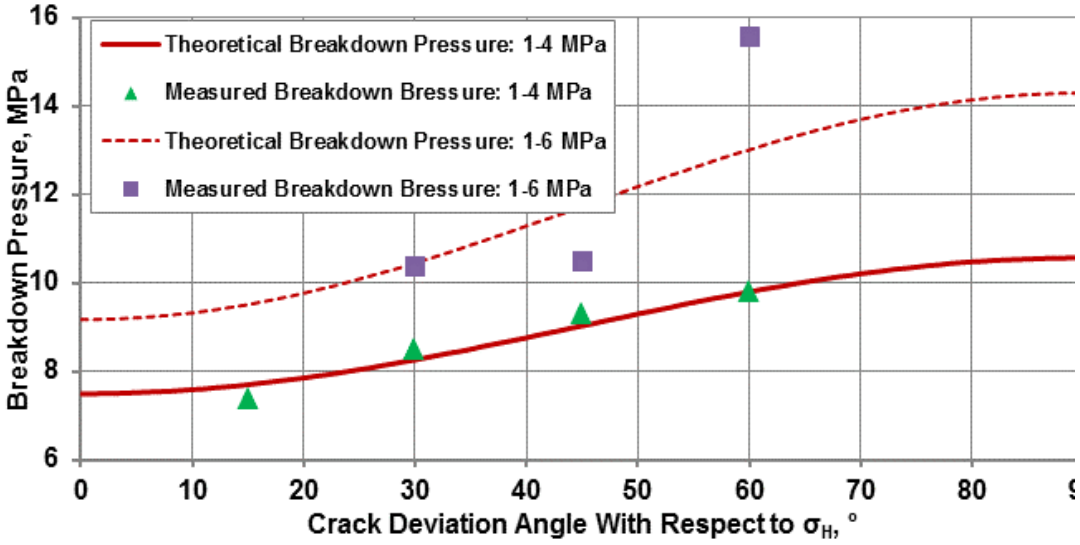

Figure 4.8 Breakdown pressure verification with in-house experimental results.

The fine-tuned fracture toughness at 1-4 *MPa* is 2.3 *MPa-m*$^{0.5}$, the one at 1-6 *MPa* is 2.9 *MPa-m*$^{0.5}$.

It can be observed from Fig. 4.8 that theoretical and experimental breakdown pressures are in good agreement when σ_h = 1 MPa, σ_H = 4 MPa, but not as good when σ_h = 1 MPa, σ_H = 6 MPa. The possible reasons for this can be attributed to the variation of fracture toughness with deviation angle and stress contrast, or the position of fracture initiation does not take place at the tip of the preexisting fracture at high deviation angle stress contrast.

4.5.2 Verification with Published Data by Rummel

Experimental data from *Rummel's* publication [*Rummel*, 1987] is selected for the verification of weight function in predicting breakdown pressure, and is listed in Table 4.5. The preexisting fracture is assumed as symmetrical micro defects perpendicular to the borehole wall, and aligning with the principal stresses. Its length is unknown, but is assumed to be less than ~15 mm. The experimental data from mini-cores is not selected due to the boundary effect. The internal fracture pressure is assumed to be constant and equal to the bottomhole pressure.

Table 4.5 Experimental conditions and breakdown pressures by Rummel

Experiment	R_w (m)	σ_h (MPa)	σ_H (MPa)	β °	P_b (MPa)	K_{IC} (MPa·m$^{0.5}$)
Granite block (1 m^3)	0.015	2	5	~0	15.5	2.47±0.2
Deep borehole in granite formation (250 m)	0.048-0.066	5	7	~0	10-17	1.79±0.22

Firstly, compare the weight function based breakdown pressure with the experimental results from the 1 m^3 Epprechtstein granite block. The breakdown pressure is calculated with the same parameters listed on the second row of Table 4.5.

Considering the uncertainties in fracture toughness measurements, so two curves of breakdown pressure are plotted in Fig. 4.9 for the lower and upper limits of fracture toughness. The observed breakdown pressure of 15.5 MPa covers the region of dimensionless crack length shown by the blue line, which covers the length from ~1.95 mm to ~ 3.3 mm (*Rummel* call it as micro crack. The micro crack length is hard to be measured before the experiment, but can be back calculated with breakdown pressure data). It is observed that crack extension pressure is about 8 MPa when the initial fracture is extended to about 40 mm, which can be explained by Fig. 4.10. Assuming the observed breakdown pressure is correct, the estimated fracture length is from 30 mm to 48 mm (as shown by the blue line in Fig. 4.10), the observed fracture length is in this region; assuming the observed fracture length is correct, the estimated breakdown pressure is from 7.4 MPa to 8.4 MPa (as shown by the black line in Fig. 4.10), the observed breakdown pressure is in this region too.

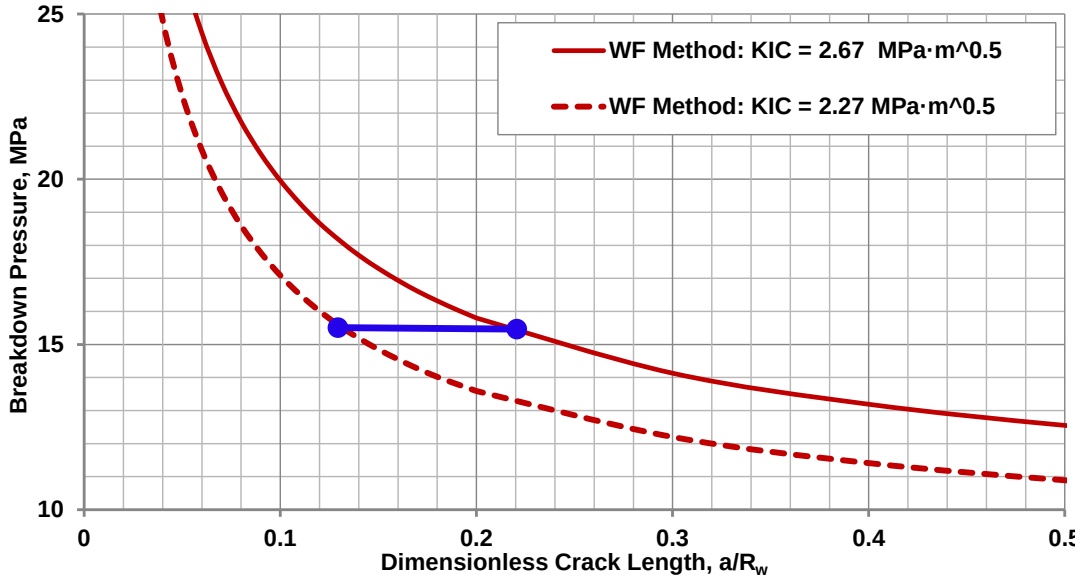

Figure 4.9 Breakdown pressure verification during the first injection with 1 m^3 block (R_w = 0.015 m).

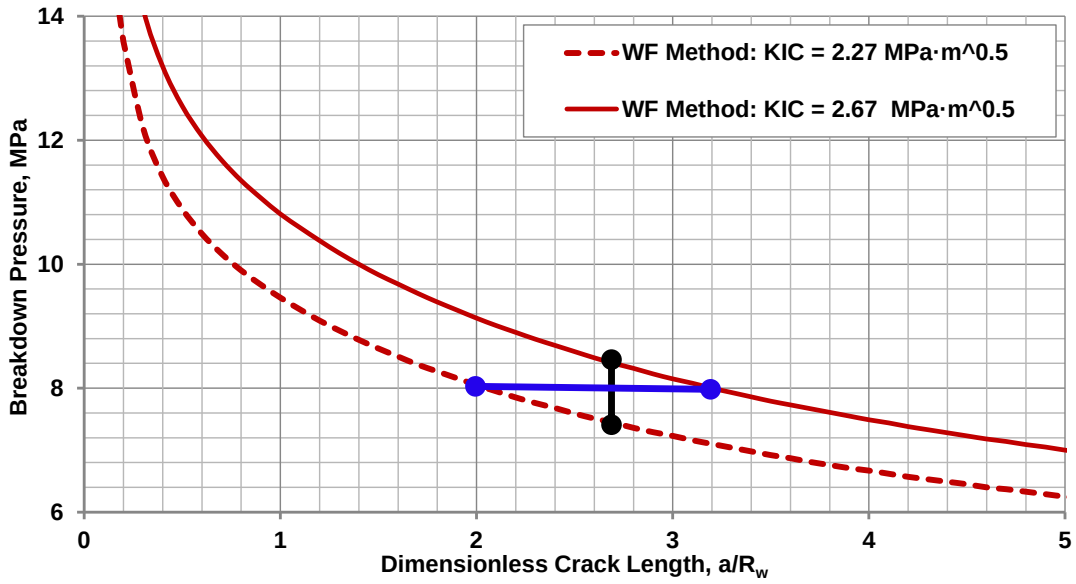

Figure 4.10 Breakdown pressure verification during the second injection with 1 m^3 block (R_w = 0.015 m).

Secondly, compare the weight function based breakdown pressure with the experimental results from the deep boreholes at the depth of 250 m in Falkenberg granite formation. The breakdown pressure is calculated with the same parameters listed on the third row of Table 4.5. Considering the uncertainties in the measurements of fracture toughness and open hole radius, so four curves of breakdown pressure are plotted in Fig. 4.11 for the lower and upper limits of fracture toughness and borehole radius. The observed breakdown pressure is in the range of 10 MPa to 17 MPa. The shaded region shows the possible natural fracture lengths. If the borehole radius is 48 mm, the preexisting fracture length ranges from ~9.6 mm to ~13.44 mm; if the borehole radius is 66 mm, the preexisting fracture length ranges from ~ 2.72 mm to 11.22 mm. Both regions are accepted length scale of micro fractures (or call defects) defined by *Rummel*.

Therefore, according to the comparison results between observed and weight function based breakdown pressure, the applicability of the weight function method for breakdown pressure prediction is proven.

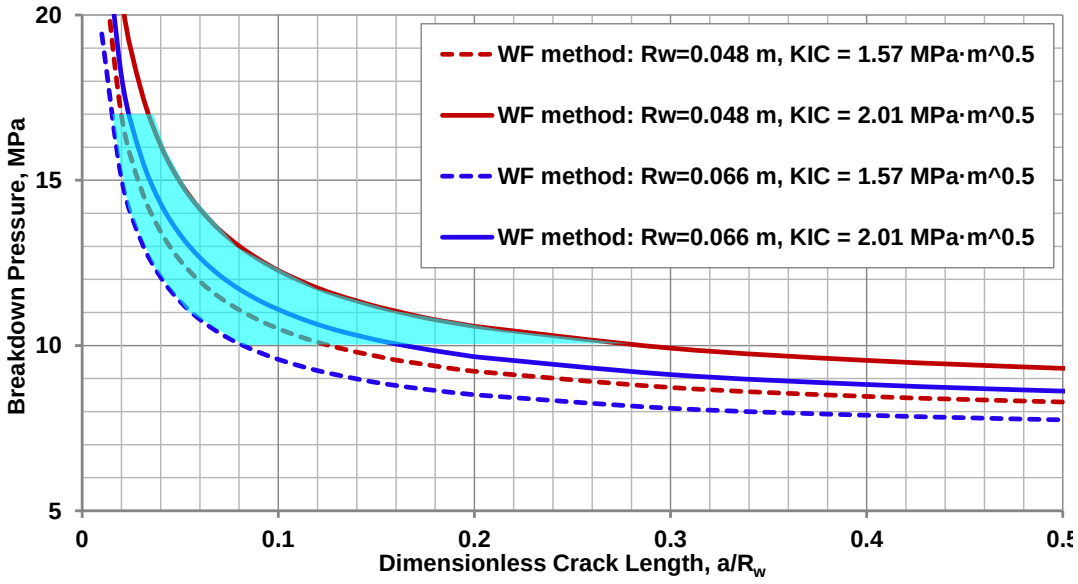

Figure 4.11 Breakdown pressure verification in the field

4.6 Discussion and Conclusions

The weight function method is applied successfully to calculate breakdown pressure, and its results are verified against both the *PSA* and Rummel's methods. Overall, results of the three methods are in good agreement. The *PSA* method deviates a little bit more from the weight function method at relatively higher stress contrast. This proves the validity of the weight function method in solving for the breakdown pressure. The weight function method also captures phenomena that cannot be observed by *PSA* method, and covers a wide range of dimensionless fracture length. The weight function method can measure breakdown pressure of fractures deviated from principal stresses, and is independent of loadings, but Rummel's method cannot. In addition,

breakdown pressure by traditional continuum mechanics methods is compared with the weight function method. It is observed that traditional models overestimate breakdown pressure. Furthermore, breakdown pressure by the weight function method is verified against hydraulic fracturing experiments in the laboratory and field. The results from in-house experiments are matched by fine-tuning fracture toughness at experimental conditions. Even then, complexities of hydraulic fracturing experiments, in some cases, still lead to disagreement between the experimental and theoretical breakdown pressures at higher stress contrast. The weight function based breakdown pressure also matches the laboratory and field results from Rummel's publication.

Sensitivity analyses are conducted to investigate the influence of preexisting crack length and orientation, fracture toughness, in-situ stress contrast, and internal pressure distribution on breakdown pressure. It is concluded that: (1) breakdown pressure does not always decrease with increasing fracture length; at a relatively higher in-situ stress contrast, the breakdown pressure may goes to zero because tangential stress near the wellbore might become tension at relatively higher stress contrast; (2) breakdown pressure is highly sensitive to a short dimensionless crack length; (3) breakdown pressure changes sinusoidally with the preexisting crack deviation angle; (4) increasing fracture toughness will increase breakdown pressure, the difference in breakdown pressure, however, becomes less as dimensionless crack length increases; (5) breakdown pressure for the case with nonlinear pressure distribution inside fracture is approximately twice that of constant internal pressure distribution.

The pressure distribution selected here for inside preexisting fracture is only to show its effect on breakdown pressures for constant and nonconstant internal pressure

distributions. Accurate determination of breakdown pressure can only be made with a detailed internal pressure function consisting of flow rate, viscosity, borehole pressure, preexisting length and orientation, etc. In reality, other types of nonlinear stresses, such as thermal stress, chemical stress, if they exist, should also be included in a weight function for calculating *SIFs* under these conditions. The *PSA* method, however, cannot account for these nonlinear stresses in the calculation of *SIF*.

This chapter covers only weight functions for a pair of symmetrical radial cracks emanating from the borehole. One can develop new weight functions for other types of cracks emanating from the borehole. For example, there might be a single, or multiple fractures emanating from the borehole. The weight functions developed here can be applied to both deviated and vertical wellbores because they only depend on dimensionless fracture length. The difference in *SIFs* between vertical and deviated wellbores is caused by different near wellbore stress concentrations.

So far, a comprehensive understanding about rock fracture mechanics has been established after studying mixed-mode fracture propagation in Chapter 2, deriving weight function based *SIF* for a pair of symmetrical cracks emanating from borehole in Chapter 3, and applying weight function method to predict breakdown pressure in Chapter 4. The ultimate goal is to improve the efficiency of hydraulic fracturing by integrating all the available information. Armed with the knowledge of rock fracture mechanics, the next step is to give a relook at brittleness in Chapter 5 and develop a fracability index model for improving the quality of reservoir characterization in Chapter 6 by integrating the disciplines of rock fracture mechanics and petrophysics.

Chapter 5. Petrophysical Approach to Brittleness Prediction: Woodford, Barnett, and Eagle Ford Shale

5.1 Introduction

Hydraulic fracturing has played a significant role in exploration and production of tight reservoirs, but field experience suggests that not all targets rich in *TOC* (Total Organic Content) are good fracturing candidates [*Britt and Schoeffler*, 2009; *King*, 2012]. Therefore, in order to maximize the efficiency of hydraulic fracturing, integrated geomechanics, petrophysics and well logging analysis have been applied in unconventional reservoir characterization. The major parameters included in the integrated analysis are: *TOC*, thermal maturity, mineralogy, fracture density and orientation, thickness, porosity, permeability, relative permeability, saturation, density, *PVT* behavior, static and dynamic Geomechanical properties (Young's modulus, Poisson's ratio), uniaxial and triaxial compressive strength, internal friction angle, cohesion, Biot's coefficient, tensile strength, fracture toughness, closure stress, proppant embedment, propped and unpropped fracture conductivity, brittleness, shale stability and compatibility with injected completion fluid. Among these, brittleness is selected as the critical parameter for investigation. Recently, brittleness is included as an essential parameter in petrophysics report. Improvement of brittleness evaluation in shale gas formation can help better appraise its potential to be a fracturing candidate [*Rickman et al.*, 2008], but, until now, there is no universally accepted definition and measurement method of brittleness.

Brittleness is defined as a material property that rupture or fracture with little or no plastic flow [*Jackson, Mehl and Neuendorf*, 2005]. It may be stated that materials with higher brittleness exhibit the following characteristics [*Hucka and Das*, 1974;

Singh, 1986; *Jarvie et al.*, 2007; *Rickman et al.*, 2008; *Wang and Gale*, 2009; *Yarali and Kahraman*, 2011; *Heidari et al.*, 2013]:

- Fail immediately at peak stress: from the stress-strain tests, it is observed that the brittle rock fails immediately when peak stress reaches rock strength, while the ductile rock does not fail immediately, but continue to absorb energy, and finally fails at large strain.
- Low values of elongation: when two brittle and ductile samples with the same dimensions are pulled under the same tensile stress, the brittle sample is elongated less than the ductile one before failure.
- Fracture failure: when two brittle and ductile samples with the same dimensions are struck by the same hammer with the same force, the brittle sample is easier to be fractured than the ductile one.
- Formation of fine particles: when two brittle and ductile samples with the same dimensions are struck by the same hammer at the same force, fine particles is easy to form in brittle sample.
- Higher ratio of compressive and tensile strength: material with low tensile strength and high compressive strength fails immediately after stress reaches rock strength.
- Higher resilience: the deformed sample with high resilience is difficult to recover its original shape, so this type of material is brittle.
- Higher internal friction angle: the internal friction angle defines the easiness of a material to slip along the fracture surface. Lower the internal friction angle, easier the material to slip along the fracture surface. The brittle rock does not

slip as much as ductile rock before rock failure, so high internal friction angle means high brittleness.

- Formation of cracks during indentation: given two brittle and ductile samples with the same dimensions, cracks are easier to form in brittle rock when conducting indentation test.
- Higher Young's modulus and lower Poisson's ratio: brittle material experiences less axial strain and lateral strain because of its high Young's modulus and low Poisson's ratio.
- Higher percent of quartz and carbonate: quartz and carbonate are brittle minerals, formation with high percent of brittle minerals are prone to be brittle.
- Lower porosity: Internal friction angle can be correlated with porosity. Low porosity corresponds to high internal friction angle, thus high brittleness.
- Big cuttings in drilling: drilling in a formation of high brittleness creates big cuttings.
- Lower rate of penetration in drilling: drilling in brittle formation creates big cuttings, which leads to the difficulty of wellbore cleanout; in addition, brittle formation is much stronger, and not easy to be drilled; thus, high brittleness reduces rate of penetration.
- Big coal blocks in coal mining. It is observed that big coal blocks are easy to form in brittle coal field.

There are more than 20 expressions of brittleness in the literature, and are listed in Table 5.1. The brittlenesses B_1 through B_{16} are obtained by rock mechanics tests, B_{17} and B_{18} are obtained by either rock mechanics tests or logging (internal friction angle

can be derived from porosity or sonic logging [*Weingarten and Perkins*, 1995; *Chang, Zoback and Khaksar*, 2006]), B_{19} is obtained by density and sonic logging [*Rickman et al.*, 2008], B_{20} and B_{21} are obtained by mineralogical logging or XRD tests in the laboratory [*Jarvie et al.*, 2007; *Wang and Gale*, 2009]. It is not affordable to evaluate brittleness of thick shale formation by laboratory testing due to the limitation of turnaround time and expense. Therefore, brittlenesses B_1 through B_{16} are not as practical as B_{17} through B_{21}.

From physical viewpoint, it is believed that mineralogical brittleness is reliable [*Jarvie et al.*, 2007; *Slatt and Abousleiman*, 2011]. In order to obtain reliable results by B_{17}, B_{18} and B_{19}, it is important to compare them with mineralogical brittleness; however, presently, a comparison of these brittlenesses is not available in the literature. Mineralogical logging is one of the most expensive logging services, and is not available for all wells. In addition, a complete set of sonic logging data is not easily available; sometimes there is only compressional sonic slowness, but no shear slowness because it is more expensive. Therefore, it is valuable to develop correlations between mineralogical brittleness and other cheap and easy accessible parameters.

In the laboratory, it is proven that brittleness decreases with increasing porosity [*Heidari et al.*, 2013]. In addition, internal friction angle is correlated with porosity and compressional slowness [*Weingarten and Perkins*, 1995; *Chang, Zoback and Khaksar*, 2006]. Compressional slowness can be correlated with porosity [*Mavko, Mukerji and Dvorkin*, 2009], and rocks of different porosities exhibit different compressional slownesses. Therefore, it is possible to correlate mineralogical brittleness with porosity and compressional slowness.

Table 5.1 Selected Expressions of Brittleness

Formula	Variable declaration	Test Method	Reference
$B_1 = (H_m\text{-}H)/K$	H and H_m are macro and micro-hardness, K is bulk modulus	Hardness test	[*Honda and Sanada*, 1956]
$B_2 = q\sigma_c$	q is percent of debris (<0.6 mm diameter); σ_c is compressive strength	Proto impact test	[*Protodyakonov*, 1962]
$B_3 = \varepsilon_{ux} \times 100\%$	ε_{ux} is unrecoverable axial strain	Stress strain test	[*Andreev*, 1995]
$B_4 = (\varepsilon_p\text{-}\ \varepsilon_r)/\ \varepsilon_p$	ε_p is peak of strain, ε_r is residual strain		[*Hajiabdolmajid and Kaiser*, 2003]
$B_5 = \tau_p\text{-}\ \tau_r/\ \tau_p$	τ_p and τ_r are peak and residual of shear strengths		[*Bishop*, 1967]
$B_6 = \ \varepsilon_r/\ \varepsilon_t$	ε_r and ε_t are recoverable and total strains		[*Hucka and Das*, 1974]
$B_7 = W_r/W_t$	W_r and W_t are recoverable and total strain energies		
$B_8 = \sigma_c/\sigma_t$	σ_c and σ_t are compressive and tensile strength	Uniaxial compressive strength and Brazilian test	
$B_9 = (\sigma_c\text{-}\ \sigma_t)/(\ \sigma_t + \sigma_c)$			
$B_{10} = (\sigma_c\sigma_t)/2$			[*Altindag*, 2003]
$B_{11} = (\sigma_c\sigma_t)^{0.5}/2$			
$B_{12} = H/K_{IC}$	H is hardness, K_{IC} is fracture toughness	Hardness and fracture toughness test	[*Lawn and Marshall*, 1979]
$B_{13} = c/d$	c is crack length, d is indent size for Vickers indents at a specified load; empirically related to H/K_{IC}	Indentation test	[*Sehgal et al.*, 1995]
$B_{14} = P_{inc}/P_{dec}$	P_{inc} and P_{dec} are average increment and decrement of forces		[*Copur et al.*, 2003]
$B_{15} = F_{max}/P$	F_{max} is maximum applied force on specimen, P is the corresponding penetration.		[*Yagiz*, 2009]
$B_{16} = H \times E/K_{IC}^2$	H is hardness, E is Young's modulus, K_{IC} is fracture toughness	Hardness, stress strain, and fracture toughness test	[*Quinn and Quinn*, 1997]
$B_{17} = 45° + \varphi/2$	φ is internal friction angle	Mohr circle or logging data	[*Hucka and Das*, 1974]
$B_{18} = Sin\varphi$			
$B_{19} = (E_n + \nu_n)/2$	E_n and ν_n are normalized dynamic Young's modulus and dynamic Poisson's ratio defined in Eqs. 5.3 and 5.4.	Density and sonic logging data	Modified from [*Rickman et al.*, 2008]
$B_{20} = (W_{qtz})/W_{Tot}$	W_{qtz}, is the weight of quartz, W_{Tot} is total mineral weight.	Mineralogical logging or XRD in the laboratory	[*Jarvie et al.*, 2007]
$B_{21} = (W_{qtz} + W_{dol})/W_{Tot}$	W_{qtz} and W_{dol} are weights of quartz and dolomite, W_{Tot} is total mineral weight.		[*Wang and Gale*, 2009]
$B_{22} = (W_{QFM} + W_{Carb})/W_{Tot}$	W_{QFM} is weight of quartz, feldspar, and mica; W_{Carb} is weight of carbonate minerals consisting of dolomite, calcite, and other carbonate components. W_{Tot} is total mineral weight.		*Defined in this paper*

The objectives are to: (1) identify the differences and similarities among various logging based brittlenesses, and benchmark its definition; (2) develop new correlation of mineralogical brittleness with neutron porosity or compressional slowness for Woodford, Barnett, and Eagle Ford shales; (3) develop two global correlations between brittleness and neutron porosity and compressional slowness with the data from three typical shale reservoirs; and (4) finally, verify the predicted brittleness from correlations against mineralogical brittleness measured for different wells.

5.2 Benchmark Brittleness Definition

Among all brittleness formulas in Table 5.1, one must first address which definition is the most appropriate. The understanding of mineralogical brittleness has advanced in recent years. Originally, the mineralogical brittleness accounted only for the weight fraction of quartz [*Jarvie et al.*, 2007]. Later, it was observed that the presence of dolomite tends to increase the brittleness of shale, so both quartz and dolomite were included in brittleness definition [*Wang and Gale*, 2009]. It is also observed that silicate minerals such as feldspar and mica are more brittle than clay in shale reservoirs. Besides dolomite, other carbonate minerals, such as calcite in limestone, are also more brittle than clay. Therefore, a new expression of brittleness is proposed, which includes silicate minerals (such as quartz, feldspar, and mica), and brittle carbonate minerals (such as calcite and dolomite).

$$B_{22} = \frac{W_{QFM}}{W_{Tot}} + \frac{W_{Carb}}{W_{Tot}} \approx \frac{W_{QFM} + W_{calcite} + W_{dolomite}}{W_{Tot}} \tag{5.1}$$

where, W_{QFM}/W_{Tot} is the weight fraction of quartz, feldspar, and brittle mica, which are silicate minerals; W_{Carb}/W_{Tot} is the weight fraction of carbonate minerals consisting of

dolomite, calcite, and other brittle carbonate. To calculate mineralogical brittleness with B_{22}, one needs to find spectrolithology data in LAS file, where weight fractions of quartz, feldspar, and mica is *WQFM*, weight fractions of carbonate, dolomite, and calcite are named as "*WQFM*", "*WCAR*", "*WDOL*", and "*WCLC*", respectively.

Brittleness B_{18}, B_{19} and B_{22} are selected for brittleness evaluation because they can be derived from well logging data and are easy to apply. Tracks of B_{17} and B_{18} are calculated with internal friction angle, but only B_{18} is selected for evaluation because it is in the range of 0 to 1. Because the literature formula for B_{19} is not clear [*Rickman et al.*, 2008], and after in-house verification, it is redefined as:

$$B_{19} = \frac{E_n + v_n}{2} \tag{5.2}$$

where, E_n and v_n are normalized Young's modulus and Poisson's ratio as shown below:

$$E_n = \frac{E - E_{\min}}{E_{\max} - E_{\min}} \tag{5.3}$$

$$v_n = \frac{v_{\max} - v}{v_{\max} - v_{\min}} \tag{5.4}$$

In Eqs. 5.3 and 5.4, E_{min} and E_{max} are the minimum and maximum dynamic Young's modulus for the investigated formation, v_{min} and v_{max} are minimum and maximum dynamic Poisson's ratio for the investigated formation, E and v are Young's modulus and Poisson's ratio over the depth. E_{min}, E_{max}, v_{min}, v_{max} are constants, E and v are variables. Brittleness B_{19} indicates that formation with higher Young's modulus (E) and lower Poisson's ratio (v) is of relatively higher brittleness.

In order to prove the validity of B_{22} for brittleness calculation, it is compared against tracks of B_{18} and B_{19} for Woodford, Barnett, and Eagle Ford shales. Similar

results as Fig. 5.1 are observed in wells from different plays and different wells in the same play. Figure 5.1 indicates that the three tracks are similar to each other, but B_{18} is better than B_{19} because its absolute value is closer to that of B_{22}. If B_{20} and B_{21} in Table 5.1 are selected to demonstrate mineralogical brittleness, they do not match well with tracks of B_{18} and B_{19} because B_{20} and B_{21} neglect other brittle components. Since B_{18}, B_{19}, and B_{22} are independent to each other, and their trends are similar, all of them can be employed to characterize brittleness of unconventional shale, among which B_{22} is the best brittleness index, followed by B_{18} and B_{19}.

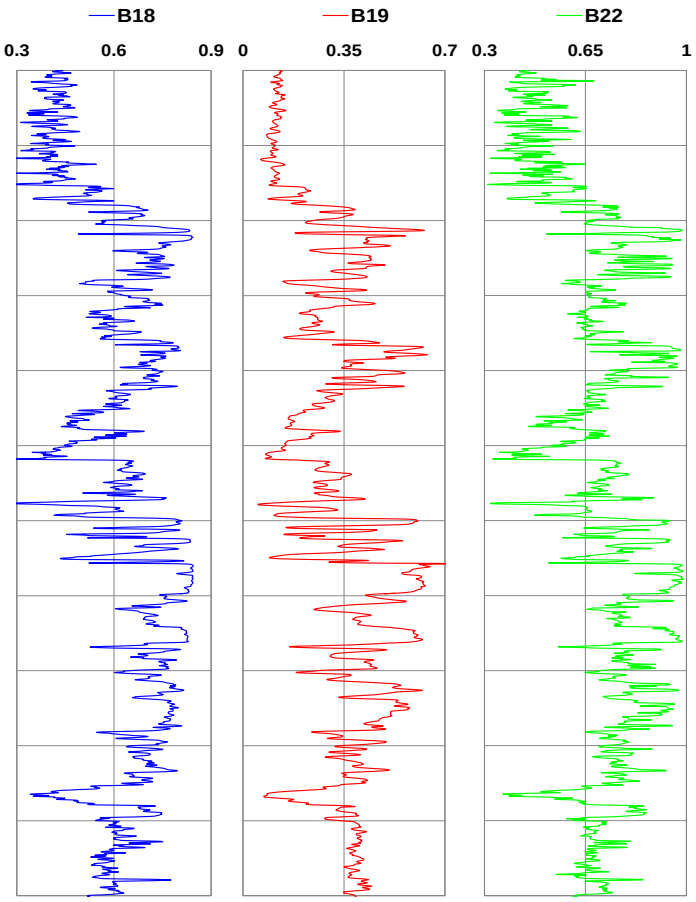

Figure 5.1 Comparison of different brittleness indices for Barnett shale (the major unit in vertical direction is 100 ft).

5.3 Prediction of Brittleness with Neutron Porosity for Typical Shale Reservoirs

Porosity is an important parameter in reservoir development, and is divided into two categories: total porosity and effective porosity [*Tiab and Donaldson*, 2011]. Fluid flow in porous medium is governed by effective porosity, but rock mechanical properties, such as Young's modulus, Poisson's ratio, brittleness, etc. are (or partly) controlled by total porosity. Because internal friction angle is correlated with porosity [*Chang, Zoback and Khaksar*, 2006], and increasing porosity reduces brittleness in the laboratory study [*Heidari et al.*, 2013], a correlation between brittleness and porosity may be developed if sufficient source data is available.

Both neutron and density porosities are available in most LAS files. In shale reservoirs, it is found that mineralogical brittleness is not correlated well with the density porosity (*DPHI*), but is associated well with the neutron porosity (*NPHI*). In present study, three separate correlations between mineralogical brittleness and neutron porosity are developed for Woodford, Barnett, and Eagle Ford shales. One global correlation between mineralogical brittleness and neutron porosity with available data from the three shale plays is also developed. The LAS files also include enhanced neutron porosity data. It is observed that the enhanced neutron porosity is also linearly correlated with neutron porosity. Once the correlation between brittleness and neutron porosity is obtained, one can derive the correlation between brittleness and enhanced neutron porosity. In the following sections, the porosity means neutron porosity.

5.3.1 Correlation of Brittleness with Porosity for Woodford Shale

Woodford shale is located in south-central Oklahoma, covering approximately 11,000 square miles. The burial depth ranges from ~6,000 ft to ~11,000 ft. The

thickness ranges from ~120 to ~220 ft across the play. It is a Devonian-age shale bounded by limestone above and undifferentiated strata below [*Council and Consulting*, 2009]. The Woodford shale formation can be divided into Upper, Middle, and Lower members [*Hester, Schmoker and Sahl*, 1990]. Well logging data from four wells of Woodford shale are selected for developing the correlation between mineralogical brittleness and neutron porosity, which is plotted in Fig. 5.2.

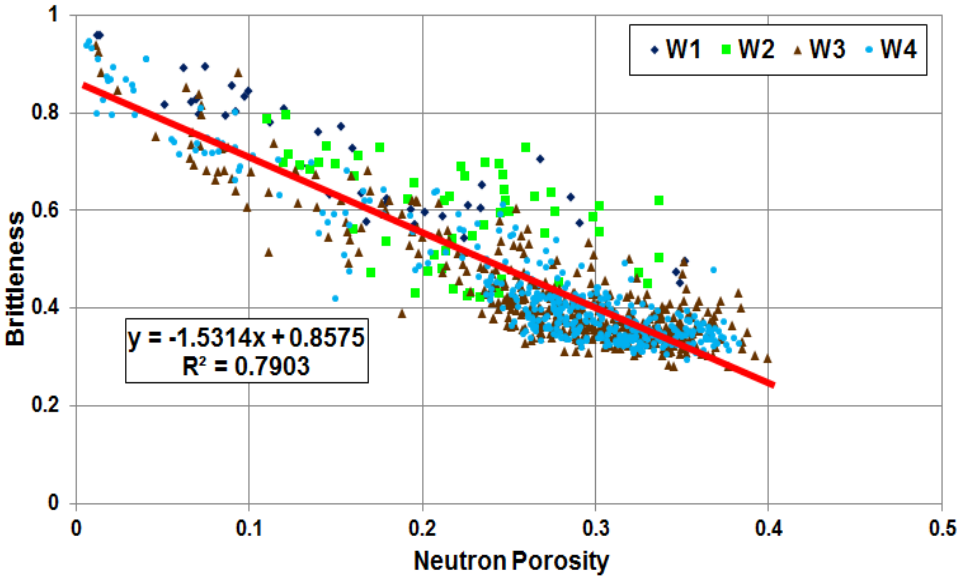

Figure 5.2 Correlation of brittleness with porosity for Woodford shale.

The vertical resolution of the logging data is 0.5 ft. It is understood that lithology may not change every 0.5 ft, therefore, the tracks of raw logging data are averaged over every 1.5, 3.0, 5.0, 10.0, 15.0, and 20.0 ft. After examining correlation quality and similarity between processed and raw logging curves, a 10 ft interval is selected for data processing. Similar data processing method is also applied to the development of correlations for other plays.

The correlation of brittleness with porosity for Woodford shale then is developed,

$$B_{23} = -1.5314 \times \phi + 0.8575$$
$$R^2 = 0.7903 \tag{5.5}$$

where, ϕ is neutron porosity, R^2 is coefficient of determination.

5.3.2 Correlation of Brittleness with Porosity for Barnett Shale

Barnett shale is located in the Fort Worth Basin of north-central Texas, covering about 5,000 square miles. The burial depth varies from ~6,500 ft to ~8,500 ft. The average thickness ranges from ~100 to ~600 ft across the play. It is a Mississippian-age shale bounded by Marble Falls limestone above and Chappel Limestone below [*Council and Consulting*, 2009]. The Barnett shale formation can be divided into Upper and Lower members [*Fisher et al.*, 2002]. Well logging data from three wells of Barnett shale are selected for the development of correlation between mineralogical brittleness and neutron porosity, and are plotted in Fig. 5.3.

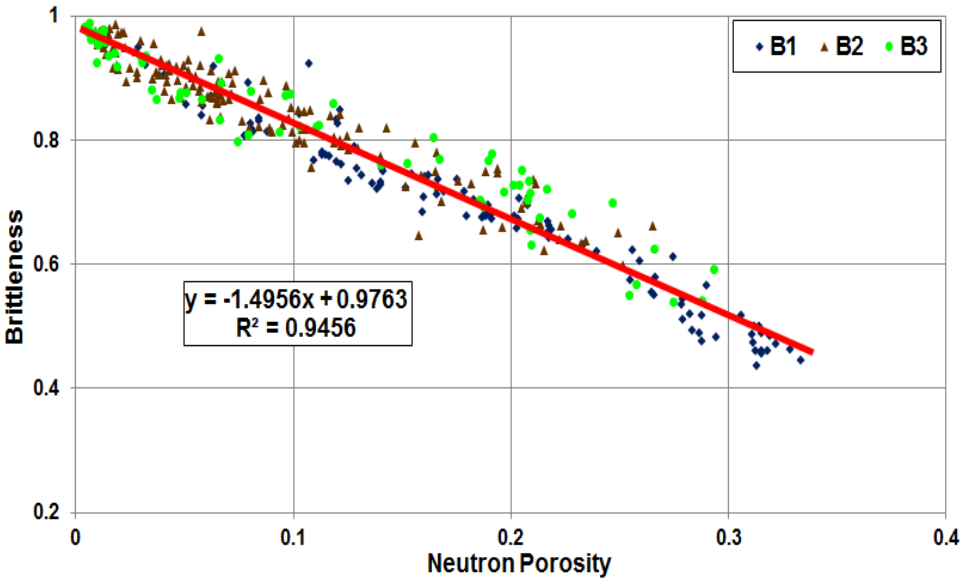

Figure 5.3 Correlation of brittleness with porosity for Barnett shale.

The correlation of brittleness with porosity for Barnett shale is

$$B_{24} = -1.4956 \times \phi + 0.9763$$
$$R^2 = 0.9456 \tag{5.6}$$

5.3.3 Correlation of Brittleness with Porosity for Eagle Ford Shale

Eagle Ford shale is a late Cretaceous-age shale located in south Texas with thickness ranges from ~100 to ~300 ft. The burial depth varies from ~4,000 ft to ~14,000 ft. It can be divided into the Upper and Lower Eagle Ford, and the Upper Eagle Ford is thicker than the Lower Eagle Ford. It is bounded by the Austin Chalk above and Buda formation below. Both gas and oil are produced in Eagle Ford Shale, but only gas play is studied here. The high fraction of carbonate in shale makes it brittle and a good fracturing candidate [*Inamdar et al.*, 2010]. Well logging data from five wells of Eagle Ford shale are selected for developing the correlation between mineralogical brittleness and neutron porosity, and are plotted in Fig. 5.4.

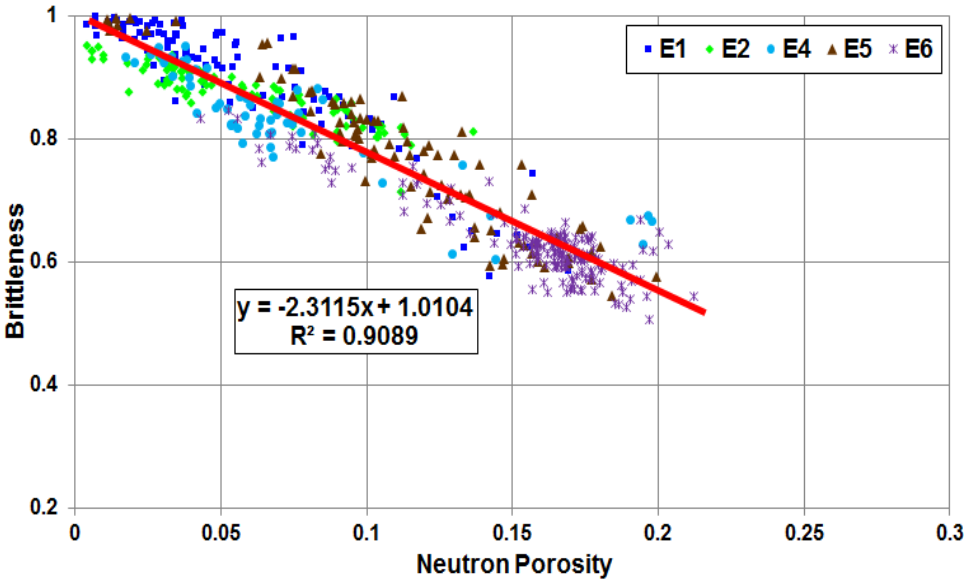

Figure 5.4 Correlation of brittleness with porosity for Eagle Ford shale.

The correlation of brittleness with porosity for Eagle ford shale is

$$B_{25} = -2.3115 \times \phi + 1.0104 \qquad R^2 = 0.9089 \tag{5.7}$$

5.4 Prediction of Brittleness with Compressional Sonic Slowness for Typical Shale Reservoirs

The equation for B_{19} is derived with density, compressional, and secondary slowness [*Rickman et al.*, 2008], and tracks of B_{19} and B_{22} are similar (Fig. 5.1). In addition, the association of mineralogical brittleness with porosity is proven in section 5.3, and porosity can be correlated with compressional slowness [*Mavko, Mukerji and Dvorkin*, 2009]. Therefore, B_{22} might be correlated with density, compressional, and shear slowness. However, after examining the cross plots of mineralogical brittleness with density, compressional and secondary slowness, it is found that only compressional sonic slowness is correlated well with mineralogical brittleness. Therefore, three correlations of mineralogical brittleness with compressional slowness are also developed for Woodford, Barnett, and Eagle Ford shales and are presented in the following.

5.4.1 Correlation of Brittleness with Compressional Sonic Slowness for Woodford Shale

Well logging data shown in Fig. 5.5 from two wells of Woodford shale are selected for the correlation between mineralogical brittleness and compressional slowness (*DTC*). The correlation is as follows:

$$B_{26} = -0.012 \times DTC + 1.4921 \qquad R^2 = 0.4164 \tag{5.8}$$

Brittleness B_{26} is not good in terms of low R^2 value, but shows a linear trend. In order to improve the quality of B_{26}, one needs additional data from more wells in Woodford shale. Unfortunately, not many wells have both mineralogical and sonic logs.

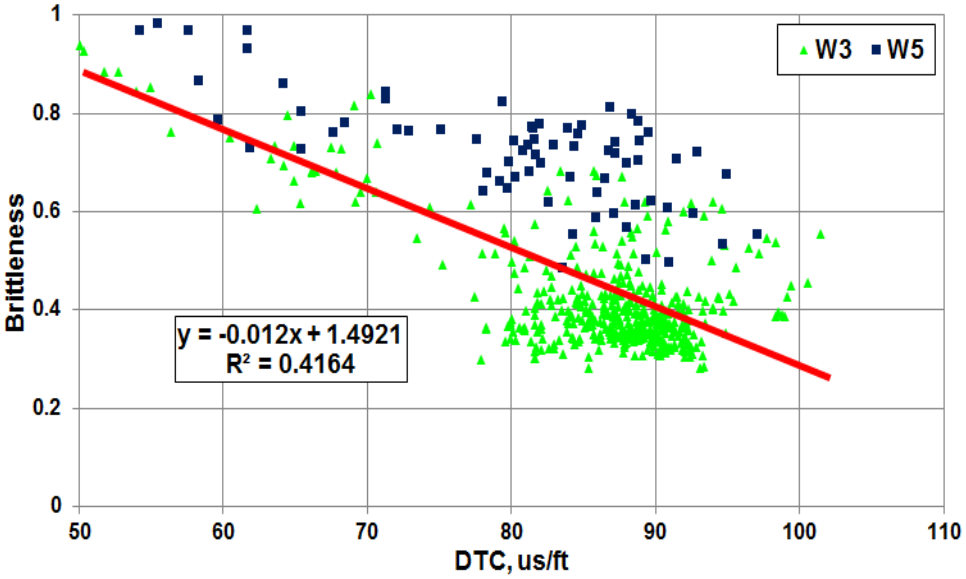

Figure 5.5 Correlation of brittleness with compressional slowness for Woodford shale.

5.4.2 *Correlation of Brittleness with Compressional Sonic Slowness for Barnett Shale*

Well logging data from three wells of Barnett shale were selected for developing the correlation between mineralogical brittleness and *DTC*, and are plotted in Fig. 5.6. The correlation is as follows:

$$B_{27} = -0.0104 \times DTC + 1.4941 \qquad R^2 = 0.9156 \tag{5.9}$$

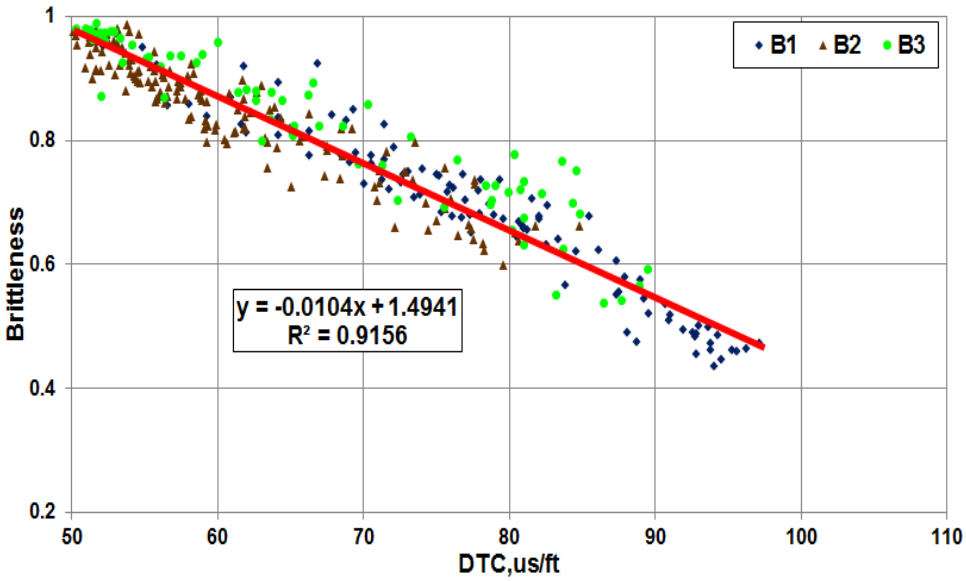

Figure 5.6 Correlation of brittleness with compressional slowness for Barnett shale.

5.4.3 Correlation of Brittleness with Porosity for Eagle ford Shale

Well logging data from five wells of Eagle Ford shale were selected for exploring the correlation between mineralogical brittleness and *DTC*, and are plotted in Fig. 5.7.

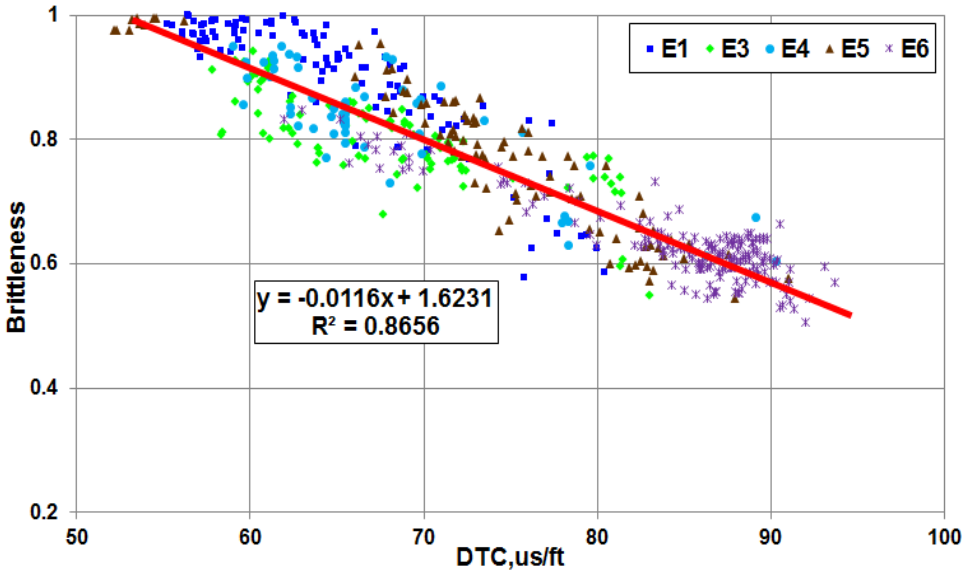

Figure 5.7 Correlation of brittleness with *DTC* for Eagle Ford shale.

The correlation is as follows:

$$B_{28} = -0.0116 \times DTC + 1.6231 \qquad R^2 = 0.8656 \tag{5.10}$$

5.5 Global Correlations of Brittleness with Porosity and Compressional Slowness

From the analysis, it is concluded that mineralogical brittleness can be linearly correlated with neutron porosity and compressional slowness for Woodford, Barnett, and Eagle Ford Shales. It might be valuable and possible to develop a global correlation between mineralogical brittleness and compressional slowness, mineralogical brittleness and neutron porosity by integrating data from the three plays.

5.5.1 Global Correlation of Brittleness with Porosity

Mineralogical brittleness and neutron porosity data from 12 wells of Woodford, Barnett, and Eagle Ford shales are selected for the development of a global correlation between mineralogical brittleness and porosity. The data are plotted in Fig. 5.8. The developed correlation is as follows:

$$B_{29} = -1.8748 \times \phi + 0.9679 \qquad R^2 = 0.9048 \tag{5.11}$$

The trend in Fig. 5.8 proves that the correlation between brittleness and neutron porosity is a global relation for all shale reservoirs. For other shale plays not being studied here, such as Marcellus, Haynesville, Fayetteville shale, etc., one may develop similar correlations of brittleness with available data, or use B_{29} to conduct a qualitative evaluation.

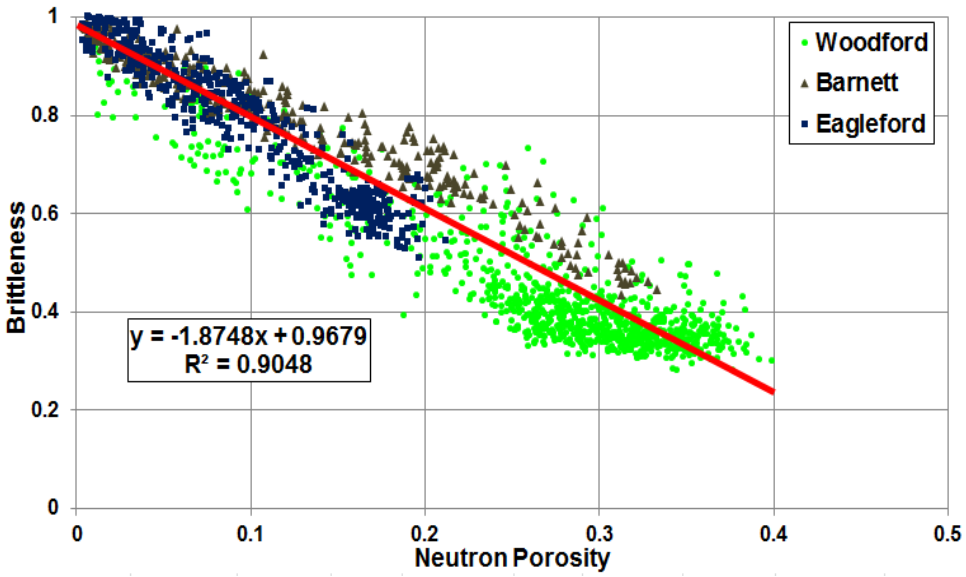

Figure 5.8 Correlation of brittleness with porosity for Woodford, Barnett and Eagle ford shales

5.5.2 Global Correlation of Brittleness with Sonic Compressional Slowness

Mineralogical brittleness and *DTC* data from all 10 wells of Woodford, Barnett, and Eagle Ford shales are selected for the correlation and are plotted in Fig. 5.9. The correlation is as follows:

$$B_{30} = -0.0142 \times DTC + 1.7439 \qquad R^2 = 0.7433 \tag{5.12}$$

The correlation given by B_{30} is good, but not as good as B_{29}. It can be observed in Figs. 5.8 and 5.9 that mineralogical brittleness is better correlated with neutron porosity than compressional slowness. The correlation B_{30} is a global correlation that can be applied quantitatively to evaluate brittleness of other shale plays without the need for mineralogical logging data.

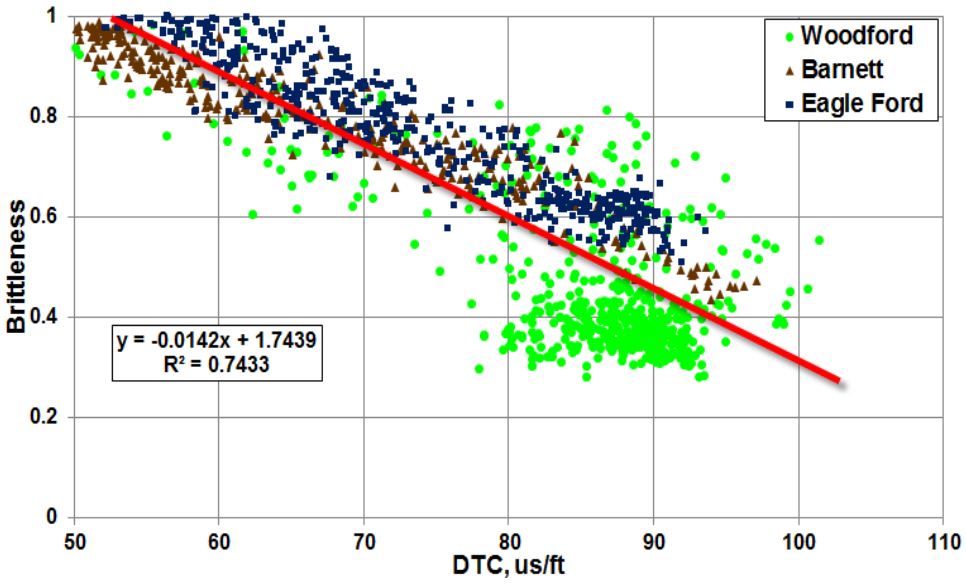

Figure 5.9 Correlation of brittleness with compressional slowness *DTC* for Woodford, Barnett and Eagle ford shales.

The B_{30} correlation can be improved by eliminating Woodford shale data. Employing only the Barnett and Eagle Ford shale data, an improved global correlation of brittleness with *DTC* is developed as shown below:

$$B_{31} = -0.0108 \times DTC + 1.5435 \qquad R^2 = 0.8578 \tag{5.13}$$

If one has more logging data from Woodford shale, a better global correlation between brittleness and compressional slowness can be derived.

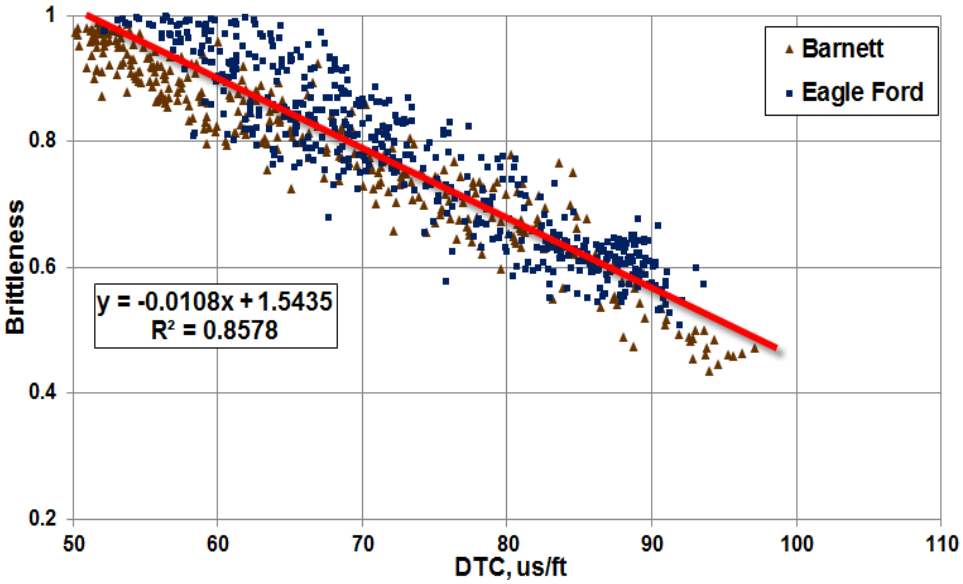

Figure 5.10 Correlation of brittleness with compressional slowness *DTC* for Barnett and Eagle ford shales.

5.6 Field Application and Verification

The brittleness correlations developed here are independently verified with the data from wells not included in the analysis.

Case I: Predicting brittleness with neutron porosity in Barnett shale.

The data from Well A of Barnett shale is shown in Fig. 5.11. Local brittleness B_{24} and global brittleness B_{29} are calculated, and compared against mineralogical brittleness B_{22}. The results indicate that both B_{24} and B_{29} can predict brittleness in Barnett shale equally well but B_{29} is slightly better, because B_{29} is closer to B_{22}. The tracks of *GR* (gamma ray), *CAL* (caliper), and *RT* (true resistivity) are also included to verify the interpretation of results.

Case II: Predicting brittleness with compressional slowness in Barnett shale.

The data from Well B of Barnett shale is shown in Fig. 5.12. Local brittleness B_{27} and global brittleness B_{30} are calculated, and compared against mineralogical

brittleness B_{22}. The results indicate that both B_{27} and B_{30} can predict brittleness in Barnett shale equally. The tracks of *GR*, *CAL*, and *RT* are also included to verify the interpretation of results.

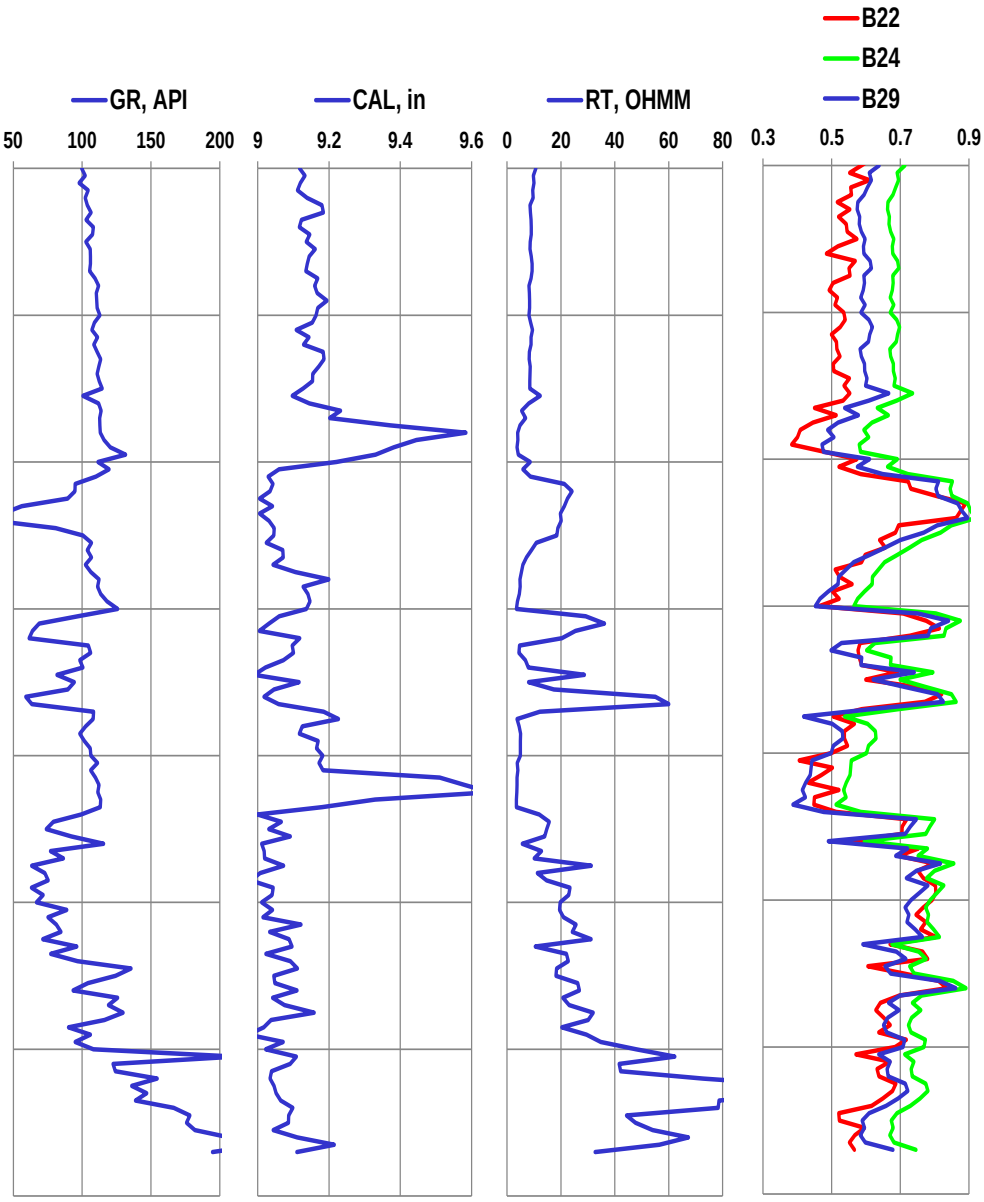

Figure 5.11 Prediction of brittleness with local correlation (B_{24}) and global correlation (B_{29}) for Well A of Barnett shale.

*The major unit in vertical direction is 100 ft.

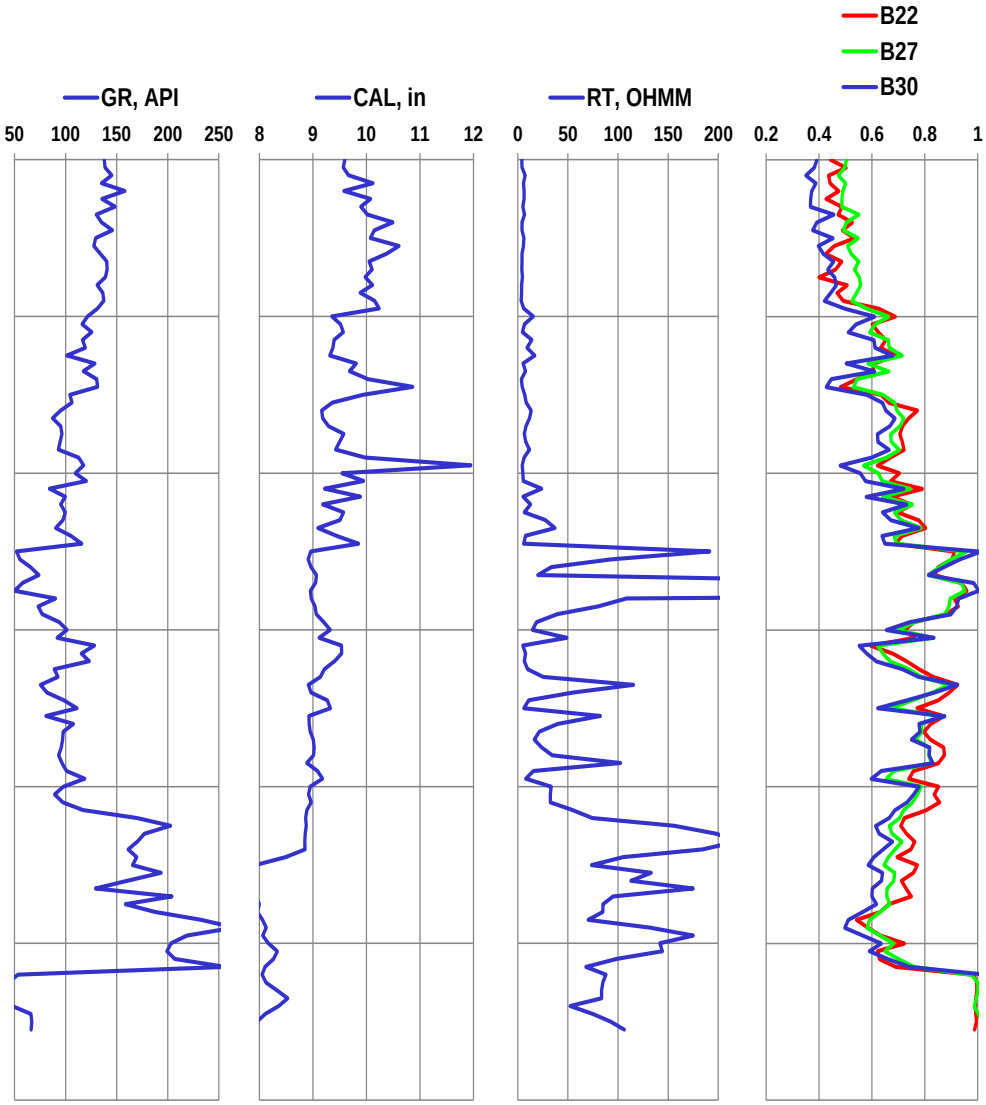

Figure 5.12 Prediction of brittleness with local correlation (B_{27}) and global correlation (B_{30}) for Well B of Barnett shale.

*****The major unit in vertical direction is 100 ft.

5.7 Discussion and Conclusions

The mineralogical brittleness is redefined as B_{22}, which consists of silicate minerals (quartz, feldspar, and mica), and carbonate minerals (mainly dolomite and calcite). The new definition of mineralogical brittleness is proven with two independent

definitions of brittleness: B_{18} (sinusoidal function of internal friction angle) and B_{19} (modified from Rickman's brittleness based on dynamic Young's modulus and Poisson's ratio). The parallel comparison of B_{22} with B_{18} and B_{19} benchmarks the definition of brittleness B_{22}. The application of B_{22} and B_{19} is restricted due to the expense and lack of logging data. Shale specific correlations between (1) mineralogical brittleness and neutron porosity, and (2) mineralogical brittleness and compressional sonic slowness have been developed for the Woodford, Barnett, and Eagle Ford shales. Two global correlations between (1) mineralogical brittleness and neutron porosity, and (2) mineralogical brittleness and compressive slowness have been developed by integrating the data from all three plays, for example, Woodford, Barnett, and Eagle Ford shales. The correlations have been verified against mineralogical brittleness of two independent wells from Barnett shale. The applicability and validity of the empirically derived correlations is reasonably good for evaluating rock brittleness; however, further research and enhanced database is essential to increase their accuracy.

Generally, it is considered that high Gamma Ray value corresponds to high clay content and low brittleness, but this is not universally true. Mineralogical brittleness B_{22} is the essence of brittleness with strong physical ground. Attempts are made to develop correlation between B_{22} and gamma ray, but without success. It will also be valuable to compare mineralogical brittleness with internal friction angle measured by Mohr-Coulomb experiments in laboratory.

One should be aware that the shortcomings of brittleness alone as a fracture indicator. Chapter 6 will integrate both brittleness and fracture energy (or fracture toughness) for the screening of fracturing candidates and barriers.

Chapter 6. Fracability Evaluation in Shale Reservoirs - An Integrated Petrophysics and Geomechanics Approach

6.1 Introduction

Brittleness has been applied to evaluate drillability in drilling [*Yarali and Kahraman*, 2011], sawability in rock cutting [*Gunaydin, Kahraman and Fener*, 2004], and mechanical coal mining [*Singh*, 1986]. In recent years, brittleness has been used as a descriptor in screening hydraulic fracturing candidates [*Jarvie et al.*, 2007; *Rickman et al.*, 2008; *Wang and Gale*, 2009; *Chong et al.*, 2010; *Li et al.*, 2013]. Therefore, brittleness is one of the most important petrophysical properties, and has been included in most petrophysics reports of unconventional shale reservoirs. The definition of brittleness was benchmarked in Chapter 5. A table of selected definitions of brittleness is assembled in Table 5.1. It is assumed that formation with high brittleness is easy to fracture [*Rickman et al.*, 2008; *Kundert and Mullen*, 2009; *Alassi et al.*, 2011; *Slatt and Abousleiman*, 2011], but this assumption is not always true because formation with higher brittleness can be a fracture barrier. For instance, dolomitic limestone is brittle, but it is a fracture barrier in Barnett shale because fracture gradient in shale formation is lower than in dolomitic limestone formation, and it cannot be fractured at the same pressure [*Bruner and Smosna*, 2011]. Therefore, brittleness alone is not sufficient to characterize the fracability of unconventional shale reservoirs. Brittleness is also applied to evaluate rock cutting efficiency, and it is found that the implementation of a single brittleness concept is not sufficient for the evaluation, specific energy should also be taken into account [*Göktan*, 1991]. Similarly, in hydraulic fracturing, other parameters similar to specific energy should be included to improve the formation fracability evaluation [*Altindag*, 2010].

In view of the above fact, this chapter attempts to solve the following problems: (1) develop a fracability evaluation model by integrating brittleness and other parameters, such as fracture toughness, energy dissipation during hydraulic fracturing, and so on; (2) apply the new model to evaluate fracability of shale reservoir, verify the interpretation results by geological interpretation, and identify its advantages by comparing against methods that use only brittleness or Poisson's ratio.

6.2 Fracture Toughness and Strain Energy Release Rate

6.2.1 Fracture Toughness

SIF (stress intensity factor) is a parameter used in fracture mechanics to predict the stress state in the vicinity of crack tip caused by remote loading or residual stress [*Rice*, 1968a]. Upon *SIF* reaching its critical value, which is defined as fracture toughness, rock will be fractured [*Bower*, 2011]. Fracture toughness represents the resistance of rock to fracture propagation from preexisting cracks. It has been proven that higher the fracture toughness, higher is the breakdown pressure [*Jin et al.*, 2013]. Fracture toughness is a material property, and can be measured with various methods. The popular measurement methods are listed in the following:

- Chevron Notched Short Rod (CNSR) Method [*Bubsey et al.*, 1982]
- Chevron Notched Semicircular Bend (CNSCB) Method [*Chong and Kuruppu*, 1984]
- Chevron Notched Brazil Disk (CNBD) Method [*Zhao and Roegiers*, 1993]

Fracture toughness measurement of rock is more difficult and complex than other tests of rock mechanical properties. To reduce the turnaround time and save expense, correlations of fracture toughness with Young's modulus, Poisson's ratio,

hardness, tensile strength, uniaxial compressive strength, and velocity of primary acoustic wave have been derived from experimental data of different types of rocks [*Barry, Whittaker and Singh*, 1992]. In addition, fracture toughness, tensile strength, and acoustic velocity are measured on samples of Woodford shale [*Sierra et al.*, 2010]. The laboratory data of Woodford shale in the literature were taken to verify the accuracy of the existing correlations in predicting fracture toughness of shale. The comparison results are included in Table 6.1.

Table 6.1 Error analysis of correlations for fracture toughness

Equation Number	**Correlation of Fracture Toughness**	**Coefficient of Determination R^2**	**Error between Predicted and Measured K_{IC}**
1	$K_{IC} = 0.271 + 0.107 \times \sigma_t$	0.86	12.47%
2	$K_{IC} = 0.313 + 0.027 \times E$	0.62	23.82%
3	$K_{IC} = -1.68 + 0.65 \times V_p$	0.90	491.78%
4	$K_{IC} = 0.708 + 0.006 \times \sigma_c$	0.72	No measured data

In Table 6.1, K_{IC} is mode-I fracture toughness, MPa·m$^{0.5}$; σ_t and σ_c are tensile strength and uniaxial compressive strength, MPa; E is Young's modulus, GPa; V_p is compressional sonic velocity, m/sec.

Although the values of R^2 for the four correlations in Table 6.1 are high, the errors vary when comparing predicted fracture toughness with measured values. The first two correlations in Table 6.1 show positive potential in evaluating fracture toughness of shale reservoirs because of the smaller errors. However, error of the correlation with V_p is large, although its R^2 is high. To further improve the accuracy in predicting fracture toughness, expanding experimental data are required. It is more

valuable to derive fracture toughness from logging data with correlations of small errors, and tie the value to core data.

From the above analysis, it is found that fracture toughness can be linearly correlated with Young's modulus or tensile strength. Both Young's modulus and tensile strength are anisotropic in vertical and horizontal directions [*Jaeger, Cook and Zimmerman*, 2009], as shown in Fig. 6.1. Therefore, fracture toughness is also an anisotropy property. Its value parallel to the bedding (Fig. 6.1-B) plane is higher than perpendicular to the bedding plane (Fig. 6.1-A). It was concluded that anisotropy of rock fracture toughness mainly depends on the size and orientation of microstructural features [*Nasseri and Mohanty*, 2008]. Unconventional shale formations are rich in natural fracture, the degree of fabric anisotropy and material composition are different at different locations [*Sone*, 2012], so fracture toughness anisotropy is significant in shale reservoirs. Unfortunately, little research is conducted to study the effect of fracture toughness anisotropy on hydraulic fracturing [*Chandler, Meredith and Crawford*, 2013].

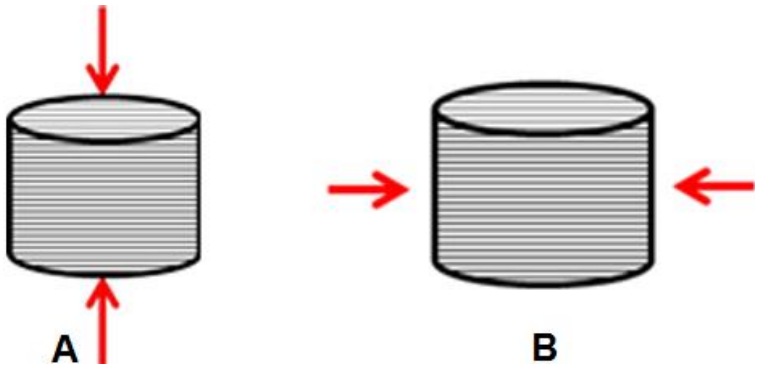

Figure 6.1 Demonstration of anisotropy of rock mechanics property.

6.2.2 Strain Energy Release Rate

Strain energy release rate is the energy dissipation per unit surface area during the process of new fracture creation [*Barry, Whittaker and Singh*, 1992]. According to failure criterion, when strain energy release rate reaches its critical value, G_C (G_C is named as fracture energy), fracture propagates from the preexisting fracture. In hydraulic fracturing, fracture surface area (fracture length multiplied by fracture height) is far larger than the cross section area (fracture height multiplied by fracture width), so most energy is consumed in the creation of new fracture surface area. It is assumed that: given the same amount of energy, lower the G_C, more fracture surface area will be created. The critical value, G_C is independent of the applied load and the geometry of the body [*Irwin*, 1957]. In present study, G_C is assumed not to vary with fracture modes. The critical strain energy release rate is

$$G_C = \frac{K_{IC}^2}{E'} \tag{6.1}$$

where, $E' = E$ for plane stress, and $E' = E/(1-\nu^2)$ for plane strain.

For hydraulic fracturing in an infinite subsurface body, the assumption of plane strain is applied. Substituting the correlation of fracture toughness with Young's modulus from Table 1 into Eq. 6.1 lead to the following

$$G_C = (1-\nu^2)\frac{(0.313+0.027\times E)^2}{E}\times 10^3 \tag{6.2}$$

keeping Poisson's ratio ν as constant, varying Young's modulus E, and analyzing the variation of G_C with E, it is observed that minimum G_C is 30.8 $(1-\nu^2)$ Joule/m^2 when E = 11.59 GPa, G_C decreases with increasing E when E < 11.59 GPa, , but increases with increasing E when E > 11.59 GPa. Considering the uncertainty in the

coefficients of fracture toughness correlations of Table 6.1, the boundary value 11.59 is not an exact number, and it may be slightly higher or lower than 11.59. Based on the analysis, it is concluded that the fracture energy does not always increase with increasing Young's modulus. However, because Young's modulus of most sedimentary rocks is greater than 11 GPa, it can be stated that formation with higher Young's modulus will be more difficult to fracture. Since fracture toughness is linearly correlated with Young's modulus, higher the fracture toughness, more energy will be dissipated during the creation of new fracture surfaces.

6.3 Fracture Barrier

One of the key steps to successful hydraulic fracturing is the identification of fracture barrier [*Economides and Nolte*, 2000]. Hydraulic fracture should be contained within the pay zone, unintentional invasion into freshwater aquifer or fault zone will adversely affect future hydrocarbon production or lead to environmental pollution [*Bruner and Smosna*, 2011]. For instance, Barnett shale is underlain by the Ellenburger formation, which is composed of porous dolomite and limestone often bearing water. Fracture breakthrough in the aquifer will reduce relative permeability of gas, and finally, reduce the net present value of the play [*Bruner and Smosna*, 2011]. In addition, the prediction of fracture height is determined by the estimation of fracture barrier depth, which is contingent upon fundamental understanding of the mechanisms of fracture barrier to vertical fracture propagation. Misinterpretation of fracture barrier may also influence the calculation of fracture length and width [*Gidley*, 1989]. The schematic of fracture barrier is demonstrated in Fig. 6.2.

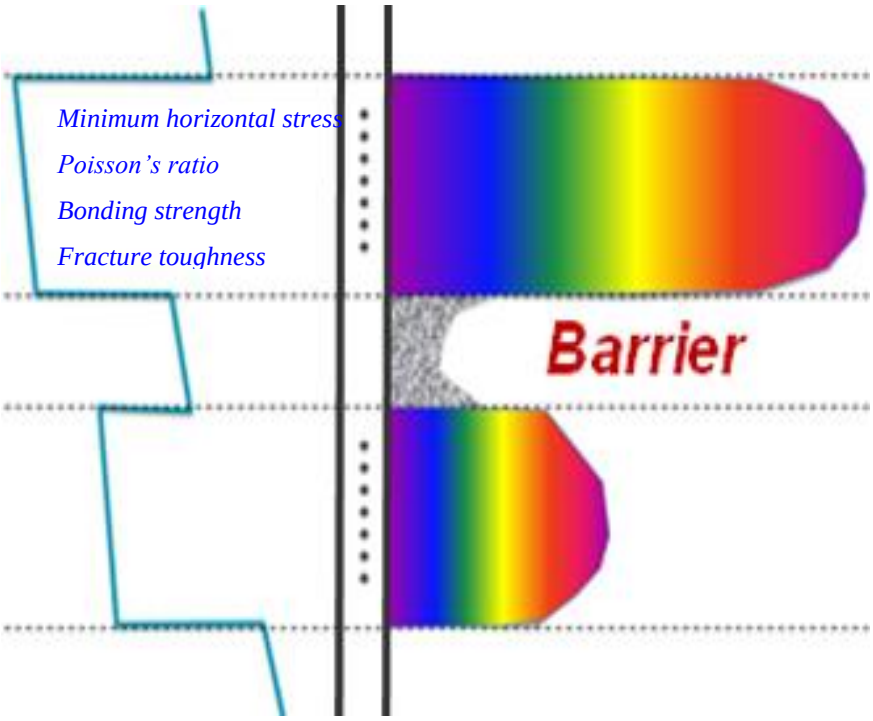

Figure 6.2 Schematic of fracture barrier.

In general, the following factors are considered as an indication of fracture barrier [*Simonson, Abou-Sayed and Clifton*, 1978; *Ham*, 1982; *Economides and Nolte*, 2000]:

- ***Minimum horizontal in-situ stress***: higher minimum horizontal in-situ stress corresponds to higher closure stress;
- ***Poisson's ratio***: If it is not in active tectonic stress area, higher Poisson's ratio corresponds to higher minimum horizontal in-situ stress, which is a fracture barrier;
- ***Fracture toughness***: higher fracture toughness (only considers mode-I K_{IC}) corresponds to higher breakdown pressure. Higher fracture gradient will be needed to fracture formation with higher fracture toughness;
- ***Brittleness***: relatively less brittle formation exhibits plasticity and fracturing in plastic formation consumes more energy;

- ***Shear bond strength at the interface***: slippage at the interface may stop fracture penetration into the adjacent formation.

6.4 Fracability Index Model

The objective of hydraulic fracturing in shale reservoirs is: (1) to create and connect complex fracture network; and (2) to maximize stimulated reservoir volume (*SRV*). To create and connect the complex fracture network, the candidate should have relatively high brittleness. To maximize *SRV*, the energy required to create a new fracture surface should be relatively low. Therefore, an ideal hydraulic fracturing candidate is of relatively high brittleness and low critical strain energy release rate. The mathematical model of fracability index (*FI*) is defined as follows:

$$FI_1 = w \times B_n + (1-w) \times G_{C_n} \tag{6.3}$$

where, w is weight fraction ($0 < w < 1.0$), B_n and G_{C_n} are normalized brittleness and critical strain energy release rate, and are defined as:

$$B_n = \frac{B - B_{\min}}{B_{\max} - B_{\min}} \tag{6.4}$$

$$G_{C_n} = \frac{G_{C_\max} - G_C}{G_{C_\max} - G_{C_\min}} \tag{6.5}$$

where, B_{min} and B_{max} are the minimum and maximum brittleness and G_{C_min} and G_{C_max} are the minimum and maximum critical strain energy release rates for the investigated formation.

According to the analysis in Section 6.2.2, for most sedimentary rocks, G_C increases monotonically with Young's modulus and fracture toughness. Therefore, it is appropriate to define fracability index with Young's modulus and fracture toughness.

The mathematical model of fracability index in terms of brittleness and fracture toughness can be defined as follows:

$$FI_2 = w \times B_n + (1-w) \times K_{IC_n} \tag{6.6}$$

where, w is weight fraction ($0 < w < 1.0$), B_n is normalized brittleness (Eq. 6.4), and K_{IC_n} is normalized fracture toughness as defined below:

$$K_{IC_n} = \frac{K_{IC_\max} - K_{IC}}{K_{IC_\max} - K_{IC_\min}} \tag{6.7}$$

where, $K_{IC_\min}$ and $K_{IC_\max}$ are the minimum and maximum mode-I fracture toughness for the investigated formation, respectively.

The mathematical model of fracability index in terms of brittleness and Young's modulus is defined as:

$$FI_3 = w \times B_n + (1-w) E_n \tag{6.8}$$

where, w is weight fraction ($0 < w < 1.0$), B_n is normalized brittleness (Eq. 6.4), and E_n is normalized Young's modulus.

$$E_n = \frac{E_{\max} - E}{E_{\max} - E_{\min}} \tag{6.9}$$

where, $E_{\min}$ and $E_{\max}$ are the minimum and maximum Young's modulus for the investigated formation, respectively.

It is known that brittleness can be calculated with dynamic Young's modulus and Poisson's ratio. The in-house verifications also prove that the three proven brittlenesses in Chapter 5 can be applied in fracability index model, and generate similar fracability index maps. To avoid the dispute that fracability index model is a mathematical game of brittleness and rock mechanical properties, only the

mineralogical brittleness is employed in the fracability index model. It is assumed that mineralogical brittleness is independent of rock mechanical properties, such as Young's modulus, tensile strength, fracture toughness, and so on. There are correlations between brittleness and minerals, but the relationships are not unique. Therefore, the fracability index model is not a mathematical game.

Fracability index FI_1, FI_2 and FI_3 are in the range of 0 to 1.0. Formation with $FI = 1.0$ is the best as fracture candidate, and formation with $FI = 0$ is the worst as fracture candidate, and can be a perfect fracture barrier. In present analysis, the weight fraction is set as 0.5. According to results of present research, it is defined that formation with $FI > 0.67$ might be good fracturing candidate (0.67 is bound value). It is hard to determine how much the weight fraction is, but it does not affect the geometry of fracability index curve, only affects the bound value. For instance, if weight fraction $w \neq 0.5$, the bound value of FI might change to one value higher or lower than 0.67. Therefore, it is not important what weight fraction the user chooses, but one must define the bound value by comparing FI curve with other logging data, geological interpretation results, production data, and so on. In the dissertation, weight fraction is set as 0.5.

Fracability index maps (Figs. 6.3 through 6.6) are plotted with mineralogical brittleness and critical strain energy release rate G_C, fracture toughness K_{IC}, and Young's modulus E. It is concluded that: (1) fracture toughness and Young's modulus can be substitutes for critical strain energy in FI calculation, because they show the same trend; (2) formation with brittleness close to 1.0 may not be a good fracturing candidate because its Young's modulus/fracture toughness may be higher, which can

lead to lower *FI*. Limestone formation is one example; (3) formation with lower Young's modulus/fracture toughness may not be a good candidate, because its brittleness may be lower, which can prohibit the formation of connected complex fracture network and thus lower *FI*. Formation rich in clay is one example for this case. (4) Formations with relatively high brittleness and low rock strength show relatively higher *FI*. Shale formation rich in brittleness minerals is one example.

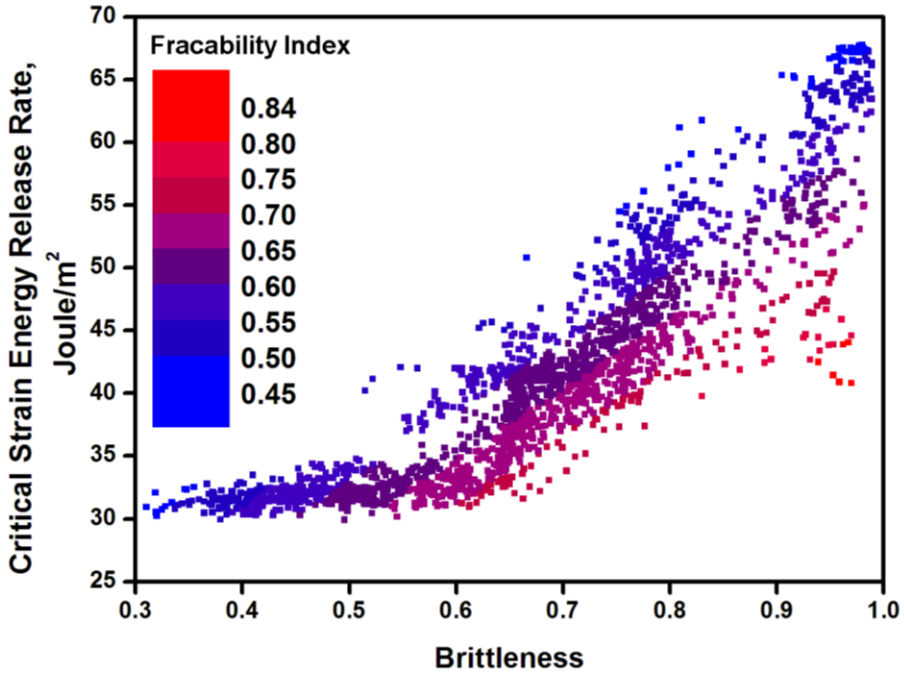

Figure 6.3 A cross plot of brittleness and critical strain energy release rate shows increasing fracability index.

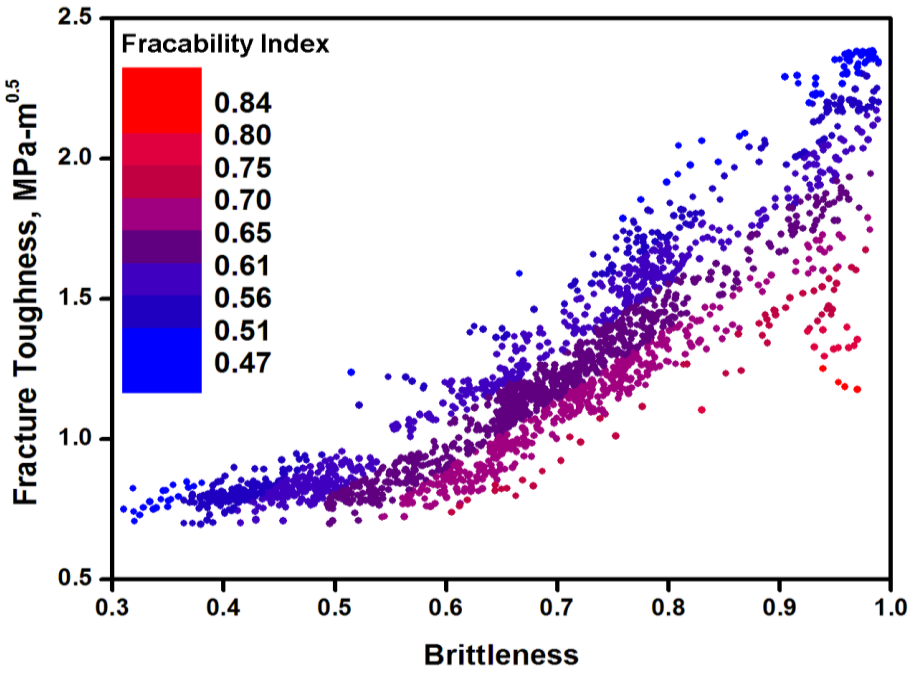

Figure 6.4 A cross plot of brittleness and fracture toughness shows increasing fracability index.

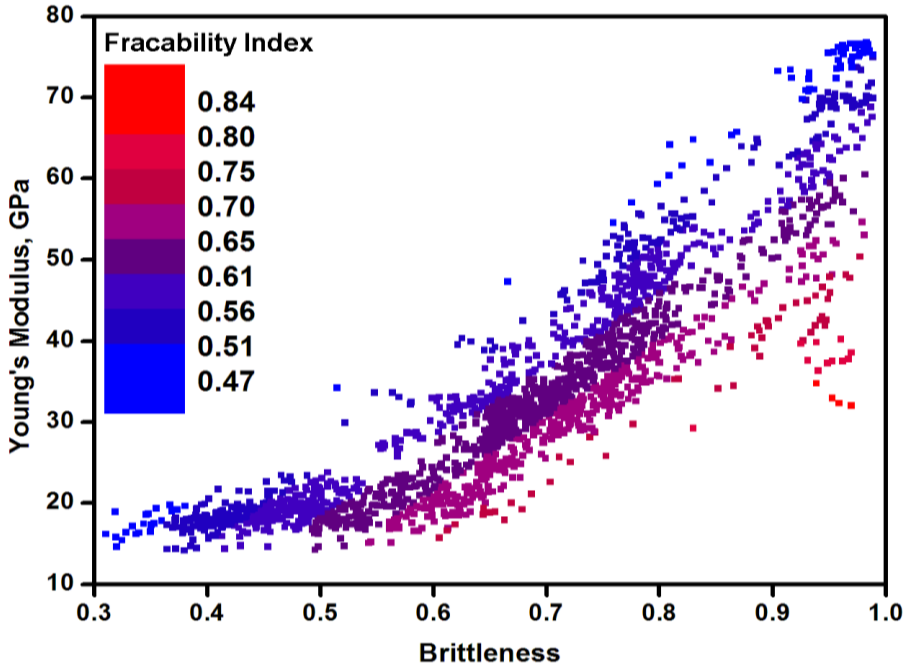

Figure 6.5 A cross plot of brittleness and Young's modulus shows increasing fracability index.

6.5 Field Application

The objective of hydraulic fracturing design is to maximize ultimate hydrocarbon recovery by screening candidates of the highest fracability. The fracability index model developed here is applied to the selection process of hydraulic fracturing candidate with logging data of Well-A in Barnett Shale. The procedure is as follows:

Step 1: Locate pay zones and distinguish rock types by analyzing logging data of Well-A with *GR* (gamma ray)[5], *NPHI* (neutron porosity)[6], *AT90* (deep resistivity at 90 inches)[7], *PEF* (photoelectric factor)[8], *DTC* and *DTS* (compressional and shear slowness)[9], and bulk density (*RHOB*)[10];

Step 2: Calculate dynamic Young's modulus (E), dynamic Poisson's ratio (v), fracture toughness (K_{IC}), mineralogical brittleness (B_{22}), fracability index (FI_1, FI_2, *or* FI_3), and plot their tracks;

Step 3: Locate fracture barrier by comparing *FI* in adjacent formations, and compare the optimized intervals of fracture barriers with interpretation results from Step 1;

Step 4: Screen hydraulic fracturing candidates of higher *FI* within the pay zones;

Step 5: Place horizontal well in the middle of each target, or at the depth that is good for connecting different targets adjacent to thin fracture barriers.

---

[5] *GR* of fracture barrier is relatively lower.

[6] Pay zone of shale gas is of relatively lower value of *NPHI* than that of adjacent formations due to the presence of gas.

[7] Tight limestone is of relatively higher resistivity.

[8] *PEF* is great for distinguishing rock types. Sandstone: ~1.8 to 3.0; limestone: ~4.0 to 5.0; dolomite: ~ 3.0; "Normal" shale: ~3.4; Siliceous shale: 2.5 to 3.0. There are serious errors if the tool is not calibrated correctly.

[9] Sonic slowness is lower in limestone, and higher in pay zones.

[10] *RHOB* of fracture barrier is higher than adjacent formations.

As for the field development plan, it will be helpful to have a 3-D geological model of fracability index, but it is not constructed here due to the absence of logging data covering a field. It will assist the geomodeler/engineer refine the horizontal well trajectory within the pay zone, and optimize the locations and intervals of perforation clusters.

Following the above procedure, according to logging interpretation (mainly based on *NPHI*, *PEF*, *AT90*, and *GR*), Data of Well A from Barnett shale play is employed to illustrate how to refine the trajectory of horizontal drilling and location of hydraulic fracturing in Fig. 6.6. The pay and non-productive zones are represented by yellow and blue colors, respectively. The red shaded sections are hydraulic fracturing candidates; yellow double arrows represent fracture barriers. The brittleness is mineralogical brittleness, and the fracability index track is derived with Eq. 6.6. Logging data of Well-A shown in Fig. 6.6 are interpreted as follows:

(1) Marble Falls, Upper Barnett, Forestburg Limestone, Lower Barnett, and Viola Limestone are distinguished by following step 1.

(2) The viewpoint that hydraulic fracturing candidate is the formation of higher brittleness might not be always true. For instance, brittleness of Bar_3 is higher than the adjacent formations, but *FI* of Bar_3 is lower than that of the adjacent formations due to the higher fracture toughness. According to lithology interpretation, Bar_3 is Forestburg limestone, which can act as barrier if it is thick enough and there are not many natural fractures within it [*Bruner and Smosna*, 2011].

(3) *FI* does not always increase monotonically with increasing brittleness. For instance, different trends of brittleness and *FI* are observed in F_3, F_5, Bar_3, Bar_4, and Bar_6. The reason for the difference is attributed to different trends of fracture toughness.

(4) F_1 through F_5 (the red shaded sections) are selected as fracturing candidates, and Bar_1 through Bar_6 (the yellow double arrows) are considered as fracture barriers by comparing *FI* of adjacent formations. For well-A, when *FI* is greater than 0.7, it is considered as fracturing candidate, otherwise, it is not.

(5) Bar_6 based on *FI* is thicker than Viola limestone shown in blue shaded section, which is interpreted by geologist. Bar_6 is considered as a fracture barrier because its *FI* is much lower than that of F_5, which is attributed to lower brittleness. Complex connected fracture network cannot be easily created in formation with lower brittleness.

(6) Whether a formation can act as fracture barrier depends on: differences of *FI* in the adjacent formations and thickness of fracture barrier. Bar_1 can be an effective barrier in vertical direction because the difference of *FI* between Bar_1 and F_1 is large, and Bar_1 is 200 ft thick. Bar_2, Bar_4 and Bar_5 might not stop hydraulic fracture from crossing because they are thin. Bar_6 is a good fracture barrier because it is 150 ft thick, and the difference of *FI* between F_5 and Bar_6 is large enough.

(7) Hydraulic fracturing may connect upper and lower Barnett through Bar_3 because the difference in *FI* between Bar_3 and its adjacent formation is not large. This viewpoint can also be supported by Poisson's ratio track, which shows that Poisson's ratios are similar in F_2, Bar_3, and F_3.

(8) The viewpoint that the higher (lower) the Poisson's ratio (higher Poisson's ratio corresponds to higher closure stress), lower (higher) is the *FI* is not always true. For lower Barnett and Viola limestone, this is true; however, it is not true for upper Barnett and Marble Falls. The inconsistency is caused by the fact that fracability index model accounts for both mineralogical brittleness and energy dissipation, which makes more sense from physical viewpoint.

In conclusion, fracability index model can help refine traditional formation evaluation.

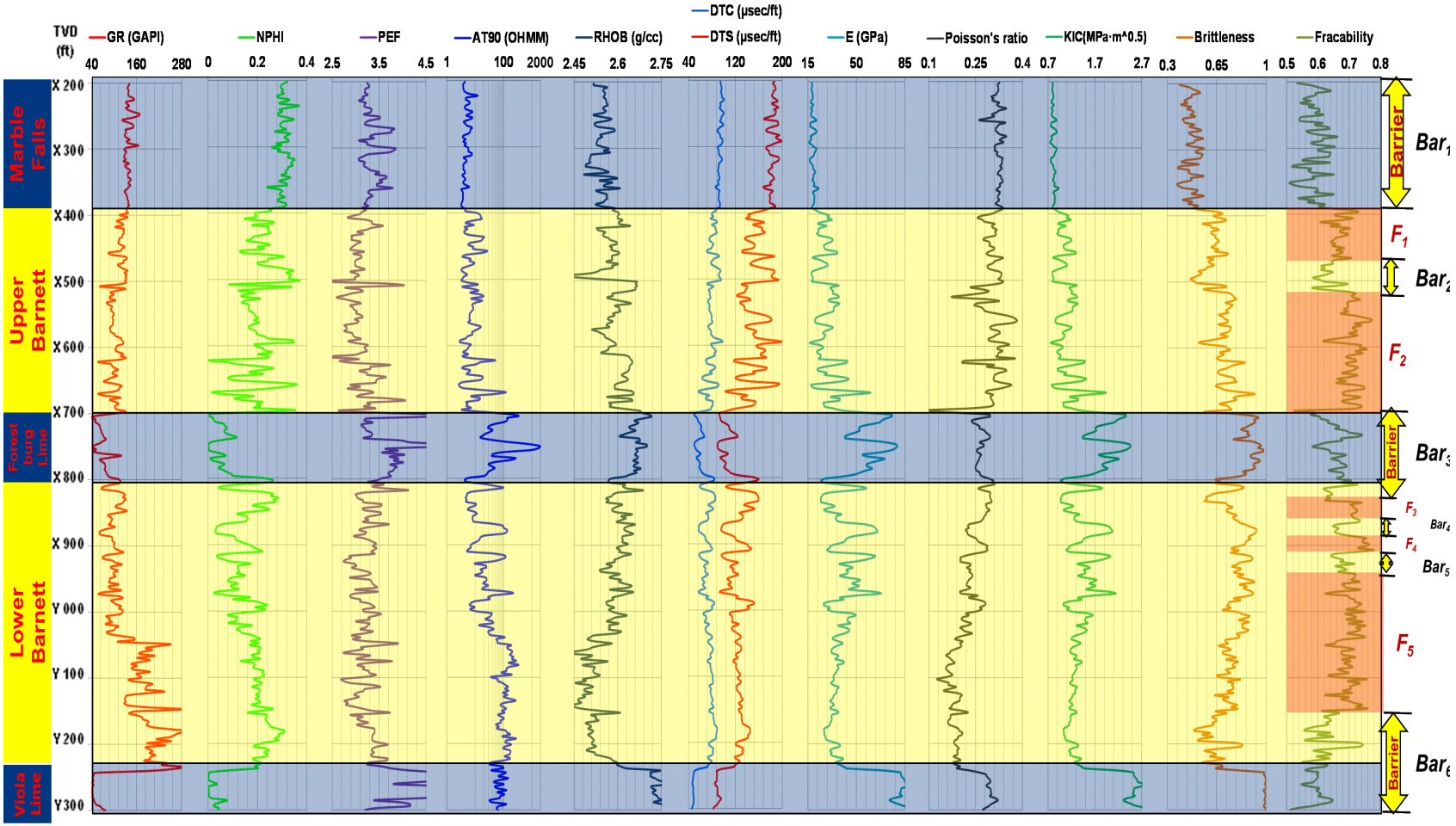

Figure 6.6 Screening hydraulic fracturing candidates with fracability index.

6.6 Discussion and Conclusions

The shortcomings of brittleness as an indicator of fracturing candidate selection are discussed. Fracability index model is developed to overcome the shortcomings by integrating both fracture energy (critical strain energy release rate) and brittleness. For most sedimentary rocks, critical strain energy release rate can be substituted with fracture toughness or Young's modulus in the calculation of fracability index. The objectives of fracability index model are: (1) to screen formations with great potential to create both connected complex fracture network and maximum stimulated reservoir volume; (2) to locate the position of fracture barrier; and (3) to optimize the horizontal well trajectory and perforation cluster spacing. Formation with higher fracability index is considered as good fracturing candidate, whilst others are assigned as fracture barriers. From the cross plots of brittleness and fracture toughness, brittleness and Young's modulus, brittleness and critical strain energy release rate, it is observed that: (1) formation with the highest brittleness (~1.0) may not be a good fracturing candidate because its fracture toughness can also be high, which can lead to lower value of fracability index; (2) formation with relatively lower fracture toughness may not be a good fracturing candidate because its brittleness can also be low, which can lead to lower value of fracability index; (3) formation with relatively lower brittleness may be a good candidate for hydraulic fracturing if its fracture toughness is not very high; (4) formation with relatively higher fracture toughness may be a good fracturing candidate if its brittleness is high enough. The fracability index model is successfully applied to optimize the hydraulic fracturing and horizontal well drilling of Well-A in Barnett shale.

Because tensile strength is also linearly correlated with Young's modulus, fracability index can also be calculated with tensile strength and brittleness. Some readers think fracability index map is a mathematical game, because brittleness can be calculated from Young's modulus and Poisson's ratio. To convince the skeptical readers that it is not a mathematical game, the fracability maps are plotted with mineralogical brittleness. However, it also proves that one can use Rickman's brittleness, or internal friction angle based brittleness to build fracability index model in the absence of mineralogical brittleness. Only opening mode fracture is considered here when developing fracability index model. Mode-II fracture (sliding mode) may also contribute to stimulated reservoir volume, but the reaction of preexisting natural fractures is by the changing of pore pressure, not by fracturing fluid directly, which is different from the reactivation of mode-I fracture. A 3-D fracability index model could be constructed with the method developed in this paper if well logging data from a field is available. It will help user to optimize the trajectory of horizontal well and perforation cluster spacing in multistage hydraulic fracturing. Fracture diagnostic test data will be helpful for further validation of the proposed fracture index model.

Chapter 7. Conclusions and Recommendations

7.1 Conclusions

This dissertation encompasses fundamental rock fracture mechanics and petrophysical studies in hydraulic fracturing. Several selected challenging topics were studied by integrating geomechanical and petrophysical modeling, hydraulic fracturing experiments in laboratory, and logging interpretation. The major discoveries are as follows:

(1) Three criteria (S-Criterion, σ_θ-Criterion, and G-Criterion) yield fracture initiation angles with similar trends but different magnitudes, S-Criterion < σ_θ-Criterion < G-Criterion.

(2) σ_θ-Criterion is the most popular fracture propagation criterion in fracturing simulation, but yields fracture initiation angle that deviates more from measured fracture initiation angle in the laboratory than S-Criterion. Therefore, S-Criterion is the best criterion for fracture propagation simulation.

(3) Weight function method is applied successfully to predict breakdown pressure of preexisting fracture emanating from borehole. The weight function based *SIF* is verified against boundary collocation based *SIF*. The weight function based breakdown pressure is verified against both breakdown pressure of both PSA and Rummel's method, and measured values from both in-house experiments and published experimental data.

(4) The weight function based breakdown pressure accounts for near wellbore stress concentration, nonlinear pressure distribution inside fracture, deviation angle, and dimensionless fracture length. It improves the accuracy of breakdown pressure prediction, and is a more general method than PSA and *Rummel*'s methods.

(5) The definition of brittleness is redefined and benchmarked by the comparison with three independent definitions of brittleness. Correlations of brittleness with compressional sonic slowness and neutron porosity have been developed for Woodford, Barnett, and Eagle Ford Shales. The global correlations can save the cost of expensive mineralogical logging and dipole logging, and enable the prediction of brittleness in fields without such logging services.

(6) Fracability index model is developed by integrating both fracture energy (fracture toughness, Young's modulus, or tensile strength) and brittleness. It overcomes the limitations of brittleness alone as a fracturing indicator. Formation with high fracability index is considered as good fracturing candidate, while others are considered as fracture barriers. The results of fracability index model are proven with results from logging interpretation. The fracability index model can help us refine the interpretation results by traditional method.

7.2 Recommendations

The conclusions mainly depend on results of theoretical models and experiments in the laboratory. The methodologies developed in the dissertation may provide guidelines for drilling and hydraulic fracturing, but direct applications without critical analysis may lead to risks because of the assumptions of linear elasticity, homogeneous material, symmetrical fracture, etc. The following topics are suggested for future research:

(1) Mixed-mode fracture propagation in nonhomogeneous material. Rock is an inhomogeneous material. It is valuable to compare the differences of fracture initiation angles in homogeneous and nonhomogeneous rocks.

(2) The weight function method might be applied to analyze the mechanisms of wellbore strengthening. Preexisting fractures intersecting borehole reduce fracture gradient. Continuum mechanics is not appropriate for predicting breakdown pressure of borehole with fracture, as discussed in Chapter 4.

(3) Weight function parameters of single/multi fractures emanating from borehole can be derived with similar approach proven in Chapter 3. Only weight function parameters of symmetrical radial cracks are derived in the dissertation.

(4) The weight function method can be applied to estimate the magnitude of maximum horizontal in-situ stress and the length of natural fractures intersecting borehole. The modeling of both parameters is still controversial. The weight function method may provide some insights into it.

(5) The benchmarked definition of brittleness can be compared against measured results by rock mechanics experiments. It will be valuable to figure out the differences of brittleness between field and laboratory.

(6) Brittleness cannot only be used in hydraulic fracturing evaluation, but also can be applied to predict the rate of penetration during drilling. The *ROP* data can also tell the users whether the formation is brittle or not. It is significant to have the correlation between *ROP* and brittleness.

(7) The fracability index model can be integrated to hydraulic fracturing model. For example, set different fracability indices for different layers, input the same mechanical properties in simulator, and then study the integrity of fracture barriers.

(8) Hydraulic fracturing data can further prove the validity of fracability index model. For example, one field has a complete set of logging data, and the fracturing job

failed. One might figure out the failure reasons by evaluating its fracability index. The fracturing job might be conducted in a formation with low fracability index, so the fracturing job failed.

Nomenclatures

a = perforation/preexisting fracture depth, m

AT90 = deep resistivity at 90 inches from borehole wall, OHMM

b = stress ratio between maximum and minimum horizontal principal stresses, σ_H/σ_h in Chapter 2; normalized fracture length in Chapter 4, $1 + a/R_w$.

B_i = brittleness index, i is integer number from 1 to n.

B_n = normalized brittleness index defined in Eq. 6.4

B_{max} = maximum brittleness for the investigated formation

B_{min} = minimum brittleness for the investigated formation

BC = boundary collocation

C = stress contrast between maximum and minimum horizontal principal stresses, Mpa

CAL = caliper

CNSR = Chevron Notched Short Rod method

CNSCB = Chevron Notched Semicircular Bend method

CNBD = Chevron Botched Brazil Disk method

DTC = compressional sonic slowness, μs/ft

DTS = shear slowness, μs/ft

E = Young's modulus for plane stress problem, GPa

E' = general expression of Young's modulus, it is different for plane stress and strain problems, GPa

E_{max} = maximum dynamic Young's modulus for the investigated formation, GPa

E_{min} = minimum dynamic Young's modulus for the investigated formation, GPa

E_n = normalized Young's modulus defined in Eq. 5.3

$f\,(a/R_w)$ = coefficient for two symmetrical radial cracks from circle

$f\,(b)$ = geometric coefficient of Rummel's method

FI_i = fracability index (i = 1, 2, 3)

$g\,(a/R_w)$ = coefficient for two symmetrical radial cracks from circle

$g\,(b)$ = geometric coefficient of Rummel's method

G-Criterion = maximum energy release rate criterion

G_C = critical strain energy release rate, Joule/m^2

G_{C_n} = normalized critical strain energy release rate defined in Eq. 6.5

G_{C_max} = maximum critical strain energy release rate, Joule/m^2

G_{C_min} = minimum critical strain energy release rate, Joule/m^2

$G\,(\theta)$ = total energy release rate, Joule/m^2

G_I, G_{II} = energy release rates of mode-I and mode-II fractures, Joule/m^2

GR = gamma ray

$h_a\,(b)$, $h_o\,(b)$ = geometric functions of Rummel's method

ID = Inner diameter of borehole, mm

k = Geomechanics parameter, equal to $3\text{-}4v$

K_i = stress intensity factor at different types of loadings ($i = 1, 2, 3$)

K_I, K_{II} = stress intensity factor of mode-I and mode-II, MPa·m$^{1/2}$

K_{IC}, K_{IIC} = fracture toughness of mode-I and mode-II fracture, MPa-m$^{0.5}$

K_{IC_max} = maximum fracture toughness for the investigated formation, MPa-m$^{0.5}$

K_{IC_min} = minimum fracture toughness for the investigated formation, MPa-m$^{0.5}$

K_{IC_n} = normalized fracture toughness defined in Eq. 6.7

K_I (θ), K_{II} (θ) = stress intensity factor of mode-I and mode-II for extended fracture, MPa·m$^{1/2}$

L = block side length, cm

m (x, a) = weight function

M_i = weight function parameters (i =*1,2,3*)

NPHI = neutron porosity

OD = outer diameter of borehole, mm

P = pressure inside fracture, MPa

P_b = breakdown pressure, MPa

PEF = photoelectric factor

p_o = pore pressure, *Mpa*

P_w = wellbore pressure, *Mpa*

P(x, P_w) = internal pressure distribution of preexisting fracture, *Mpa*

r = radial distance from crack tip, m

ROP = rate of penetration, ft/hr

RT = true resistivity, OHMM

R_w = borehole radius, *m*

R^2 = coefficient of determination

S = strain energy density function

S-Criterion = minimum strain energy density criterion

SIF = stress intensity factor

T = tensile strength, MPa

UCS = Uniaxial Compressive Strength, Mpa

Vp = primary sonic velocity, m/sec

w = weight fraction in fracability index model

WF = weight function

WQFM = weight of quartz, feldspar, and mica

WCAR = weight fraction of carbonate

WCLC = weight fraction of calcite

W_{QFM} = weight of quartz, feldspar, and brittle mica

W_{Carb} = weight of carbonate minerals consisting of dolomite, calcite, and other brittle carbonate

$W_{calcite}$ = weight of calcite

$W_{dolomite}$ = weight of dolomite

W_{Tot} = total weight of minerals

X = distance from the borehole wall

Y_1 = shape factor of mode-I fracture

Y_2 = shape factor of mode-II fracture

Greek symbols

β = inclination angle between preexisting crack axis and maximum principal stress

η = poroelastic constant, *0 – 0.5*

θ *in Chapter 2* = the angle refers to preexisting crack in polar coordinates, clockwise direction is negative, °

θ *in Chapters 3 and 4* = the angle of preexisting fracture refers to horizontal principal stress, clockwise direction is negative, °

θ_m = fracture initiation angle at the tip of preexisting fracture, °

λ = the ratio of pressure inside fracture to that of hole, or of horizontal stress to vertical stress. It can be constant or variable.

μ = Shear modulus, GPa

ν = Poisson's ratio

ν_{max} = maximum dynamic Poisson's ratio for the investigated formation

ν_{min} = minimum dynamic Poisson's ratio for the investigated formation

ν_n = normalized Poisson's ratio defined in Eq. 5.4

$\sigma_i(x,\theta)$ = stress distribution applied at the position of crack when the object is not fractured ($i = 1, 2, 3$)

σ_H = maximum in-situ principal stress, MPa

σ_h = minimum in-situ principal stress, MPa

σ_n = stress normal to fracture wall, MPa

σ_r = radial stress near crack tip, MPa

$\sigma_{r\theta}, \sigma_{rz}, \sigma_{\theta z}$ = shear stress near crack tip, Mpa

σ_v = overburden stress, MPa

σ_z = vertical stress near crack tip, MPa

σ_θ = tangential stress near crack tip, MPa

σ_θ-Criterion = maximum tangential stress criterion

τ = shear stress along fracture wall, Mpa

ϕ = porosity, v/v

References

Abass, H. H., S. Hedayati, and D. Meadows (1996), Nonplanar fracture propagation from a horizontal wellbore: experimental study, *SPE Production & Facilities*, *11*(3), 133-137.

Abou-Sayed, A., C. Brechtel, and R. Clifton (1978), In situ stress determination by hydrofracturing: a fracture mechanics approach, *Journal of Geophysical Research*, *83*(B6), 2851-2862.

Abousleiman, Y., M. Tran, S. Hoang, C. Bobko, A. Ortega, and F.-J. Ulm (2007), Geomechanics field and laboratory characterization of the Woodford Shale: The next gas play, paper presented at SPE Annual Technical Conference and Exhibition, Anaheim, California, U.S.A., November 11-14

Al-Shayea, N., K. Khan, and S. Abduljauwad (2000), Effects of confining pressure and temperature on mixed-mode (I–II) fracture toughness of a limestone rock, *International Journal of Rock Mechanics and Mining Sciences*, *37*(4), 629-643.

Alassi, H., R. Holt, O.-m. Nes, and S. Pradhan (2011), Realistic Geomechanical Modeling of Hydraulic Fracturing in Fractured Reservoir Rock, paper presented at Canadian Unconventional Resources Conference, Alberta, Canada, November 15-17.

Altindag, R. (2003), Correlation of specific energy with rock brittleness concepts on rock cutting, *Journal of the South African Institute of Mining and Metallurgy*, *103*(3), 163-171.

Altindag, R. (2010), Assessment of some brittleness indexes in rock-drilling efficiency, *Rock Mechanics and Rock Engineering*, *43*(3), 361-370.

Anderson, T. L. (2005), *Fracture mechanics: fundamentals and applications*, 3rd ed., CRC Press.

Andreev, G. E. (1995), *Brittle failure of rock materials: test results and constitutive models*, Taylor & Francis.

Ansah, J., M. Proett, and M. Soliman (2002), Advances in well completion design: A new 3D finite-element wellbore inflow model for optimizing performance of perforated completions, paper presented at International Symposium and Exhibition on Formation Damage Control, Lafayette, Louisiana, February 20-21.

Atkinson, B. K. (1987), Fracture mechanics approach to hydraulic fracturing stress measurements, in *Fracture mechanics of rocks*, edited, pp. 217-239, Academic Press.

Backers, T. (2005), Fracture toughness determination and micromechanics of rock under mode I and mode II loading, Doctoral thesis, University of Potsdam, Germany.

Barry, N., N. R. Whittaker, and S. G. Singh (1992), *Rock fracture mechanics principles design and applications*, ELSEVIER, Amsterdam-London-New York-Tokyo.

Barton, C., and M. Zoback (2002), Discrimination of natural fractures from drilling-induced wellbore failures in wellbore image data-implications for reservoir permeability, *SPE Reservoir Evaluation & Engineering*, *5*(3), 249-254.

Belytschko, T., and T. Black (1999), Elastic crack growth in finite elements with minimal remeshing, *International Journal for Numerical Methods in Engineering*, *45*(5), 601-620.

Berchenko, I., E. Detournay, N. Chandler, and J. Martino (2004), An in-situ thermo-hydraulic experiment in a saturated granite I: design and results, *International Journal of Rock Mechanics and Mining Sciences*, *41*(8), 1377-1394.

Berryman, J. G., and S. C. Blair (1986), Use of digital image analysis to estimate fluid permeability of porous materials: Application of two - point correlation functions, *Journal of applied Physics*, *60*(6), 1930-1938.

Bishop, A. W. (1967), Progressive Failure-with special reference to the mechanism causing it., paper presented at Geotechnical Conference, Oslo, Norway.

Blanton, T. (1982), An experimental study of interaction between hydraulically induced and pre-existing fractures, paper presented at SPE Unconventional Gas Recovery Symposium, Pittsburgh, Pennsylvania, May 16-18.

Bourgoyne Jr, A. T., K. K. Millheim, M. E. Chenevert, and F. S. Young Jr (1986), *Applied drilling engineering.*, Society of Petroleum Engineering

Bower, A. F. (2011), *Applied mechanics of solids*, 1 ed., CRC press.

Britt, L., and J. Schoeffler (2009), The geomechanics of a shale play: what makes a shale prospective, paper presented at SPE Eastern Regional Meeting, Charleston, West Virginia, USA, September 23-25.

Brook, N. (1977), The use of irregular specimens for rock strength tests, paper presented at International Journal of Rock Mechanics and Mining Sciences & Geomechanics Abstracts, Elsevier.

Bruner, K. R., and R. Smosna (2011), A Comparative Study of the Mississippian Barnett Shale, Fort Worth Basin, and Devonian Marcellus Shale, Appalachian Basin. National Energy Technology Laboratory*Rep.*, DOE/NETL-2011/1478.

Bubsey, R., D. Munz, W. Pierce, and J. Shannon Jr (1982), Compliance calibration of the short rod chevron-notch specimen for fracture toughness testing of brittle materials, *International Journal of Fracture*, *18*(2), 125-133.

Bueckner, H. (1970), Novel principle for the computation of stress intensity factors, *Zeitschrift fuer Angewandte Mathematik & Mechanik*, *50*(9).

Bunger, A., A. Lakirouhani, and E. Detournay (2010), Modelling the effect of injection system compressibility and viscous fluid flow on hydraulic fracture breakdown pressure, paper presented at Proceedings 5th International Symposium on In-situ Rock Stress, Beijing, China, August 25 - 27.

Chandler, M., P. Meredith, and B. Crawford (2013), Experimental Determination of the Fracture Toughness and Brittleness of the Mancos Shale, Utah, paper presented at European Geosciences Union General Assembly, Vienna, Austria, April 7-12.

Chang, C., M. D. Zoback, and A. Khaksar (2006), Empirical relations between rock strength and physical properties in sedimentary rocks, *Journal of Petroleum Science and Engineering*, *51*(3), 223-237.

Chapra, S. C., and R. P. Canale (2001), *Numerical Methods for Engineers: With Software and Programming Applications*, 4 ed., McGraw-Hill, Boston.

Chen, M., H. Jiang, G. Zhang, and Y. Jin (2010), The Experimental Investigation of Fracture Propagation Behavior and Fracture Geometry in Hydraulic Fracturing through Oriented Perforations, *Petroleum Science and Technology*, *28*(13), 1297-1306.

Chong, K., and M. D. Kuruppu (1984), New specimen for fracture toughness determination for rock and other materials, *International Journal of Fracture*, *26*(2), R59-R62.

Chong, K. K., W. Grieser, A. Passman, H. Tamayo, N. Modeland, and B. Burke (2010), A Completions Guide Book to Shale-Play Development: A Review of Successful Approaches toward Shale-Play Stimulation in the Last Two Decades, paper presented at Canadian Unconventional Resources and International Petroleum Conference, Calgary, Alberta, Canada, Oct 19-21.

Cleary, M., D. Johnson, H. Kogsboll, K. Owens, K. Perry, C. Pater, S. Alfred, S. Holger, and T. Mauro (1993), Field implementation of proppant slugs to avoid premature screen-out of hydraulic fractures with adequate proppant concentration, paper presented at Low Permeability Reservoirs Symposium, Denver, Colorado, April 26-28.

Collins, P. (2005), Geomechanical effects on the SAGD process, paper presented at SPE/PS-CIM/CHOA International Thermal Operations and Heavy Oil Symposium, Calgary, Alberta, Canada, November 1-3.

Copur, H., N. Bilgin, H. Tuncdemir, and C. Balci (2003), A set of indices based on indentation tests for assessment of rock cutting performance and rock properties, *Journal-South African Institute of Mining and Metallurgy*, *103*(9), 589-599.

Council, G. W. P., and A. Consulting (2009), *Modern shale gas development in the United States: A primer*, US Department of Energy, Office of Fossil Energy.

Curtis, J. B. (2002), Fractured shale-gas systems, *AAPG bulletin*, *86*(11), 1921-1938.

Daneshy, A. (1973), Experimental investigation of hydraulic fracturing through perforations, *Journal of Petroleum Technology*, *25*(10), 1201-1206.

Daneshy, A. (1978), Hydraulic fracture propagation in layered formations, *Old SPE Journal*, *18*(1), 33-41.

Daneshy, A. (2013), Horizontal Well Fracture Initiation and Extension from Cemented Cased Wells, paper presented at SPE Annual Technical Conference and Exhibition, New Orleans, Louisiana, USA, September 30 - October 2.

De Pater, C., M. Cleary, T. Quinn, D. Barr, D. Johnson, and L. Weijers (1994), Experimental verification of dimensional analysis for hydraulic fracturing, *SPE Production & Facilities*, *9*(4), 230-238.

Detournay, E., and A. Cheng (1992), Influence of pressurization rate on the magnitude of the breakdown pressure, paper presented at Proc. 33nd US Rock Mechanics Symposium, Balkema, Santa Fe, NM, June 3 - 5, 1992.

Detournay, E., and R. Carbonell (1997), Fracture-mechanics analysis of the breakdown process in minifracture or leakoff Test, *Old Production & Facilities*, *12*(3), 195-199.

Dusseault, M. B. (2010), Deep injection disposal: environmental and petroleum geomechanics, paper presented at ISRM International Symposium-6th Asian Rock Mechanics Symposium, New Delhi, India, October 23-27.

Dusterhoft, R. (1994), *FracPac completion services-stimulation and sand-control techniques for high-permeability oil and gas wells*, Halliburton Energy Services, Houston.

Dutta, N. (2002), Geopressure prediction using seismic data: Current status and the road ahead, *Geophysics*, *67*(6), 2012-2041.

Eaton, B. (1969), Fracture gradient prediction and its application in oilfield operations, *Journal of Petroleum Technology*, *21*(10), 1353-1360.

Eaton, B. (1975), The equation for geopressure prediction from well logs, paper presented at Fall Meeting of the Society of Petroleum Engineers of AIME.

Economides, M. J., and K. G. Nolte (2000), *Reservoir stimulation*, 3rd ed., Wiley, New York, NY

El Rabaa, W. (1998), Experimental study of hydraulic fracture geometry initiated from horizontal wells, *SPE REPRINT SERIES*, 166-181.

Erdogan, F., and G. Sih (1963), On the crack extension in plates under plane loading and transverse shear, *Journal of Basic Engineering*, *85*, 519.

Esmersoy, C., K. Koster, M. Williams, A. Boyd, and M. Kane (1994), Dipole shear anisotropy logging, *Resúmenes Expandidos*, 1139-1142.

Ewy, R., P. Ray, C. Bovberg, P. Norman, and H. Goodman (2001), Openhole stability and sanding predictions by 3D extrapolation from hole-collapse tests, *SPE Drilling & Completion*, *16*(4), 243-251.

Fertl, W., and G. Chilingar (1988), Total organic carbon content determined from well logs, *SPE formation evaluation*, *3*(2), 407-419.

Fisher, M., J. Heinze, C. Harris, D. BM, C. Wright, and K. Dunn (2004), Optimizing horizontal completion techniques in the Barnett shale using microseismic fracture mapping, paper presented at SPE Annual Technical Conference and Exhibition, Houston, Texas, September 26-29.

Fisher, M., C. Wright, B. Davidson, A. Goodwin, E. Fielder, W. Buckler, and N. Steinsberger (2002), Integrating fracture mapping technologies to optimize stimulations in the barnett shale, paper presented at SPE Annual Technical Conference and Exhibition, San Antonio, Texas, September 29 - October 2.

Fjar, E., R. M. Holt, A. Raaen, R. Risnes, and P. Horsrud (2008), *Petroleum related rock mechanics*, 2nd ed., Elsevier Science.

Fritz, R. D., M. K. Horn, and S. D. Joshi (1991), *Geological aspects of horizontal drilling*, The American Association of Petroleum Geologists, Tulsa, Oklahoma, USA.

Gale, J. F., and J. Holder (2010), Natural fractures in some US shales and their importance for gas production, paper presented at Geological Society, London, Petroleum Geology Conference series, Geological Society of London, January 1.

Gale, J. F., R. M. Reed, and J. Holder (2007), Natural fractures in the Barnett Shale and their importance for hydraulic fracture treatments, *AAPG bulletin*, *91*(4), 603-622.

Garagash, D., and E. Detournay (1997), An analysis of the influence of the pressurization rate on the borehole breakdown pressure, *International Journal of Solids and Structures*, *34*(24), 3099-3118.

Gardner, D. (1992), High fracturing pressures for shales and which tip effects may be responsible, paper presented at SPE Annual Technical Conference and Exhibition, Washington, D.C., October 4-7.

Ge, J., and A. Ghassemi (2011), Permeability Enhancement in Shale Gas Reservoirs after Stimulation by Hydraulic Fracturing, paper presented at 45th US Rock Mechanics/Geomechanics Symposium, San Francisco, California, June 26-29.

Geertsma, J., and F. De Klerk (1969), A rapid method of predicting width and extent of hydraulically induced fractures, *Journal of Petroleum Technology*, *21*(12), 1571-1581.

Germanovich, L., R. Hurt, J. Ayoub, E. Siebrits, D. Norman, I. Ispas, and C. Montgomery (2012), Experimental Study of Hydraulic Fracturing in Unconsolidated Materials, paper presented at SPE International Symposium and Exhibition on Formation Damage Control, Lafayette, Louisiana, February 15-17.

Ghannadi, S., M. Irani, and R. Chalaturnyk (2013), Evaluation of Induced Thermal Pressurization in Clearwater Shale Caprock in Electromagnetic Steam-Assisted Gravity-Drainage Projects, *SPE Journal*(Preprint).

Ghassemi, A., G. Wolfe, A. Diek, and J. Roegiers (1999), A chemo-mechanical model for borehole stability analyses, paper presented at Vail Rocks' 99, 37th US Rock Mechanics Symposium, Vail, Colorado, June 7-9.

Gidley, J. L. (1989), *Recent advances in hydraulic fracturing*, 1st ed., Society of Petroleum Engineers.

Glinka, G. (1996), Development of weight functions and computer integration procedures for calculating stress intensity factors around cracks subjected to complex stress fields*Rep.*, SaFFD, Inc, Petersburg Ontario, Canada.

Glinka, G., and G. Shen (1991), Universal features of weight functions for cracks in mode I, *Engineering Fracture Mechanics*, *40*(6), 1135-1146.

Göktan, R. (1991), Brittleness and micro-scale rock cutting efficiency, *Mining Science and Technology*, *13*(3), 237-241.

Gong, B., G. Qin, B. Towler, and H. Wang (2011), Discrete modeling of natural and hydraulic fractures in shale-gas reservoirs, paper presented at SPE Annual Technical Conference and Exhibition, Denver, Colorado, USA, October 30 - November 2.

Griffith, A. A. (1921), The phenomena of rupture and flow in solids, *Philosophical transactions of the royal society of london. Series A, containing papers of a mathematical or physical character*, *221*, 163-198.

Gunaydin, O., S. Kahraman, and M. Fener (2004), Sawability prediction of carbonate rocks from brittleness indexes, *JS Afr Inst Min Metall*, *104*, 1-6.

Haimson, B. C. (1968), Hydraulic fracturing in porous and nonporous rock and its potential for determining in-situ stresses at great depth, Dissertation thesis, 246 pp, University of Minnesota, Ann Arbor.

Haimson, B. C. (1981), Large scale laboratory testing of hydraulic fracturing, *Geophysical Research Letters*, *8*(7), 715-718.

Haimson, B. C., and C. Fairhurst (1967), Initiation and extension of hydraulic fractures in rocks, *Old SPE Journal*, *7*(3), 310-318.

Hajiabdolmajid, V., and P. Kaiser (2003), Brittleness of rock and stability assessment in hard rock tunneling, *Tunnelling and Underground Space Technology*, *18*(1), 35-48.

Ham, V. (1982), Hydraulic fracture geometry: fracture containment in layered formations, *Old SPE Journal*, *22*(3), 341-349.

Heidari, M., G. Khanlari, M. Torabi-Kaveh, S. Kargarian, and S. Saneie (2013), Effect of porosity on rock brittleness, *Rock Mechanics and Rock Engineering*, 1-6.

Hester, T. C., J. W. Schmoker, and H. L. Sahl (1990), Log-derived regional source-rock characteristics of the Woodford Shale, Anadarko Basin, Oklahoma.

Higgins, S. (2006), Geomechanical modeling as a reservoir characterization tool at Rulison, FieldPiceance Basin, Colorado, Master thesis, Colorado School of Mines, Golden, Colorado, USA.

Honda, H., and Y. Sanada (1956), Hardness of coal, *Fuel*, *35*, 451-461.

Hornby, B. E., L. M. Schwartz, and J. A. Hudson (1994), Anisotropic effective-medium modeling of the elastic properties of shales, *Geophysics*, *59*(10), 1570-1583.

Huang, K., Z. Zhang, and A. Ghassemi (2012), Modeling three‐dimensional hydraulic fracture propagation using virtual multidimensional internal bonds, *International Journal for Numerical and Analytical Methods in Geomechanics*.

Hubbert, M. K., and D. G. Willis (1957), Mechanics of hydraulic fracturing, *US Geological Survey*, *210*, 153-168.

Hucka, V., and B. Das (1974), Brittleness determination of rocks by different methods, *International Journal of Rock Mechanics and Mining Sciences & Geomechanics Abstracts*, *11*(10), 389-392.

Hussain, M. A. P., S. L. ; Underwood,J. H. (1974), Strain Energy Release Rate for a Crack under Combined Mode I and Mode II, *American Society for Testing and Materials*, 27.

Inamdar, A., T. Ogundare, R. Malpani, W. Atwood, K. Brook, A. Erwemi, and D. Purcell (2010), Evaluation of Stimulation Techniques Using Microseismic Mapping in the Eagle Ford Shale, paper presented at Tight Gas Completions Conference, San Antonio, Texas, November 2-3.

Ingraffea, A. R. (1977), Discrete fracture propagation in rock: laboratory tests and finite element, Doctoral thesis, University of Colorado, Denver, Colorado.

Ingraffea, A. R. (1981), Mixed-mode fracture initiation in Indiana limestone and Westerly granite, paper presented at The 22nd US Symposium on Rock Mechanics (USRMS), Cambridge, MA, June 29 - July 2.

Irwin, G. R. (1957), Analysis of stresses and strains near the end of a crack traversing a plate, *J. Appl. Mech.*

Ishijima, Y., and J. Roegiers (1983), Fracture initiation and breakdow pressure-Are they similar?, paper presented at The 24th US Symposium on Rock Mechanics (USRMS), College Station, TX, June 20 - 23.

Ispas, I., R. Eve, R. Hickman, R. Keck, S. Willson, and K. Olson (2012), Laboratory Testing and Numerical Modelling of Fracture Propagation from Deviated Wells in Poorly Consolidated Formations, paper presented at SPE Annual Technical Conference and Exhibition, San Antonio, Texas, USA, October 8-10.

Jackson, J. A., J. P. Mehl, and K. K. Neuendorf (2005), *Glossary of geology*, Springer.

Jaeger, J. C., N. G. W. Cook, and R. Zimmerman (2009), *Fundamentals of rock mechanics*, 4th ed., Malden, MA, USA.

Jarvie, D. M., R. J. Hill, T. E. Ruble, and R. M. Pollastro (2007), Unconventional shale-gas systems: The Mississippian Barnett Shale of north-central Texas as one model for thermogenic shale-gas assessment, *AAPG bulletin*, *91*(4), 475-499.

Jeffrey, R. (1989), The combined effect of fluid lag and fracture toughness on hydraulic fracture propagation, paper presented at Low Permeability Reservoirs Symposium, Denver, Colorado, March 6-8.

Jin, X., and S. Shah (2013), Fracture propagation direction and its application in hydraulic fracturing, paper presented at SPE Hydraulic Fracturing Technology Conference, The Woodlands, TX, USA, February 04-06.

Jin, X., S. Shah, and M. Sheng (2012), Hydraulic fracturing model based on nonlinear facture mechanics: theory and simulation, paper presented at SPE Annual Technical Conference and Exhibition, San Antonio, Texas, USA, October 8 -10.

Jin, X., S. Shah, J. Roegiers, and B. Hou (2013), Breakdown Pressure Determination-A Fracture Mechanics Approach, paper presented at SPE Annual Technical Conference and Exhibition, New Orleans, Louisiana, USA, Sep 30 - Oct 2.

Josh, M., L. Esteban, C. Delle Piane, J. Sarout, D. Dewhurst, and M. Clennell (2012), Laboratory characterisation of shale properties, *Journal of Petroleum Science and Engineering*, *88*, 107-124.

Kemeny, J., and R. Post (2003), Estimating three-dimensional rock discontinuity orientation from digital images of fracture traces, *Computers & Geosciences*, *29*(1), 65-77.

Khan, S., and M. K. Khraisheh (2000), Analysis of mixed mode crack initiation angles under various loading conditions, *Engineering Fracture Mechanics*, *67*(5), 397-419.

Kiciak, A., G. Glinka, and D. Burns (2003), Calculation of stress intensity factors and crack opening displacements for cracks subjected to complex stress fields, *Journal of pressure vessel technology*, *125*(3), 260-266.

King, G. (2012), Hydraulic fracturing 101: what every representative, environmentalist, regulator, reporter, investor, university researcher, neighbor and engineer should know about estimating frac risk and improving frac performance in unconventional gas and oil wells, paper presented at SPE Hydraulic Fracturing Technology Conference, The Woodlands, TX, USA, February 6-8.

Knackstedt, M. A., S. Latham, M. Madadi, A. Sheppard, T. Varslot, and C. Arns (2009), Digital rock physics: 3D imaging of core material and correlations to acoustic and flow properties, *The Leading Edge*, *28*(1), 28-33.

Kumar, V. (2012), characterization of shale using nano-indentation, Master thesis, University of Oklahoma, Norman, Oklahoma.

Kundert, D., and M. Mullen (2009), Proper evaluation of shale gas reservoirs leads to a more effective hydraulic-fracture stimulation, paper presented at SPE Rocky Mountain Petroleum Technology Conference, Denver, Colorado, April 14-16.

Lawn, B., and D. Marshall (1979), Hardness, toughness, and brittleness: an indentation analysis, *Journal of the American ceramic society*, *62*(7-8), 347-350.

Li, Q., M. Chen, Y. Jin, Y. Zhou, F. Wang, and R. Zhang (2013), Rock Mechanical Properties of Shale Gas Reservoir and Their Influences on Hydraulic Fracture, paper presented at 6th International Petroleum Technology Conference, Beijing, China, Mar 26-28.

Li, X., L. Cui, and J.-C. Roegiers (1998), Thermoporoelastic modelling of wellbore stability in non-hydrostatic stress field, *International Journal of Rock Mechanics and Mining Sciences*, *35*(4), 584.

Li, Y., and A. Ghassemi (2012), Creep Behavior of Barnett, Haynesville, and Marcellus Shale, *American Rock Mechanics Association (ARMA)*.

Lord, D., and S. Shah (1994), Study of perforation friction pressure employing a large-scale fracturing flow simulator, paper presented at SPE Annual Technical Conference and Exhibition, New Orleans, Louisiana, September 25-28.

Luffel, D., and F. Guidry (1992), New core analysis methods for measuring reservoir rock properties of Devonian shale, *Journal of Petroleum Technology*, *44*(11), 1184-1190.

Luffel, D., C. Hopkins, and P. Schettler (1993), Matrix permeability measurement of gas productive shales, paper presented at SPE Annual Technical Conference and Exhibition, Houston, Texas, October 3-6.

Matthews, W., and J. Kelly (1967), How to predict formation pressure and fracture gradient, *Oil and Gas Journal*, *65*(8), 92-106.

Mavko, G., T. Mukerji, and J. Dvorkin (2009), *The rock physics handbook: Tools for seismic analysis of porous media*, Cambridge University Press.

Miller, T. C. (2000), Analysis of mixed-mode cracks in a rubbery particulate composite, *Composites Part B: Engineering*, *31*(4), 319-325.

Moes, N., J. Dolbow, and T. Belytschko (1999), A finite element method for crack growth without remeshing, *Int. J. Numer. Meth. Engng*, *46*, 131-150.

Montgomery, C., and R. Steanson (1985), Proppant selection: the key to successful fracture stimulation, *Journal of Petroleum Technology*, *37*(12), 2,163-162,172.

Moran, J., and S. Gianzero (1979), Effects of formation anisotropy on resistivity-logging measurements, *Geophysics*, *44*(7), 1266-1286.

Nagel, N., and M. Sanchez-Nagel (2011), Stress shadowing and microseismic events: a numerical evaluation, paper presented at SPE Annual Technical Conference and Exhibition, Denver, Colorado, USA, October 30 - November 2.

Nasseri, M., and B. Mohanty (2008), Fracture toughness anisotropy in granitic rocks, *International Journal of Rock Mechanics and Mining Sciences*, *45*(2), 167-193.

Newman Jr, J. (1971), *An improved method of collocation for the stress analysis of cracked plates with various shaped boundaries*, National Aeronautics and Space Administration.

Nguyen, V., and Y. Abousleiman (2009), The Porochemothermoelastic Coupled Solutions of Stress and Pressure With Applications to Wellbore Stability in Chemically Active Shale, paper presented at SPE Annual Technical Conference and Exhibition, New Orleans, Louisiana, October 4-7

Nordgren, R. (1972), Propagation of a vertical hydraulic fracture, *Old SPE Journal*, *12*(4), 306-314.

Olson, J. (2008), Multi-fracture propagation modeling: Applications to hydraulic fracturing in shales and tight gas sands, paper presented at The 42nd US Rock Mechanics Symposium (USRMS), San Francisco, CA, June 29 - July 2.

Olson, J., and K. Wu (2012), Sequential vs. Simultaneous Multizone Fracturing in Horizontal Wells: Insights From a Non-Planar, Multifrac Numerical Model, paper presented at SPE Hydraulic Fracturing Technology Conference, The Woodlands, Texas, USA, February 6-8.

Paris, P. C., and G. C. Sih (1965), Stress analysis of cracks, *ASTM stp*, *381*, 30-83.

Passey, Q., S. Creaney, J. Kulla, F. Moretti, and J. Stroud (1990), A practical model for organic richness from porosity and resistivity logs, *AAPG bulletin*, *74*(12), 1777-1794.

Peng, S., and J. Zhang (2007), *Engineering geology for underground rocks*, Springer-Verlag Berlin Heidelberg.

Perkins, T., and L. Kern (1961), Widths of hydraulic fractures, *Journal of Petroleum Technology*, *13*(9), 937-949.

Perkins, T., and J. Weingarten (1988), Stability and failure of spherical cavities in unconsolidated sand and weakly consolidated rock, paper presented at SPE Annual Technical Conference and Exhibition, Houston, Texas, October 2-5.

Potluri, N., D. Zhu, and A. Hill (2005), The effect of natural fractures on hydraulic fracture propagation, paper presented at SPE European Formation Damage Conference, Sheveningen, The Netherlands, May 25-27, 2005.

Protodyakonov, M. (1962), Mechanical properties and drillability of rocks, paper presented at Proceedings of the 5th Symposium on Rock Mechanics, Minnesota, May.

Quinn, J. B., and G. D. Quinn (1997), Indentation brittleness of ceramics: a fresh approach, *Journal of Materials Science*, *32*(16), 4331-4346.

Rao, Q., Z. Sun, O. Stephansson, C. Li, and B. Stillborg (2003), Shear fracture (mode II) of brittle rock, *International Journal of Rock Mechanics and Mining Sciences*, *40*(3), 355-375.

Rice, J. R. (1968a), Mathematical analysis in the mechanics of fracture, *Fracture: An advanced treatise*, *2*, 191-311.

Rice, J. R. (1968b), A path independent integral and the approximate analysis of strain concentration by notches and cracks, *Journal of Applied Mechanics*, *35*, 379-386.

Rice, J. R. (1972), Some remarks on elastic crack-tip stress fields, *International Journal of Solids and Structures*, *8*(6), 751-758.

Rickman, R., M. Mullen, J. Petre, W. Grieser, and D. Kundert (2008), A practical use of shale petrophysics for stimulation design optimization: all shale plays are not clones of the barnett shale, paper presented at SPE Annual Technical Conference and Exhibition, Denver, Colorado, USA, September 21-24.

Roegiers, J. (1989), Elements of rock mechanics, *Reservoir stimulation: Englewood Cliffs, New Jersey, Prentice Hall*, 2-1.

Rossmanith, H. P. (1983), *Rock fracture mechanics*, 1 ed., Springer, Verlag.

Rummel, F. (1987), Fracture mechanics approach to hydraulic fracturing stress measurements, *Fracture Mechanics of rocks*, 217-240.

Rummel, F., and J. Hansen (1989), Interpretation of hydrofrac pressure recordings using a simple fracture mechanics simulation model, *International Journal of Rock Mechanics and Mining Sciences & Geomechanics Abstracts*, *26*(6), 483-488.

Sayers, C., G. Johnson, and G. Denyer (2002), Predrill pore-pressure prediction using seismic data, *Geophysics*, *67*(4), 1286-1292.

Sehgal, J., Y. Nakao, H. Takahashi, and S. Ito (1995), Brittleness of glasses by indentation, *Journal of materials science letters*, *14*(3), 167-169.

Settari, A., and D. Walters (2001), Advances in coupled geomechanical and reservoir modeling with applications to reservoir compaction, *SPE Journal*, *6*(3), 334-342.

Shen, G., and G. Glinka (1991), Determination of weight functions from reference stress intensity factors, *Theoretical and applied fracture mechanics*, *15*(3), 237-245.

Sheng, M., G. Li, S. Shah, and X. Jin (2012), Extended finite element modeling of multi-scale flow in fractured shale gas reservoirs, paper presented at SPE Annual Technical Conference and Exhibition, San Antonio, TX, USA, October 8-10.

Shlyapobersky, J., G. Wong, and W. Walhaug (1988), Overpressure calibrated design of hydraulic fracture stimulations, paper presented at SPE Annual Technical Conference and Exhibition, Houston, Texas, October 2-5.

Sierra, R., M. Tran, Y. Abousleiman, and R. Slatt (2010), Woodford Shale mechanical properties and the impacts of lithofacies, paper presented at Proceedings symposium on the 44th US rock mechanics symposium and 5th US–Canada rock mechanics symposium, Salt Lake City, Utah, June 27-30.

Sih, G. C. (1973), *Handbook of Stress-intensity Factors for Researchers and Engineers: Stress-intensity Factor Solutions and Formulas for Reference*, Institute of Fracture and Solid Mechanics, Lehigh University, Bethlehem, PA.

Sih, G. C. (1974), Strain-energy-density factor applied to mixed mode crack problems, *International Journal of Fracture*, *10*(3), 305-321.

Simonson, E., A. Abou-Sayed, and R. Clifton (1978), Containment of massive hydraulic fractures, *Old SPE Journal*, *18*(1), 27-32.

Singh, S. (1986), Brittleness and the mechanical winning of coal, *Mining Science and Technology*, *3*(3), 173-180.

Slatt, R. M., and Y. Abousleiman (2011), Multi-scale, brittle-ductile couplets in unconventional gas shales: merging sequence stratigraphy and geomechanics, paper presented at AAPG Annual Convention and Exhibition, Houston, Texas, USA, April 10-13.

Soliman, M., J. Hunt, and A. El Rabaa (1990), Fracturing aspects of horizontal wells, *Journal of Petroleum Technology*, *42*(8), 966-973.

Sondergeld, C., K. Newsham, J. Comisky, M. Rice, and C. Rai (2010), Petrophysical considerations in evaluating and producing shale gas resources, paper presented at SPE Unconventional Gas Conference, Pittsburgh, Pennsylvania, February 23-25.

Sone, H. (2012), Mechanical Properties of Shale Gas Reservoir Rocks, and Its Relation to the In-situ Stress Variation Observed in Shale Gas Reservoirs, Dissertation thesis, 225 pp, Stanford University, California.

Stenhaug, M., L. Erichsen, F. H. Doornbosch, and R. A. Parrott (2003), A Step Change in Perforating Technology Improves Productivity of Horizontal Wells in the North Sea, paper presented at SPE International Improved Oil Recovery Conference in Asia Pacific, Kuala Lumpur, October 20-21.

Tada, H., P. C. Paris, G. R. Irwin, and H. Tada (2000), *The stress analysis of cracks handbook*, ASME press New York.

Thomas, R., and D. Ward (1972), Effect of overburden pressure and water saturation on gas permeability of tight sandstone cores, *Journal of Petroleum Technology*, *24*(2), 120-124.

Tiab, D., and E. C. Donaldson (2011), *Petrophysics: theory and practice of measuring reservoir rock and fluid transport properties*, Gulf professional publishing.

Tran, M. (2009), Geomechanics field and laboratory characterization of Woodford Shale, Master thesis, University of Oklahoma, Norman, Oklahoma.

Ulm, F.-J., and Y. Abousleiman (2006), The nanogranular nature of shale, *Acta Geotechnica*, *1*(2), 77-88.

Valkó, P., and M. J. Economides (1995), *Hydraulic fracture mechanics*, Wiley Chichester, UK.

Wang, F., and J. Gale (2009), Screening criteria for shale-gas systems, *Gulf Coast Association of Geological Societies Transactions*, *59*, 779-793.

Wang, H., M. Soliman, and B. Towler (2009), Investigation of factors for strengthening a wellbore by propping fractures, *SPE Drilling & Completion*, *24*(3), 441-451.

Wang, Y., and M. Dusseault (1991), Hydraulic fracture stress measurement in rocks with stress-dependent Young's modulus, paper presented at The 32nd US Symposium on Rock Mechanics (USRMS), Norman, Oklahoma, July 10 - 12, 1991.

Weijers, L., C. de Pater, and J. Hagoort (1996), A new mechanism for hydraulic fracture initiation, paper presented at 2nd North American Rock Mechanics Symposium, Montreal, Quebec, Canada, June 19-21.

Weingarten, J., and T. Perkins (1995), Prediction of sand production in gas wells: methods and Gulf of Mexico case studies, *Journal of Petroleum Technology*, *47*(7), 596-600.

Willson, S., A. Fossum, and J. Fredrich (2003), Assessment of salt loading on well casings, *SPE Drilling & Completion*, *18*(1), 13-21.

Wiprut, D., and M. D. Zoback (2000), Fault reactivation and fluid flow along a previously dormant normal fault in the northern North Sea, *Geology*, *28*(7), 595-598.

Wu, K., and J. Olson (2013), Investigation of critical in-situ and injection factors in Multi-Frac treatments: guidelines for controlling fracture complexity, paper presented at the SPE Hydraulic Fracturing Technology Conference, The Woodlands, TX, USA, February 04-06.

Yagiz, S. (2009), Assessment of brittleness using rock strength and density with punch penetration test, *Tunnelling and Underground Space Technology*, *24*(1), 66-74.

Yarali, O., and S. Kahraman (2011), The drillability assessment of rocks using the different brittleness values, *Tunnelling and Underground Space Technology*, *26*(2), 406-414.

Yew, C. H. (1997), *Mechanics of hydraulic fracturing*, 1st ed., Gulf Professional Publishing.

Yi, X., P. Valko, and J. Russell (2004), Predicting critical drawdown for the onset of sand production, paper presented at SPE International Symposium and Exhibition on Formation Damage Control, Lafayette, Louisiana, February 18-20.

Yuan, R., B. Xu, C. Zhu, L. Jin, and S. Vitthal (2013), High Pressure Stimulation-Impact of Hydraulic Fracture Geometry to Unconventional Gas Appraisal and Development in Compressional Settings, paper presented at SPE Annual Technical Conference and Exhibitions, New Orleans, Louisiana, September 30-October 2.

Zehnder, A. T. (2012), *Fracture Mechanics*, 1st ed., Springer.

Zhang, J. (2011), Pore pressure prediction from well logs: Methods, modifications, and new approaches, *Earth-Science Reviews*, *108*(1), 50-63.

Zhang, J., M. Bai, and J.-C. Roegiers (2003), Dual-porosity poroelastic analyses of wellbore stability, *International Journal of Rock Mechanics and Mining Sciences*, *40*(4), 473-483.

Zhang, X., R. Jeffrey, A. Bunger, and M. Thiercelin (2011), Initiation and growth of a hydraulic fracture from a circular wellbore, *International Journal of Rock Mechanics and Mining Sciences*, *48*(6), 984-995.

Zhao, X., and J.-C. Roegiers (1993), Determination of in situ fracture toughness, *International journal of rock mechanics and mining sciences & geomechanics abstracts*, *30*(7), 837-840.

Zheng, X., and G. Glinka (1995), Weight functions and stress intensity factors for longitudinal semi-elliptical cracks in thick-wall cylinders, *Journal of pressure vessel technology*, *117*(4), 383-389.

Zheng, X., A. Kiciak, and G. Glinka (1997), Weight functions and stress intensity factors for internal surface semi-elliptical crack in thick-walled cylinder, *Engineering Fracture Mechanics*, *58*(3), 207-221.

Zhou, J., M. Chen, Y. Jin, and G. Zhang (2008), Analysis of fracture propagation behavior and fracture geometry using a tri-axial fracturing system in naturally fractured reservoirs, *International Journal of Rock Mechanics and Mining Sciences*, *45*(7), 1143-1152.

Zoback, M. D. (2010), *Reservoir geomechanics*, Cambridge University Press, Cambridge.

Appendix

Appendix A: Solution of Maximum Tangential Stress Criterion

σ_θ-Criterion assumes that fracture grows at an angle where tangential stress is maxim [*Erdogan and Sih*, 1963], which corresponds to zero shear stress.

$$\sigma_{r\theta} = \frac{K_I}{\sqrt{2\pi r}} \cos\frac{\theta_m}{2} \sin\frac{\theta_m}{2} cos\frac{\theta_m}{2} + \frac{K_{II}}{\sqrt{2\pi r}} \cos\frac{\theta_m}{2}\left(1 - 3\sin^2\frac{\theta_m}{2}\right) = 0 \quad \text{(A-1)}$$

Solving Eq. A-1 for fracture propagation angle θ_m

$$\theta_m = 2arc\tan\left[\frac{1}{4}\frac{K_I}{K_{II}} \pm \frac{1}{4}\sqrt{\left(\frac{K_I}{K_{II}}\right)^2 + 8}\right] \quad \text{(A-2)}$$

The solution $\theta_m = 2arc\tan\left[\frac{1}{4}\frac{K_I}{K_{II}} + \frac{1}{4}\sqrt{\left(\frac{K_I}{K_{II}}\right)^2 + 8}\right]$ is rejected because $\frac{\partial^2\sigma_\theta}{\partial\theta^2} > 0$, which is against the assumptions of σ_θ-Criterion [*Erdogan and Sih*, 1963].

As a result, the proper solution for fracture propagation angle θ_m is,

$$\theta_m = 2arc\tan\left[\frac{1}{4}\frac{K_I}{K_{II}} - \frac{1}{4}\sqrt{\left(\frac{K_I}{K_{II}}\right)^2 + 8}\right] \quad \text{(A-3)}$$

Substituting Eqs. 5 and 6 into Eq. A-3, the analytical solution of fracture initiation angle θ_m is obtained as follows,

$$\theta_m = 2arc\tan\left[\frac{1}{2}\left(\frac{P-(\sigma_H\sin^2\beta+\sigma_h\cos^2\beta)}{(\sigma_H-\sigma_h)\sin 2\beta}\right) - \frac{1}{2}\sqrt{\left(\frac{P-(\sigma_H\sin^2\beta+\sigma_h\cos^2\beta)}{(\sigma_H-\sigma_h)\sin 2\beta}\right)^2 + 2}\right] \quad \text{(A-4)}$$

Appendix B: Solution of Maximum Energy Release Rate

The word "rate" does not mean the derivative of energy with respective to time, *Joule/sec*, but *Joule/m*^{2}, which is equivalent to *N/m* after unit conversion, so the energy release rate can also be considered as driving force for the propagation of fractures [*Sih*, 1974]. Energy release rate is defined as

$$G(\theta) = G_I + G_{II} = \frac{1}{E'}\left(K_I{}^2(\theta) + K_{II}^2(\theta)\right) \quad \text{(B-1)}$$

$E' = E/(1-\upsilon^2)$ for plane strain, and E for plane stress.

The SIFs of extended fracture are [*Barry, Whittaker and Singh*, 1992].

$$\begin{bmatrix} K_I(\theta) \\ K_{II}(\theta) \end{bmatrix} = \frac{4}{4-\sin^2\theta}\left(\frac{1-\theta/\pi}{1+\theta/\pi}\right)^{\theta/2\pi} \begin{bmatrix} K_I\cos\theta + \frac{3}{2}K_{II}\sin\theta \\ K_{II}\cos\theta - \frac{K_I}{2}\sin\theta \end{bmatrix} \tag{B-2}$$

Substitute Eqs. 5 and 6 into Eq. B-2,

$$\begin{bmatrix} K_I(\theta) \\ K_{II}(\theta) \end{bmatrix} =$$

$$\frac{4\sqrt{\pi a}}{4-\sin^2\theta}\left(\frac{1-\theta/\pi}{1+\theta/\pi}\right)^{\theta/2\pi} \begin{bmatrix} (P-\sigma_H\sin^2\beta-\sigma_h\cos^2\beta)\cos\theta + \frac{3}{4}(\sigma_H-\sigma_h)\sin 2\beta\sin\theta \\ \frac{1}{2}(\sigma_H-\sigma_h)\sin 2\beta\cos\theta - \frac{(P+\alpha_1 p-\sigma_H\sin^2\beta-\sigma_h\cos^2\beta)}{2}\sin\theta \end{bmatrix}$$

(B-3)

Fracture occurs where energy release rate is maximum, the mathematical criteria are

$$\frac{\partial G}{\partial\theta} = 0, \quad \frac{\partial^2 G}{\partial\theta^2} < 0 \tag{B-4}$$

The energy release rate function *G (ϴ)* is obtained by substituting Eq. B-3 into Eq. B-1, then substituting *G (ϴ)* into Eq. B-4

$$\cos\theta\sin\theta\left(4\left((\sigma_h-\sigma_H)\cos\theta\sin 2\beta + (P_b-\sigma_h\cos^2\beta-\sigma_H\sin^2\beta)\sin\theta\right)^2 + (4\cos\theta(P_b-\sigma_h\cos^2\beta-\sigma_H\sin^2\beta)+3(\sigma_H-\sigma_h)\sin 2\beta\sin\theta)^2\right) + \left(\frac{2\theta}{-\pi^2+\theta^2} + \frac{log\left(-1+\frac{2\pi}{\pi+\theta}\right)}{\pi}\right)(-4+\sin^2\theta)\left(4\left((\sigma_h-\sigma_H)\cos\theta\sin 2\beta + (P_b-\sigma_h\cos^2\beta-\sigma_H\sin^2\beta)\sin\theta\right)^2 + (4\cos\theta(P_b-\sigma_h\cos^2\beta-\sigma_H\sin^2\beta)+3(\sigma_H-\sigma_h)\sin 2\beta\sin\theta)^2\right) + (-4+\sin^2\theta)\left(8(\sigma_h-\sigma_H)(-2P_b+\sigma_h+\sigma_H+(\sigma_h-\sigma_H)\cos 2\beta)\cos 2\theta\sin 2\beta - 2\left(6{P_b}^2+\sigma_h^2+6P_b(-\sigma_h-\sigma_H)+4\sigma_h\sigma_H+\sigma_H^2-\right.\right.$$

$$6(\sigma_h+\sigma_H)+(\sigma_h-\sigma_H)(3(-2P_b+\sigma_h+\sigma_H)\cos2\beta+2(\sigma_h-\sigma_H)\cos4\beta)\Big)\sin2\theta\Big)=0$$

(B-5)

Analytical solution of Eq. B-5 is not available, Bisection method [*Chapra and Canale*, 2001] is modified and implemented in the numerical codes to find the root for the fracture initiation angle θ_m at different inclination angle β (0°-90°), as is plotted in Fig. 2.6.

Appendix C: Solution of Minimum Strain Energy Density Criterion

This criterion was proposed by Sih [*Sih*, 1973; 1974] and it is demonstrated that there is a direction where the strain energy density is minimum and it corresponds to the maximum potential energy, which is the preferred path for the initiation and propagation of fractures.

The strain energy density function is [*Sih*, 1974]

$$S=\frac{1}{2\mu}\left[\frac{k+1}{8}(\sigma_r+\sigma_\theta)^2-\sigma_r\sigma_\theta+\sigma_{r\theta}^2\right] \quad \text{(C-1)}$$

Fracture takes place where strain energy density is minimum, the mathematical criteria are

$$\frac{\partial S}{\partial\theta}=0,\quad \frac{\partial^2 S}{\partial\theta^2}>0 \quad \text{(C-2)}$$

Substituting Eqs. 5, 6 and 11 into Eq. C-1, then taking the first derivative with respect to Eq. C-1,

$$4(\sigma_h-\sigma_H)(-2P_b+\sigma_H+\sigma_h+(\sigma_h-\sigma_H)\cos2\beta)\cos2\theta\sin2\beta-(-1+$$

$$k)((-2P_b+\sigma_H+\sigma_h)^2+2(\sigma_h-\sigma_H)(-2P_b+\sigma_H+\sigma_h)\cos2\beta+(\sigma_h-$$

$$\sigma_H)^2\cos4\beta)\sin\theta+4(\sigma_h-\sigma_H)\cos\theta\Big((-1+k)(P_b-\sigma_h\cos^2\beta-\sigma_H\sin^2\beta)\sin2\beta+$$

$\left((-2P_b + \sigma_H + \sigma_h)\cos 2\beta + (\sigma_h - \sigma_H)\cos 4\beta\right)\sin\theta\Big) + 4(P_b - \sigma_h)(P_b - \sigma_H)\sin 2\theta = 0$ (C-3)

The modified bisection method implemented in the solution of Maximum Energy Release Rate is also applied to find roots for the fracture initiation angle θ_m at different inclination angle β (0°-90°), as is shown in Fig. 2.6.

Appendix D: Algorithm of Modified Bisection Method

The success of bisection method depends on the selection of both starting and end points. If there is no root between the two ends, the program will not converge. Make some adjustments finding numerical roots for Eqs. B-5 or C-3.

Firstly, calculate breakdown pressure at the inclination angle β with Eq. 10.

Secondly, prior to searching for fracture initiation angle, add a command to ensure $f(x_l) \cdot f(x_u) < 0$ (x_l is the left end point, x_u is right end point). If not, keep x_u as constant, and increase x_l gradually with small steps until $f(x_l') \cdot f(x_u) < 0$ (x_l' is the new left end point);

Thirdly, the simulation is allowed to run and search for fracture initiation angle between x_l' and $x_u$following the classical procedure of Bisection method [*Chapra and Canale*, 2001]. The convergence criterion is set strictly as $|(x_{new} - x_{old})/x_{new}| < 10^{-40}$;

Finally, make sure $\frac{\partial^2 G}{\partial \theta_m^2} < 0$ for G-Criterion, and $\frac{\partial^2 S}{\partial \theta_m^2} > 0$ for S-Criterion.

In conclusion, the modified bisection method developed in this paper can solve the nonlinear equation automatically, and search for fracture initiation angle with updating breakdown pressure at different inclination angle (0°-90°) automatically and consecutively.

Appendix E: Mathematica code for solving parameters of weight function

$$\text{Assuming}[R_w > 0 \&\& a > 0,$$

$$\text{Solve}[\sqrt{\pi a}\left(1-\frac{a}{R_w+a}\right)\left(0.637+0.485\left(1-\frac{a}{R_w+a}\right)^2+0.4\left(\frac{a}{R_w+a}\right)^2\left(1-\frac{a}{R_w+a}\right)\right)-$$

$$\text{Integrate}\left[\left(\frac{R_w}{R_w+x}\right)^2\frac{2}{\sqrt{2\pi(a-x)}}\left(1+M_1\left(1-\frac{x}{a}\right)^{0.5}+M_2\left(1-\frac{x}{a}\right)+M_3\left(1-\frac{x}{a}\right)^{1.5},\{x,0,a\}\right]\right]$$

$$== 0$$

$$\&\&$$

$$\sqrt{\pi a}\left(1+\left(1-\frac{a}{R_w+a}\right)\left(0.5+0.743\left(1-\frac{a}{R_w+a}\right)^2\right)\right)-$$

$$\text{Integrate}\left[\left(\left(\frac{R_w}{R_w+x}\right)^2+1\right)\frac{2}{\sqrt{2\pi(a-x)}}\left(1+M_1\left(1-\frac{x}{a}\right)^{0.5}+M_2\left(1-\frac{x}{a}\right)\right.\right.$$

$$\left.\left.+M_3\left(1-\frac{x}{a}\right)^{1.5},\{x,0,a\}\right]==0\right.$$

$$\left.\&\&1+M_2-M_3==0,\{M_1,M_2,M_3\}\right]]$$

Appendix F: Weight function parameters for symmetrical radial cracks emanating from borehole

Table F-1 Parameters of weight function for different ratio of crack length to circular radius.

a/R_w	M_1	M_2	M_3	a/R_w	M_1	M_2	M_3	a/R_w	M_1	M_2	M_3
0.001	-8.5085	9.54248	5.27124	0.36	-0.24015	0.198545	0.599272	2.00	-0.20741	0.059727	0.529864
0.002	-3.8161	4.422013	2.711007	0.37	-0.24951	0.204179	0.60209	2.05	-0.20121	0.054455	0.527228
0.003	-2.2565	2.719114	1.859557	0.38	-0.25836	0.20942	0.60471	2.10	-0.19518	0.049372	0.524686
0.004	-1.4801	1.870579	1.43529	0.39	-0.26673	0.214286	0.607143	2.15	-0.18932	0.044471	0.522235
0.005	-1.0169	1.36377	1.181885	0.40	-0.27465	0.218797	0.609398	2.20	-0.18362	0.039745	0.519873
0.006	-0.7103	1.027805	1.013903	0.41	-0.28212	0.222969	0.611484	2.25	-0.17808	0.035189	0.517595
0.007	-0.4932	0.789452	0.894726	0.42	-0.28918	0.226819	0.613409	2.30	-0.1727	0.030796	0.515398
0.008	-0.332	0.612093	0.806046	0.43	-0.29584	0.230363	0.615182	2.35	-0.16747	0.02656	0.51328
0.009	-0.2081	0.475385	0.737693	0.44	-0.30212	0.233617	0.616808	2.40	-0.16239	0.022474	0.511237
0.01	-0.1102	0.367123	0.683562	0.45	-0.30803	0.236594	0.618297	2.45	-0.15745	0.018533	0.509266
0.02	0.29602	-0.090763	0.454619	0.46	-0.3136	0.239309	0.619655	2.50	-0.15266	0.014731	0.507365
0.03	0.39232	-0.21007	0.394965	0.47	-0.31883	0.241775	0.620887	2.55	-0.148	0.011062	0.505531
0.04	0.41345	-0.246926	0.376537	0.48	-0.32374	0.244003	0.622002	2.60	-0.14347	0.007522	0.503761
0.05	0.40624	-0.252414	0.373793	0.49	-0.32834	0.246007	0.623003	2.65	-0.13907	0.004105	0.502053
0.06	0.38618	-0.243455	0.378273	0.50	-0.33266	0.247797	0.623898	2.70	-0.1348	0.000807	0.500403
0.07	0.35982	-0.227214	0.386393	0.55	-0.35031	0.253897	0.626949	2.75	-0.13065	-0.00238	0.498811
0.08	0.33038	-0.207208	0.396396	0.60	-0.36238	0.256063	0.628032	2.80	-0.12661	-0.00545	0.497273
0.09	0.29959	-0.185334	0.407333	0.65	-0.37001	0.255207	0.627604	2.85	-0.12269	-0.00843	0.495787
0.10	0.26843	-0.162683	0.418658	0.70	-0.3741	0.252044	0.626022	2.90	-0.11888	-0.0113	0.494352
0.11	0.2375	-0.139913	0.430043	0.75	-0.37536	0.247133	0.623567	2.95	-0.11517	-0.01407	0.492965
0.12	0.20717	-0.117429	0.441285	0.80	-0.37437	0.240916	0.620458	3.00	-0.11157	-0.01675	0.491624
0.13	0.17764	-0.095484	0.452258	0.85	-0.37161	0.233737	0.616869	3.05	-0.10807	-0.01934	0.490328
0.14	0.14906	-0.074236	0.462882	0.90	-0.36745	0.22587	0.612935	3.10	-0.10466	-0.02185	0.489074
0.15	0.12151	-0.05378	0.47311	0.95	-0.3622	0.217529	0.608765	3.15	-0.10135	-0.02428	0.487862
0.16	0.09502	-0.03417	0.482915	1.00	-0.3561	0.208882	0.604441	3.20	-0.09812	-0.02662	0.486689
0.17	0.06961	-0.015432	0.492284	1.05	-0.34935	0.200062	0.600031	3.25	-0.09499	-0.02889	0.485554
0.18	0.04528	0.002427	0.501214	1.10	-0.34212	0.191171	0.595585	3.30	-0.09193	-0.03109	0.484456
0.19	0.02201	0.019413	0.509706	1.15	-0.33454	0.18229	0.591145	3.35	-0.08896	-0.03321	0.483393
0.20	-0.0002	0.035539	0.51777	1.20	-0.32672	0.173483	0.586741	3.40	-0.08607	-0.03527	0.482363
0.21	-0.0214	0.050828	0.525414	1.25	-0.31874	0.164796	0.582398	3.45	-0.08325	-0.03727	0.481366
0.22	-0.0417	0.065303	0.532652	1.30	-0.31068	0.156265	0.578133	3.50	-0.08051	-0.0392	0.4804
0.23	-0.0609	0.078993	0.539496	1.35	-0.30259	0.147919	0.57396	3.55	-0.07784	-0.04107	0.479464
0.24	-0.0793	0.091925	0.545962	1.40	-0.29453	0.139776	0.569888	3.60	-0.07524	-0.04288	0.478558
0.25	-0.0968	0.10413	0.552065	1.45	-0.28652	0.131851	0.565926	3.65	-0.0727	-0.04464	0.477679
0.26	-0.1134	0.115637	0.557818	1.50	-0.2786	0.124152	0.562076	3.70	-0.07024	-0.04635	0.476826
0.27	-0.1292	0.126476	0.563238	1.55	-0.27079	0.116685	0.558342	3.75	-0.06783	-0.048	0.476
0.28	-0.1443	0.136677	0.568338	1.60	-0.26311	0.109451	0.554726	3.80	-0.06548	-0.0496	0.475199
0.29	-0.1586	0.146268	0.573134	1.65	-0.25557	0.102452	0.551226	3.85	-0.06319	-0.05116	0.474421
0.30	-0.1721	0.155276	0.577638	1.70	-0.24819	0.095685	0.547843	3.90	-0.06096	-0.05267	0.473667
0.31	-0.185	0.163729	0.581865	1.75	-0.24097	0.089148	0.544574	3.95	-0.05879	-0.05413	0.472935
0.32	-0.1972	0.171654	0.585827	1.80	-0.23391	0.082835	0.541418	4.00	-0.05667	-0.05555	0.472224
0.33	-0.2088	0.179074	0.589537	1.85	-0.22703	0.076743	0.538371	4.05	-0.0546	-0.05693	0.471535
0.34	-0.2198	0.186014	0.593007	1.90	-0.22032	0.070865	0.535432	4.10	-0.05258	-0.05827	0.470865
0.35	-0.2303	0.192497	0.596248	1.95	-0.21378	0.065195	0.532598	4.15	-0.05061	-0.05957	0.470214

a/R_w	M_1	M_2	M_3	a/R_w	M_1	M_2	M_3	a/R_w	M_1	M_2	M_3
4.20	-0.0487	-0.060835	0.469582	6.60	0.00778	-0.09456	0.452721	9.00	0.031133	-0.10554	0.447228
4.25	-0.0468	-0.062063	0.468968	6.65	0.008478	-0.09492	0.452539	9.05	0.031461	-0.10568	0.447161
4.30	-0.045	-0.063256	0.468372	6.70	0.009164	-0.09528	0.452361	9.10	0.031784	-0.10581	0.447097
4.35	-0.0432	-0.064416	0.467792	6.75	0.009838	-0.09563	0.452187	9.15	0.032102	-0.10593	0.447033
4.40	-0.0414	-0.065543	0.467228	6.80	0.010501	-0.09597	0.452017	9.20	0.032416	-0.10606	0.446971
4.45	-0.0397	-0.066639	0.46668	6.85	0.011152	-0.0963	0.45185	9.25	0.032726	-0.10618	0.44691
4.50	-0.038	-0.067705	0.466148	6.90	0.011791	-0.09662	0.451688	9.30	0.033032	-0.1063	0.44685
4.55	-0.0364	-0.068741	0.46563	6.95	0.01242	-0.09694	0.451529	9.35	0.033333	-0.10642	0.446792
4.60	-0.0348	-0.069749	0.465125	7.00	0.013038	-0.09725	0.451373	9.40	0.03363	-0.10653	0.446734
4.65	-0.0333	-0.07073	0.464635	7.05	0.013646	-0.09756	0.451221	9.45	0.033924	-0.10664	0.446678
4.70	-0.0317	-0.071684	0.464158	7.10	0.014243	-0.09786	0.451072	9.50	0.034213	-0.10675	0.446623
4.75	-0.0303	-0.072613	0.463694	7.15	0.014831	-0.09815	0.450926	9.55	0.034499	-0.10686	0.446568
4.80	-0.0288	-0.073517	0.463242	7.20	0.015408	-0.09843	0.450784	9.60	0.03478	-0.10697	0.446515
4.85	-0.0274	-0.074397	0.462802	7.25	0.015976	-0.09871	0.450644	9.65	0.035058	-0.10707	0.446463
4.90	-0.026	-0.075253	0.462373	7.30	0.016535	-0.09898	0.450508	9.70	0.035332	-0.10718	0.446412
4.95	-0.0246	-0.076088	0.461956	7.35	0.017085	-0.09925	0.450374	9.75	0.035603	-0.10728	0.446362
5.00	-0.0233	-0.0769	0.46155	7.40	0.017625	-0.09951	0.450243	9.80	0.03587	-0.10737	0.446313
5.05	-0.022	-0.077692	0.461154	7.45	0.018157	-0.09977	0.450115	9.85	0.036134	-0.10747	0.446265
5.10	-0.0207	-0.078463	0.460769	7.50	0.01868	-0.10002	0.44999	9.90	0.036394	-0.10756	0.446218
5.15	-0.0194	-0.079214	0.460393	7.55	0.019195	-0.10026	0.449868	9.95	0.036651	-0.10766	0.446172
5.20	-0.0182	-0.079946	0.460027	7.60	0.019701	-0.1005	0.449748	10	0.036904	-0.10775	0.446126
5.25	-0.017	-0.080659	0.45967	7.65	0.0202	-0.10074	0.44963	11	0.041354	-0.10923	0.445385
5.30	-0.0158	-0.081355	0.459323	7.70	0.02069	-0.10097	0.449515	12	0.044851	-0.11022	0.444888
5.35	-0.0147	-0.082033	0.458984	7.75	0.021173	-0.1012	0.449402	13	0.047643	-0.11088	0.44456
5.40	-0.0136	-0.082694	0.458653	7.80	0.021648	-0.10142	0.449292	14	0.049905	-0.1113	0.444351
5.45	-0.0125	-0.083338	0.458331	7.85	0.022116	-0.10163	0.449184	15	0.051759	-0.11154	0.444228
5.50	-0.0114	-0.083967	0.458017	7.90	0.022577	-0.10184	0.449079	16	0.053295	-0.11167	0.444166
5.55	-0.0103	-0.08458	0.45771	7.95	0.02303	-0.10205	0.448975	17	0.054579	-0.1117	0.444149
5.60	-0.0093	-0.085178	0.457411	8.00	0.023476	-0.10225	0.448874	18	0.055661	-0.11167	0.444165
5.65	-0.0083	-0.085761	0.457119	8.05	0.023916	-0.10245	0.448774	19	0.056581	-0.11159	0.444206
5.70	-0.0073	-0.086331	0.456835	8.10	0.024349	-0.10265	0.448677	20	0.057366	-0.11147	0.444264
5.75	-0.0063	-0.086886	0.456557	8.15	0.024775	-0.10284	0.448582	25	0.05996	-0.11063	0.444687
5.80	-0.0053	-0.087428	0.456286	8.20	0.025195	-0.10302	0.448488	30	0.061304	-0.10967	0.445167
5.85	-0.0044	-0.087957	0.456021	8.25	0.025609	-0.10321	0.448397	35	0.062048	-0.10876	0.44562
5.90	-0.0035	-0.088474	0.455763	8.30	0.026016	-0.10339	0.448307	40	0.062474	-0.10795	0.446027
5.95	-0.0026	-0.088978	0.455511	8.35	0.026418	-0.10356	0.44822	45	0.06272	-0.10723	0.446387
6.00	-0.0017	-0.08947	0.455265	8.40	0.026813	-0.10373	0.448134	50	0.062857	-0.10659	0.446705
6.05	-0.0008	-0.089951	0.455025	8.45	0.027202	-0.1039	0.448049	55	0.062928	-0.10603	0.446987
6.10	5.2E-05	-0.09042	0.45479	8.50	0.027586	-0.10407	0.447967	60	0.062956	-0.10553	0.447237
6.15	0.00089	-0.090879	0.454561	8.55	0.027965	-0.10423	0.447886	65	0.062956	-0.10508	0.447461
6.20	0.00171	-0.091327	0.454337	8.60	0.028337	-0.10439	0.447807	70	0.062938	-0.10468	0.447662
6.25	0.00252	-0.091764	0.454118	8.65	0.028705	-0.10454	0.447729	75	0.062908	-0.10431	0.447844
6.30	0.00331	-0.092192	0.453904	8.70	0.029067	-0.10469	0.447653	80	0.062871	-0.10398	0.448008
6.35	0.00409	-0.092609	0.453695	8.75	0.029423	-0.10484	0.447579	85	0.062829	-0.10368	0.448159
6.40	0.00486	-0.093017	0.453491	8.80	0.029775	-0.10499	0.447506	90	0.062784	-0.10341	0.448296
6.45	0.00561	-0.093416	0.453292	8.85	0.030122	-0.10513	0.447434	95	0.062737	-0.10316	0.448422
6.50	0.00634	-0.093806	0.453097	8.90	0.030464	-0.10527	0.447364	100	0.062689	-0.10292	0.448539
6.55	0.00707	-0.094186	0.452907	8.95	0.030801	-0.10541	0.447295				